



# Mathematical Modelling and Numerical Simulation with Applications

ISSN Online : 2791-8564

Year : 2023

Volume : 3

Issue : 4



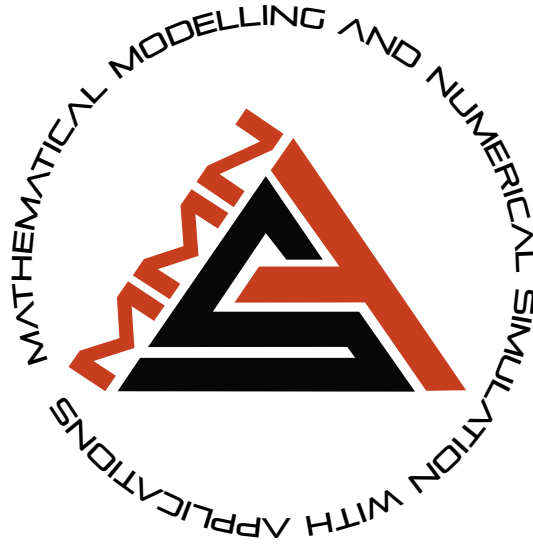
<https://dergipark.org.tr/en/pub/mmnsa>

Editor-in-Chief  
Mehmet Yavuz, PhD

M  
M  
N  
S  
A

VOLUME: 3 ISSUE: 4  
ISSN ONLINE: 2791-8564

December 2023  
<https://dergipark.org.tr/en/pub/mmnsa>



# MATHEMATICAL MODELLING AND NUMERICAL SIMULATION WITH APPLICATIONS

---

## Editor-in-Chief and Publisher

---

Mehmet Yavuz  
Department of Mathematics and Computer Sciences,  
Faculty of Science, Necmettin Erbakan University,  
Meram Yeniyol, 42090 Meram, Konya / TÜRKİYE  
mehmetyavuz@erbakan.edu.tr

---

## Associate Editors (In Alphabetical Order)

---

- **Abdeljawad, Thabet** - Prince Sultan University, Saudi Arabia
- **Agarwal, Praveen** - Anand International College of Engineering, India
- **Baleanu, Dumitru** - Cankaya University, Türkiye; Institute of Space Sciences, Bucharest, Romania
- **Hammouch, Zakia** - ENS Moulay Ismail University Morocco
- **Hristov, Jordan** - University of Chemical Technology and Metallurgy, Bulgaria
- **Karaca, Yeliz** - University of Massachusetts Chan Medical School, USA
- **Özdemir, Necati** - Balıkesir University, Türkiye
- **Pinto, Carla M.A.** - ISEP, Portugal
- **Sarris, Ioannis E.** - University of West Attica, Greece
- **Sene, Ndolane** - Cheikh Anta Diop University, Senegal
- **Stamova, Ivanka** - University of Texas at San Antonio, USA
- **Torres, Delfim F. M.** - University of Aveiro, Portugal
- **Townley, Stuart** - University of Exeter, United Kingdom

---

## Editorial Board Members (In Alphabetical Order)

---

- **Aguilar, José Francisco Gómez** - National Center for Technological Research and Development, Mexico
- **Ahmad, Hijaz** - International Telematic University, Uninettuno, Italy
- **Arqub, Omar Abu** - Al-Balqa Applied University, Jordan
- **Asjad, Muhammad Imran** - University of Management and Technology, Pakistan
- **Atangana, Abdon** - Faculty of Natural and Agricultural, Sciences, University of the Free State, South Africa
- **Başkonuş, Hacı Mehmet** - Harran University, Türkiye
- **Biswas, Md. Haider Ali** - Khulna University, Bangladesh
- **Bonyah, Ebenezer** - Akenten Appiah Menka University, Department of Mathematics Education, Ghana
- **Bulai, Iulia Martina** - University of Basilicata, Italy
- **Cabada, Alberto** - University of Santiago de Compostela, Spain
- **Dassios, Ioannis** - University College Dublin, Ireland
- **Eskandari, Zohreh** - Department of Mathematics, Faculty of Science, Fasa University, Fasa, Iran
- **Flaut, Cristina** - Ovidius University of Constanta, Romania
- **González, Francisco Martínez** - Universidad Politécnica de Cartagena, Spain
- **Gürbüz, Burcu** - Johannes Gutenberg-University Mainz, Institute of Mathematics, Germany
- **Jafari, Hossein** - University of Mazandaran, Iran; University of South Africa, UNISA003, South Africa
- **Jajarmi, Amin** - University of Bojnord, Iran
- **Kaabar, Mohammed K.A.** - Washington State University, USA
- **Kumar, Devendra** - University of Rajasthan, India

- **Kumar, Sunil** - National Institute of Technology, India
- **Lupulescu, Vasile** - Constantin Brâncuși University of Târgu-Jiu, Romania
- **Merdan, Hüseyin** - TOBB University of Economy and Technology, Department of Mathematics, Türkiye
- **Mohammed S. Abdo** - Hodeidah University, Al-Hodeidah, Department of Mathematics, Yemen
- **Muñoz-Pacheco, Jesus Manuel** - Faculty of Electronics Sciences at the Autonomous University of Puebla (BUAP), Mexico
- **Noeiaghdam, Samad** - Irkutsk National Research Technical University, Russian Federation
- **Owolabi, Kolade** - Federal University of Technology, Nigeria
- **Otero-Espinar, Maria Victoria** - University of Santiago de Compostela, Spain
- **Panigoro, Hasan S.** - Universitas Negeri Gorontalo, Indonesia
- **Povstenko, Yuriy** - Jan Dlugosz University in Czestochowa, Poland
- **Qureshi, Sania** - Mehran University of Engineering and Technology, Pakistan
- **Sabatier, Jocelyn** - Bordeaux University, France
- **Safaei, Mohammad Reza** - Florida International University, USA
- **Salahshour, Soheil** - Bahçeşehir University, Türkiye
- **Sarı, Murat** - Yıldız Technical University, Türkiye
- **Singh, Jagdev** - JECRC University, India
- **Valdés, Juan Eduardo Nápoles** - Universidad Nacional del Nordeste, Argentina
- **Veerasha, Pundikala** - Christ University, India
- **Weber, Gerhard-Wilhelm** - Poznan University of Technology, Poland
- **Xu, Changjin** - Guizhou University of Finance and Economics, China
- **Yang, Xiao-Jun** - China University of Mining and Technology, China
- **Yuan, Sanling** - University of Shanghai for Science and Technology, China

---

## Scientific Managing Editor

---

Fırat Evirgen  
Balıkesir University, Balıkesir / TÜRKİYE  
fevirgen@balikesir.edu.tr

---

## Technical Editor

---

Kerim Sarıgöl  
Gazi University, Ankara / TÜRKİYE  
kerimsarigul@gazi.edu.tr

---

## English Editors (In Alphabetical Order)

---

- **Abdulkadir Ünal** - School of Foreign Languages, Foreign Languages, Alanya Alaaddin Keykubat University, Antalya Türkiye.
  - **Ahmet Sınak** - Necmettin Erbakan University, Department of Mathematics and Computer Sciences, Konya, Türkiye.
  - **Faruk Türk** - Karamanoğlu Mehmetbey University, School of Foreign Languages, Karaman, Türkiye.
- 

## Editorial Secretariat

---

Fatma Özlem Coşar  
Department of Mathematics and Computer Sciences,  
Faculty of Science, Necmettin Erbakan University,  
Meram Yenyol, 42090 Meram, Konya / TÜRKİYE

Müzeyyen Akman  
Department of Mathematics and Computer Sciences,  
Faculty of Science, Necmettin Erbakan University,  
Meram Yenyol, 42090 Meram, Konya / TÜRKİYE

---

# Contents

## *Research Articles*

- 1 An enhanced SUPG-stabilized finite element formulation for simulating natural phenomena governed by coupled system of reaction-convection-diffusion equations  
*Süleyman Cengizci* 297-317
- 2 Optimal control of diabetes model with the impact of endocrine-disrupting chemical: an emerging increased diabetes risk factor  
*P. Logaprakash, C. Monica* 318-334
- 3 Examination of Sturm-Liouville problem with proportional derivative in control theory  
*Bahar Acay Öztürk* 335-350
- 4 Genocchi collocation method for accurate solution of nonlinear fractional differential equations with error analysis  
*Mohamed El-Gamel, Nesreen Mohamed, Waleed Adel* 351-375
- 5 The role of calcium dynamics with amyloid beta on neuron-astrocyte coupling  
*Hemlata Jethanandani, Brajesh Kumar Jha, Manisha Ubale* 376-390



RESEARCH PAPER

# An enhanced SUPG-stabilized finite element formulation for simulating natural phenomena governed by coupled system of reaction-convection-diffusion equations

Süleyman Cengizci  <sup>1,2,\*</sup>, ‡

<sup>1</sup>Computer Programming, Antalya Bilim University, Antalya 07190, Türkiye, <sup>2</sup>Department of Business Administration, Antalya Bilim University, Antalya 07190, Türkiye

\*Corresponding Author

‡suleyman.cengizci@antalya.edu.tr (Süleyman Cengizci)

## Abstract

Many phenomena arising in nature, science, and industry can be modeled by a coupled system of reaction-convection-diffusion (RCD) equations. Unfortunately, obtaining analytical solutions to RCD systems is typically not possible and, therefore, usually requires the use of numerical methods. On the other hand, since solutions to RCD-type equations can exhibit rapid changes and may have boundary/inner layers, classical computational tools yield approximations polluted with physically meaningless oscillations when convection dominates the transport process. Towards that end, in order to eliminate such numerical instabilities without sacrificing accuracy, this work employs a stabilized finite element formulation, the so-called streamline-upwind/Petrov–Galerkin (SUPG) method. The SUPG-stabilized formulation is then also supplemented with the  $YZ\beta$  shock-capturing mechanism to achieve higher-quality approximations around sharp gradients. A comprehensive set of numerical test experiments, including cross-diffusion systems, the Schnakenberg reaction model, and mussel-algae interactions, is considered to reveal the robustness of the proposed formulation, which we call the SUPG- $YZ\beta$  formulation. Comparisons with reported studies reveal that the proposed formulation performs quite well without introducing excessive numerical dissipation.

**Keywords:** Reaction-convection-diffusion; finite elements; stabilization; shock-capturing; SUPG- $YZ\beta$  formulation

**AMS 2020 Classification:** 35G61; 65M60; 76M10

## 1 Introduction

Reaction-convection-diffusion (RCD) equations are used to model a wide range of natural phenomena in addition to many industrial and engineering applications. Some of these applications

include financial engineering (e.g., Black–Scholes and Heston option pricing models), chemistry (e.g., chemically reactive transport phenomena), semiconductor theory (e.g., drift-diffusion equations), fluid dynamics (e.g., Burgers'-type and Navier–Stokes equations), heat transfer (e.g., natural heat convection phenomena), and mathematical physics and astrophysics (e.g., Fokker–Planck-type equations). The coupled systems consisting of RCD-type equations are also essential for modeling many phenomena that involve interactions between more than one species and frequently arise in biological and chemical sciences, such as tumor growth models, chemotaxis processes, bacteria pattern formation, predator-prey dynamics, etc. We refer the interested reader to the extensive work of Painter [1] and Bellomo et al. [2] for chemotaxis and cross-diffusion models and their applications in biology, physiology and pathology, ecology, and even in the social sciences (e.g., crime hotspot models). The review papers [3] and [4] can also be referred to for more on pattern formation phenomena arising in plasma physics and the influence of temperature on such systems, respectively.

Analytical solutions to RCD-type systems are generally impossible to obtain since they are typically of a nonlinear nature and/or defined on sophisticated domains. Therefore, numerical approximations to the solutions of such systems are searched for. Unfortunately, despite the availability of several classical and mature numerical methods with solid theoretical foundations and sharp error estimates, such as the finite difference method (FDM), finite volume method (FVM), and finite element method (FEM), these methods are insufficient to provide accurate approximations to the solutions of RCD-type equations and coupled systems composed of such equations in convection dominance, leading to spurious oscillations. In order to overcome such numerical instability issues, the above-mentioned classical methods have been enhanced with several techniques over the years. The following paragraph presents a very concise overview of reported studies dedicated to solving coupled systems of RCD-type equations numerically. For a more comprehensive overview, the material in these references can also be referred to.

The authors of [5] investigated the effect of advection on coupled systems of reaction-diffusion (RD) equations, more specifically, the Schnackenberg and glycolysis reaction kinetics models having toroidal velocity fields, by employing the classical finite element method. Sarra considered unsteady RCD-type partial differential equations (PDEs) by employing a local radial basis function (RBF) method in [6]. The author particularly focused on chemotaxis models and Turing systems defined on complex-shaped domains. In [7], the authors proposed positivity-preserving nonstandard finite difference schemes for cross-diffusion models arising in biosciences, including malignant invasion, convective predator-prey pursuit and evasion model, and reaction-diffusion-chemotaxis model. Yücel et al. [8] studied optimal control problems governed by a system of convection-dominated RCD-type PDEs by employing a discontinuous GFEM (dGFEM) formulation. They used a symmetric interior penalty Galerkin (SIPG) discretization for the diffusion term and an upwinding discretization for the convection term, along with an adaptive mesh refinement algorithm. The author of [9] used a meshless finite difference method equipped with B-splines for solving time-dependent RD- and RCD-type coupled systems, including tumor invasion models and cross-diffusion problems. Wang et al. [10] studied the dynamics and pattern formation of a coupled time-dependent RCD system defined on a one-dimensional (1D) domain for modeling the interaction of mussels and algae. Most recently, two-dimensional (2D) elliptic-type singularly perturbed weakly-coupled systems of RCD equations, in which the diffusion and convection terms are controlled by two different parameters, were studied by Clavero et al. [11]. They proposed a first-order uniformly convergent finite difference scheme defined on layer-adapted Bakhvalov–Shishkin meshes. One can also refer to [12–14] and references therein for several applications of scalar and coupled RCD-type PDEs arising in chemical processes. Finally, in the context of

fractional differential equations, the studies [15–17] and the material therein can be referred to.

In the finite element framework, among the others, one of the most established, robust, and popular stabilized methods is the streamline-upwind/Petrov–Galerkin (SUPG) formulation. The method was first introduced for advection-diffusion equations and incompressible flow simulations by Hughes and Brooks [18, 19]. Following that, the compressible-flow SUPG method was introduced by Tezduyar and Hughes [20–22] in the context of conservation variables. The compressible-flow SUPG method introduced in 1982 is today denoted by “(SUPG)<sub>82</sub>.” The (SUPG)<sub>82</sub> formulation, in its initial form, was used without making use of any discontinuity-capturing (also commonly referred to as shock-capturing) mechanism. The test simulations demonstrated that regions with steep gradients require extra treatment. Then, the (SUPG)<sub>82</sub> formulation was subsequently reformulated in terms of the entropy variables and equipped with a shock-capturing mechanism in [23], and more satisfactory results were obtained. In [24], the (SUPG)<sub>82</sub> formulation was supplemented with a shock-capturing operator quite similar to the one introduced in [23] by Hughes et al., and the added term included a shock-capturing parameter, which is today called “ $\delta_{91}$ .” The set of stabilization parameters, which is almost universally denoted by “ $\tau$ ,” used with the (SUPG)<sub>82</sub> formulation introduced in [20–22] are called “ $\tau_{82}$ ” today. The SUPG-stabilized formulation for the reaction-advection-diffusion equation introduced in [25] included a shock-capturing term and a stabilization parameter that took into account the interaction between the shock-capturing and SUPG stabilization terms. Thus, the effect of the shock-capturing mechanism does not increase that of the SUPG stabilization when the advection and shock directions coincide. In [24], the definition of stabilization parameter  $\tau_{82}$  was slightly modified by Le Beau et al. On the other hand, although the definition of (SUPG)<sub>82</sub> parameters underwent some minor modifications in subsequent years, they were still used with the same shock-capturing parameter,  $\delta_{91}$ , until 2004. Eventually, in 2004, several new ways of determining the stabilization and shock-capturing parameters in the (SUPG)<sub>82</sub> framework were introduced in [26, 27] by Tezduyar. These new stabilization parameters are today referred to as “ $\tau_{04}$ .” As to the shock-capturing parameters, the new strategies introduced can be divided into two categories: the discontinuity-capturing directional dissipation (DCDD) [26, 28, 29] and the residual-based  $YZ\beta$  shock-capturing [26, 27]. Throughout this paper, we restrict our attention to the  $YZ\beta$  mechanism. Some of the reasons for adopting it include that it is easier to calculate the  $YZ\beta$  shock-capturing parameter than  $\delta_{91}$ , the parameter  $\beta$  offers options for mild and sharp shocks, and as it was also reported in [30–32], the  $YZ\beta$  parameter yields more accurate results than  $\delta_{91}$ . One can find various applications of the SUPG- $YZ\beta$  combination, including arterial drug delivery, shallow-water equations, chemically reactive models, and natural convection heat transfer, in [12, 33–37]. For other stabilized formulation and shock-capturing mechanisms, we refer the interested reader to [38–40] and the material in these studies. Besides that, in [41–43], the interested reader can find various applications of Petrov–Galerkin-like methods.

In this paper, we deal with stabilized finite element computations of coupled systems of RCD-type equations. In doing this, we first consider the test problems as they were reported in the literature in order to make comparisons. Following that, whenever possible, each problem is considered for convection dominance, i.e., for much more computationally challenging cases, for which the classical methods fail to yield oscillation-free approximations and/or are insufficient to capture steep gradients. Thus, new challenging benchmark problems are introduced to the literature. The main computational method we use is the SUPG finite element formulation. We also augment the SUPG-stabilized formulation with the  $YZ\beta$  shock-capturing technique. To the author’s best knowledge, this is the first report employing the SUPG- $YZ\beta$  combination for handling such kinds of problems. The semi-discrete formulations are discretized in time with the backward Euler

scheme. Then, nonlinear equation systems arising from the space-time-discretized formulations are solved with the Newton–Raphson (N–R) algorithm, and the resulting linear systems are handled with a direct method, i.e., the lower-upper (LU) factorization technique.

The rest of the manuscript is organized as follows. In [Section 2](#), a system of coupled 2D RCD-type PDEs is introduced as a model problem, and a semi-discrete GFEM formulation is described. In [Section 3](#), a SUPG-stabilized finite element formulation combined with  $YZ\beta$  shock-capturing is introduced for the model problem. [Section 4](#) first focuses on further computational details, such as the temporal discretization of the semi-discrete formulation, the quadrature degree associated with the numerical integration, and the computing environment FEniCS, in which the solvers are developed and computations are carried out. Later on in this section, four main numerical experiments with various scenarios are presented. Finally, in [Section 5](#), some concluding remarks are made, along with a brief discussion on possible extensions of this current work.

## 2 Model problem and classical GFEM formulation

Let us consider the following coupled system of time-dependent RCD equations:

$$\frac{\partial \mathbf{u}}{\partial t} + \mathbf{a} \cdot \nabla \mathbf{u} - \nabla \cdot (\mathbf{D} \nabla \mathbf{u}) - \mathbf{f}(\mathbf{u}) = \mathbf{s}, \quad (1)$$

where the vector of unknowns,  $\mathbf{u}$ , is defined by  $\mathbf{u} = [u_1, u_2]^T$ ,  $\mathbf{a} = [a_1, a_2]$  is the velocity field associated with advection, and  $\mathbf{D}$  represents the diffusivity matrix, which is given as:

$$\mathbf{D} = \begin{bmatrix} \epsilon_1 & 0 \\ 0 & \epsilon_2 \end{bmatrix}. \quad (2)$$

Here, the diffusion parameters  $\epsilon_1$  and  $\epsilon_2$  are non-negative and typically small. The vector  $\mathbf{f}$  represents the reaction term, which is typically of nonlinear nature, and  $\mathbf{s}$  is the source vector. For the moment, the system is assumed to be equipped with an appropriate set of initial and boundary conditions.

By multiplying both sides of system (1) by a test vector  $\mathbf{w} \in \mathcal{V}_{\mathbf{u}} \subset \mathcal{H}_0^1$ , the classical GFEM formulation can be obtained as follows:

$$\begin{cases} \text{find } \mathbf{u} \in \mathcal{S}_{\mathbf{u}} \text{ such that } \forall \mathbf{w} \in \mathcal{V}_{\mathbf{u}} : \\ \int_{\Omega} \mathbf{w} \cdot \left( \frac{\partial \mathbf{u}}{\partial t} + \mathbf{a} \cdot \nabla \mathbf{u} - \nabla \cdot (\mathbf{D} \nabla \mathbf{u}) - \mathbf{f}(\mathbf{u}) - \mathbf{s} \right) d\Omega = 0, \end{cases} \quad (3)$$

where  $\mathbf{u} \in \mathcal{S}_{\mathbf{u}} \subset \mathcal{H}_g^1$  is the solution vector, and the spaces  $\mathcal{S}_{\mathbf{u}}$  and  $\mathcal{V}_{\mathbf{u}}$  are the trial and test function spaces, respectively. The Sobolev spaces  $\mathcal{H}_0^1$  and  $\mathcal{H}_g^1$  are defined as follows:

$$\mathcal{H}_0^1 = \left\{ \Phi : \Phi \in [\mathcal{H}^1(\Omega)]^2 \text{ and } \Phi|_{\partial\Omega} = \mathbf{0} \right\}, \quad (4)$$

$$\mathcal{H}_g^1 = \left\{ \Phi : \Phi \in [\mathcal{H}^1(\Omega)]^2 \text{ and } \Phi|_{\partial\Omega} = \mathbf{g} \right\}, \quad (5)$$

where

$$\mathcal{H}^1 = \left\{ \Phi : \|\Phi\|_{L_{\Omega}^2} + \|\nabla \Phi\|_{L_{\Omega}^2} < \infty \right\}. \quad (6)$$

The vector  $\mathbf{g} = [g_1, g_2]$  denotes the vector of prescribed Dirichlet-type boundary conditions. Here, the space  $L^2_\Omega = L^2(\Omega)$  is the space of square-integrable functions defined on  $\Omega$ , and is equipped with the standard  $L^2$ -norm:

$$\|\Phi\|_{L^2_\Omega} = \sqrt{\int_\Omega \Phi^2 dx}. \quad (7)$$

Employing integration-by-parts, the variational formulation given by Eq. (3) can be recast as follows:

$$\left\{ \begin{array}{l} \text{find } \mathbf{u} \in \mathcal{S}_u \text{ such that } \forall \mathbf{w} \in \mathcal{V}_u : \\ \int_\Omega \mathbf{w} \cdot \left( \frac{\partial \mathbf{u}}{\partial t} + \mathbf{a} \cdot \nabla \mathbf{u} - \mathbf{s} \right) d\Omega + \int_\Omega (\nabla \mathbf{w} : (\mathbf{D}\nabla \mathbf{u})) d\Omega \\ - \int_\Omega \mathbf{w} \cdot \mathbf{f}(\mathbf{u}) d\Omega - \int_{\Gamma_N} \mathbf{w} \cdot \mathbf{h} d\Gamma = 0, \end{array} \right. \quad (8)$$

where  $\mathbf{h} = \mathbf{D}\nabla \mathbf{u} \cdot \mathbf{n}$  is the Neumann-type boundary data,  $\mathbf{n}$  is outward-oriented unit normal vector, and  $\Gamma$  denotes the boundary of the computational domain  $\Omega$ , i.e.,  $\Gamma = \partial\Omega$ . Note that  $\Gamma = \Gamma_N \cup \Gamma_D$  and  $\Gamma_N \cap \Gamma_D = \emptyset$ , where the subscripts “N” and “D” indicate that whether the boundary is subject to Neumann- or Dirichlet-type boundary conditions.

If the computational domain  $\Omega$  is divided into finite number of elements  $\Omega^e$ ,  $e = 1, 2, \dots, n_{el}$ , where  $n_{el}$  denotes the number of these elements, then the GFEM formulation associated with system (1) reads:

$$\left\{ \begin{array}{l} \text{find } \mathbf{u}^h \in \mathcal{S}_u^h \text{ such that } \forall \mathbf{w}^h \in \mathcal{V}_u^h : \\ \int_\Omega \mathbf{w}^h \cdot \left( \frac{\partial \mathbf{u}^h}{\partial t} + \mathbf{a} \cdot \nabla \mathbf{u}^h - \mathbf{s} \right) d\Omega + \int_\Omega (\nabla \mathbf{w}^h : (\mathbf{D}\nabla \mathbf{u}^h)) d\Omega \\ - \int_\Omega \mathbf{w}^h \cdot \mathbf{f}(\mathbf{u}^h) d\Omega - \int_{\Gamma_N} \mathbf{w}^h \cdot \mathbf{h}^h d\Gamma = 0, \end{array} \right. \quad (9)$$

where the superscript “h” indicates that the functions that are the components of the associated vectors/matrices come from a finite-dimensional space. The finite-dimensional function spaces are defined as follows:

$$\mathcal{S}_u^h = \mathcal{V}_u^h = \left\{ \Phi^h \in [\mathcal{C}(\overline{\Omega})]^2 : \Phi^h|_{\partial\Omega} = \mathbf{0}, \Phi^h|_{\Omega^e} \in [\mathcal{P}_1(\Omega^e)]^2, \forall \Omega^e \in \mathcal{T}^h \right\}, \quad (10)$$

where  $\mathcal{P}_1(\Omega^e)$  is the space of linear polynomials over the triangular element  $\Omega^e \in \mathcal{T}^h$ ,  $\mathcal{C}(\overline{\Omega})$  is the space of continuous functions defined on the closure of the computational domain, and  $\mathcal{T}^h$  is the triangulation of the domain  $\Omega$  into triangular elements.

### 3 Stabilized finite element formulations

This section describes the SUPG and SUPG-YZ $\beta$  formulations of the model problem given by Eq. (1), respectively.

The SUPG formulation associated with system (1) can be given as follows:

$$\left\{ \begin{array}{l} \text{find } \mathbf{u}^h \in \mathcal{S}_u \text{ such that } \forall \mathbf{w}^h \in \mathcal{V}_u^h : \\ \int_{\Omega} \mathbf{w}^h \cdot \left( \frac{\partial \mathbf{u}^h}{\partial t} + \mathbf{a} \cdot \nabla \mathbf{u}^h - \mathbf{s} \right) d\Omega + \int_{\Omega} \left( \nabla \mathbf{w}^h : \left( \mathbf{D} \nabla \mathbf{u}^h \right) \right) d\Omega \\ - \int_{\Omega} \mathbf{w}^h \cdot \mathbf{f} \left( \mathbf{u}^h \right) d\Omega - \int_{\Gamma_N} \mathbf{w}^h \cdot \mathbf{h}^h d\Gamma \\ + \sum_{e=1}^{n_{el}} \int_{\Omega^e} \boldsymbol{\tau}_{\text{SUPG}} \left( \frac{\partial \mathbf{w}^h}{\partial x_k} \right) \mathbf{a}^T \cdot \left( \frac{\partial \mathbf{u}^h}{\partial t} + \mathbf{a} \cdot \nabla \mathbf{u}^h - \nabla \cdot \left( \mathbf{D} \nabla \mathbf{u}^h \right) - \mathbf{f} \left( \mathbf{u}^h \right) - \mathbf{s} \right) d\Omega = 0, \end{array} \right. \quad (11)$$

where the finite-dimensional space  $\mathcal{V}_u^h$  is defined by Eq. (10). In this formulation,  $e$  is the element counter and  $\boldsymbol{\tau}_{\text{SUPG}}$  is the diagonal SUPG stabilization matrix. How these stabilization parameters are determined directly affects the accuracy and quality of the numerical approximations.

**Remark 1** In the last line of Eq. (11), by the term  $\left( \frac{\partial \mathbf{w}^h}{\partial x_k} \right)$ , we refer to Einstein summation convention; i.e.,

$$\left( \frac{\partial \mathbf{w}^h}{\partial x_k} \right) = \sum_{k=1}^{n_{sd}} \frac{\partial w_k^h}{\partial x_k}, \quad (12)$$

where  $w_k^h$  is the  $k$ -th component of the test vector  $\mathbf{w}^h$ .

For solving stationary problems, the stabilization matrix,  $\boldsymbol{\tau}_{\text{SUPG}}$ , is composed of stabilization parameters,  $\tau_{\text{SUPG}}^i$ 's, which are defined as follows [44]:

$$\tau_{\text{SUPG}}^i = \left[ \left( \frac{2\|\mathbf{a}\|}{h^e} \right)^2 + \left( \frac{4\epsilon_i}{(h^e)^2} \right)^2 \right]^{-\frac{1}{2}}, \quad (13)$$

where  $i = 1, 2$ , the norm  $\|\cdot\|$  represents the standard Euclidean norm, and  $h^e$  is the cell diameter associated with element  $\Omega^e$ . For unsteady problems, these parameters can be defined as

$$\tau_{\text{SUPG}}^i = \left[ \left( \frac{2}{\Delta t} \right)^2 + \left( \frac{2\|\mathbf{a}\|}{h^e} \right)^2 + \left( \frac{4\epsilon_i}{(h^e)^2} \right)^2 \right]^{-\frac{1}{2}}. \quad (14)$$

For systems involving different convection vectors, e.g.,  $\mathbf{a}_i$ 's, these parameters can be defined in the following fashion:

$$\tau_{\text{SUPG}}^i = \left[ \left( \frac{2}{\Delta t} \right)^2 + \left( \frac{2\|\mathbf{a}_i\|}{h^e} \right)^2 + \left( \frac{4\epsilon_i}{(h^e)^2} \right)^2 \right]^{-\frac{1}{2}}. \quad (15)$$

In these definitions given by Eqs. (13)–(14), the superscript “ $i$ ” in  $\tau_{\text{SUPG}}^i$  indicates that the parameter is associated with the  $i$ th equation in the system. Similarly, the subscripts in convection vectors (i.e.,  $\mathbf{a}_i$ 's) and diffusion parameters (i.e.,  $\epsilon_i$ 's) indicate that they belong to the  $i$ th equation. For further details and a review of various definitions of the stabilization parameters and element

length scales, we refer the interested reader to [38, 39, 45, 46] and references therein.

**Remark 2** One should note that, compared to the classical GFEM formulation given by Eq. (3), the SUPG formulation introduced by Eq. (11) involves additional element-based stabilization terms controlled by the stabilization parameters. By adding these terms, the original system gains artificial dissipation in the streamline direction.

**Remark 3** One can also find a variation in the definition of stabilization parameters given by Eqs. (13)–(14) based on the approach followed in [44, 47]:

$$\tau_{\text{SUPG}}^i = \left[ \left( \frac{2}{\Delta t} \right)^2 + \left( \frac{2\|\mathbf{a}_i\|}{h^e} \right)^2 + 9 \left( \frac{4\epsilon_i}{(h^e)^2} \right)^2 \right]^{-\frac{1}{2}}. \quad (16)$$

For stationary problems, the term associated with time is simply omitted, as done in Eq. (13).

We adopt the stabilization parameter described by Eq. (16), in our computations. Then, the stabilization matrix,  $\tau_{\text{SUPG}}$ , associated with the model problem described by Eq. (1) can be given as follows:

$$\tau_{\text{SUPG}} = \begin{bmatrix} \tau_{\text{SUPG}}^1 & 0 \\ 0 & \tau_{\text{SUPG}}^2 \end{bmatrix}. \quad (17)$$

Eventually, the SUPG- $\text{YZ}\beta$  formulation associated with system (1) can be described as follows:

$$\left\{ \begin{array}{l} \text{find } \mathbf{u}^h \in \mathcal{S}_{\mathbf{u}}^h \text{ such that } \forall \mathbf{w}^h \in \mathcal{V}_{\mathbf{u}}^h : \\ \int_{\Omega} \mathbf{w}^h \cdot \left( \frac{\partial \mathbf{u}^h}{\partial t} + \mathbf{a} \cdot \nabla \mathbf{u}^h - \mathbf{s} \right) d\Omega + \int_{\Omega} \left( \nabla \mathbf{w}^h : (\mathbf{D} \nabla \mathbf{u}^h) \right) d\Omega \\ - \int_{\Omega} \mathbf{w}^h \cdot \mathbf{f}(\mathbf{u}^h) d\Omega - \int_{\Gamma_N} \mathbf{w}^h \cdot \mathbf{h}^h d\Gamma \\ + \sum_{e=1}^{n_{\text{el}}} \int_{\Omega^e} \tau_{\text{SUPG}} \left( \frac{\partial \mathbf{w}^h}{\partial x_k} \right) \mathbf{a}^T \cdot \left( \frac{\partial \mathbf{u}^h}{\partial t} + \mathbf{a} \cdot \nabla \mathbf{u}^h - \nabla \cdot (\mathbf{D} \nabla \mathbf{u}^h) - \mathbf{f}(\mathbf{u}^h) - \mathbf{s} \right) d\Omega \\ + \sum_{e=1}^{n_{\text{el}}} \int_{\Omega^e} \nu_{\text{SHOC}} \left( \frac{\partial \mathbf{w}^h}{\partial x_k} \right) \cdot \left( \frac{\partial \mathbf{u}^h}{\partial x_k} \right) d\Omega = 0, \end{array} \right. \quad (18)$$

where the term  $\nu_{\text{SHOC}}$  is the stabilization parameter associated with the  $\text{YZ}\beta$  shock-capturing technology. The shock-capturing parameter is defined in light of studies by Tezduyar [30–32]. In this work, we slightly modify the original definition of the shock-capturing parameter to solve the model problem as follows [33]:

$$\nu_{\text{SHOC}}^i = |Y^{-1}Z_i| \left( \sum_{i=1}^{n_{\text{sd}}} \left| Y^{-1} \frac{\partial u_i^h}{\partial x_i} \right|^2 \right)^{\frac{\beta}{2}-1} \left( \frac{h_{\text{SHOC}}^i}{2} \right)^{\beta}, \quad (19)$$

where

$$Z_i = \frac{\partial u_i}{\partial t} - \nabla \cdot (\epsilon_i \nabla u_i^h) + \mathbf{a} \cdot \nabla u_i^h - f_i - s_i. \quad (20)$$

**Remark 4** Compared to the SUPG-based stabilized formulation given by Eq. (11), the SUPG-YZ $\beta$  formulation described by Eq. (18) involves additional element-based stabilization terms associated with the shock-capturing mechanism. These new terms introduce additional artificial diffusion in the direction of solution gradients, which helps to mitigate undershoots and overshoots around sharp layers.

**Remark 5** As also mentioned by Remark 1, by the terms  $\left(\frac{\partial \mathbf{w}^h}{\partial x_k}\right)$  and  $\left(\frac{\partial \mathbf{u}^h}{\partial x_k}\right)$  in Eq. (18), we refer to Einstein summation convention.

**Remark 6** By using Eq. (20) in computations, we adopt the residual form of  $Z_i$ , which is similar to that used by Bazilevs et al. in [33] as a variation of the advective form introduced in [26, 27]:

$$Z_i = \mathbf{a} \cdot \nabla u_i^h. \quad (21)$$

In addition to that used in [33], following this way, we also include the reaction and source terms in the definition of  $Z_i$ .

**Remark 7** The definition of quantity  $Z_i$  can be extended to handle the case of different advection vectors  $a_i$ 's in the same way followed for describing the SUPG stabilization parameter defined by Eq. (15).

In Eq. (19), the quantity  $Y$  can be determined as follows:

$$Y = \sqrt{u_{1,\text{ref}}^2 + u_{2,\text{ref}}^2}. \quad (22)$$

The reference values  $u_{i,\text{ref}}$ 's are typically determined according to the initial data given for time-dependent problems. For steady-state problems, they can also be determined as reference values or through numerical experiments. The local element length scales,  $h_{\text{SHOC}}^i$ 's, are defined as

$$h_{\text{SHOC}}^i = 2 \left( \sum_{a=1}^{n_{\text{en}}} |\mathbf{j}_i \cdot \nabla N_a| \right)^{-1}, \quad (23)$$

with the unit vector in the direction of the gradient of  $u_i^h$ :

$$\mathbf{j}_i = \frac{\nabla u_i^h}{\|\nabla u_i^h\|}. \quad (24)$$

Here, the term  $N_a$  represents the interpolating function associated with element node  $a$ . The indices  $n_{\text{sd}}$  and  $n_{\text{en}}$  stand for the number of space-dimensions and number of element nodes. The sharpness parameter  $\beta$  is typically set as  $\beta = 1$  for mild shocks and  $\beta = 2$  for sharper shocks [30–32]. Since the main focus of this study is problems highly dominated by convection, we set the parameter  $\beta$  as  $\beta = 2$  in our computations.

**Remark 8** The finite element formulations introduced in the previous lines for a two-species model given by Eq. (1) can be easily extended to models with more species and/or higher dimensions. Similarly, as discussed in the previous lines, these formulations can also be modified for handling systems of RCD-type equations with different convection fields instead of ones having the same convection vector .

## 4 Numerical experiments

After providing some computational details, such as the time-integration, absolute and relative error tolerances associated with linear and nonlinear solvers, and computing platform, as the first numerical experiment, we consider a cross-diffusion reaction-diffusion system with component-wise analytical solutions in order to validate our GFEM solvers. Then, again for verification purposes, we deal with a steady convection-dominated RCD system with component-wise exact solutions. Following that, we focus on coupled systems of time-dependent RCD equations.

### Further computational details

Throughout this work, for unsteady problems, the time discretization is performed with the backward Euler scheme, i.e., the semi-discrete (spatially discretized) formulations (see Eqs. (9), (11), and (18)) introduced in the previous sections are discretized such that as advancing from time-step  $n$  to  $n + 1$ :

$$\frac{\partial U^h}{\partial t} = \frac{U_{n+1}^h - U_n^h}{\Delta t} = \mathcal{J}_{n+1}^h, \quad (25)$$

where  $\mathcal{J}_{n+1}^h$  represents the rest of the terms in the variational formulations computed at time steps  $n + 1$ . The relative and absolute convergence criteria associated with the N–R algorithm are both set to  $1.0 \times 10^{-12}$ . All computations are carried out in serial in the FEniCS [48–50] scientific computing environment, which is particularly dedicated to the finite element solution of differential equations and allows the user high-level C++ and Python interfaces, on a computer equipped with Intel i7-12650H CPU and 40GB RAM running Ubuntu 20.04.5 LTS. For further details on the FEniCS Project, we refer the interested reader to the references provided above and the official webpage of the project: <https://fenicsproject.org/>. Since the test computations, apart from the first numerical experiment (*Application 1*), are of highly nonlinear nature, we set the quadrature degree associated with the numerical integration to eleven. Besides, all the finite element meshes are triangular and generated by using the built-in `mshr` component of FEniCS.

### Test computations

*Application 1 – Reaction-diffusion with cross-diffusion.* We take this test example, which was originally studied in [51], from [9], for comparison purposes. It is described as follows:

$$\begin{cases} \frac{\partial u}{\partial t} = D_{11} \Delta u + D_{12} \Delta v + D_{13} v, \\ \frac{\partial v}{\partial t} = D_{21} \Delta u + D_{22} \Delta v + D_{23} u, \end{cases} \quad (26)$$

where the spatial domain is defined by  $\Omega = (0, 2\pi)^2$ , and  $t > 0$ . The component-wise initial conditions are defined as

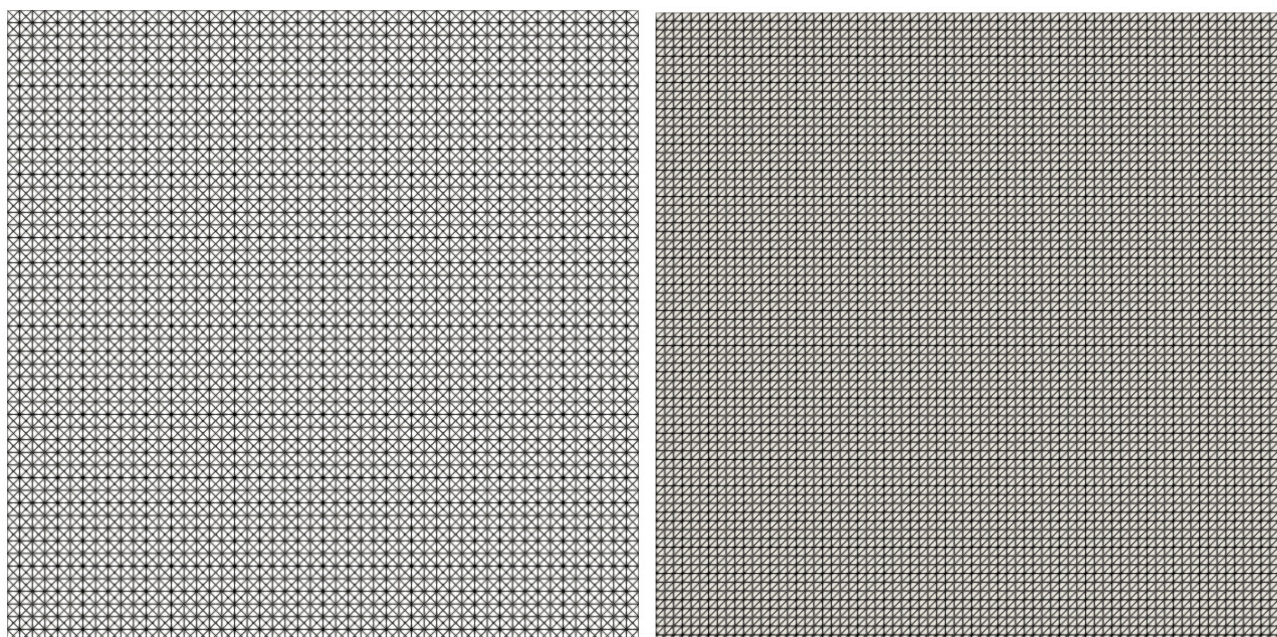
$$u(x_1, x_2, 0) = \cos(2x_1) + \cos(2x_2), \quad v(x_1, x_2, 0) = \cos(x_1) + \cos(x_2). \quad (27)$$

At walls, zero-flux, i.e., homogeneous Neumann-type boundary conditions apply. Then, the component-wise analytical solutions to the system described by Eq. (26) are given as

$$u(x_1, x_2, t) = \exp(-4t\beta) [\cos(2x_1) + \cos(2x_2)], \quad (28)$$

$$v(x_1, x_2, t) = \exp(-t\beta) [\cos(x_1) + \cos(x_2)], \quad (29)$$

where  $D_{11} = D_{22} = \beta = 0.01$ ,  $D_{12} = 1.5\beta$ ,  $D_{21} = 0.5\beta$ ,  $D_{13} = D_{12}$ , and  $D_{23} = 4D_{21}$ . We follow the same fashion used in [9] by setting the final time as  $t_f = 50$  and time-step size as  $\Delta t = 0.005$ , which results in 10,000 iterations. In computations, the mesh constructed with crossed elements, which is shown in Figure 1a, is used. We directly employ the GFEM to solve this problem since it



(a)

(b)

**Figure 1.** Meshes: (a) constructed with  $n_{el} = 10,000$  crossed elements and  $n_{en} = 5,101$  nodes for solving *Application 1*, (b) constructed with  $n_{el} = 10,368$  elements and  $n_{en} = 5,329$  nodes for solving *Application 2*.

does not have convective terms. Figure 2 shows the component-wise GFEM solutions of *Application 1*, which is described by system (26), along with the corresponding absolute errors. It is observed that the absolute errors take their maximum values around corners of the computational domain. In Figure 3, the absolute errors in the GFEM approximation along the line  $x_2 = \pi$  are displayed. It is revealed that the maximum absolute error is around 0.001. In comparison to the results presented in [9], where the author employed B-spline basis functions of order  $k = 8$ , our results show good agreement with them (see Figure 3).

*Application 2 – Convection-diffusion with nonlinear reaction.* This second example is a stationary problem and is from [8] by Yücel et al.:

$$\begin{cases} -\epsilon_u \Delta u + \beta_u \cdot \nabla u + \alpha_u u + \gamma_u uv - f_u = 0, \\ -\epsilon_v \Delta v + \beta_v \cdot \nabla v + \alpha_v v + \gamma_v uv - f_v = 0, \end{cases} \quad (30)$$

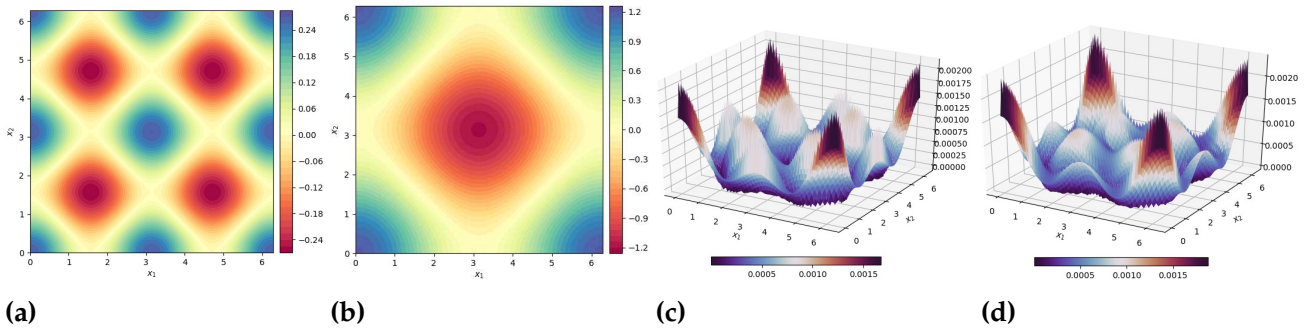


**Figure 2.** GFEM approximations for solving *Application 1*;  $t_f = 50$  and  $\Delta t = 0.005$ : (a) surface plot for  $u(x_1, x_2)$ , (b) surface plot for  $v(x_1, x_2)$ , (c) elevation plot for absolute error in  $u(x_1, x_2)$ , and (d) elevation plot for absolute error in  $v(x_1, x_2)$ .

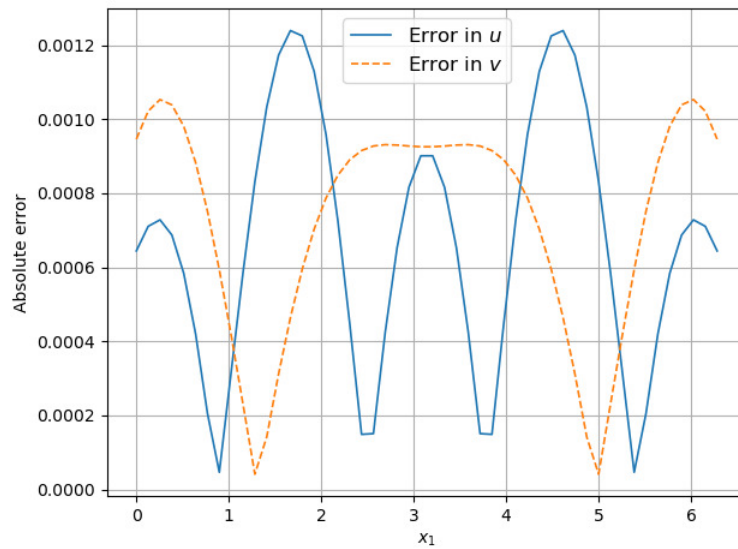


**Figure 3.** Comparison of absolute errors for solving *Application 1* along line  $x_2 = \pi$ .

where the unknown functions, i.e.,  $u(\mathbf{x})$  and  $v(\mathbf{x})$ , represents the reactant concentrations, the computational domain is taken as  $\Omega = (0, 1)$ , and the given functions  $f_u(\mathbf{x})$  and  $f_v(\mathbf{x})$  are the source functions. The parameters are set as follows: the diffusion coefficients are  $\epsilon_u = \epsilon_v = 10^{-5}$ , the convection vectors are  $\beta_u = [2, 3]$  and  $\beta_v = [1, 0]$ , the reaction coefficients  $\alpha_u = \alpha_v = 1.0$ , and  $\gamma_u = \gamma_v = 0.1$ . The source functions  $f_u$  and  $f_v$  are determined such that the following analytical solutions hold [8]:

$$u(x_1, x_2) = \frac{2}{\pi} \arctan \left( \frac{1}{\sqrt{\epsilon_u}} \left[ -\frac{1}{2}x_1 + x_2 - 0.25 \right] \right), \tag{31}$$

$$v(x_1, x_2) = 4 \exp \left( \frac{-1}{\sqrt{\epsilon_v}} \left( (x_1 - 0.5)^2 + 3(x_2 - 0.5)^2 \right) \right) \sin(\pi x_1) \cos(\pi x_2). \tag{32}$$

**Figure 1b** shows the mesh constructed with 10,368 triangular elements used in computations for solving *Application 2*. **Figure 4** presents a comparison of the performances of the proposed formulations for  $u(x_1, x_2)$ . It is clearly seen that the GFEM approximation is completely polluted with nonphysical oscillations. Although the SUPG formulation manages to eliminate spurious oscillations significantly, it requires additional treatment to resolve steep gradients. As to the SUPG- $\text{YZ}\beta$  formulation, there is not any significant oscillatory behavior, and the resulting approximation

is in good agreement with the exact solution. Since the  $v(x_1, x_2)$  component of the solution vector  $\mathbf{u}$  does not exhibit oscillatory behavior, only the exact solution and SUPG- $\text{YZ}\beta$  approximations are given in Figure 5, along with absolute errors in SUPG- $\text{YZ}\beta$  approximations for solving  $u(x_1, x_2)$  and  $v(x_1, x_2)$  components. We observe that the absolute errors almost completely vanish far from the regions where solutions exhibit rapid changes. In other words, the SUPG- $\text{YZ}\beta$  formulation looks for a compromise between stability and accuracy. While high-quality solution profiles are obtained similar to those reported in [8], the SUPG- $\text{YZ}\beta$  formulation achieves this on a coarser mesh without the need for any mesh refinement techniques.

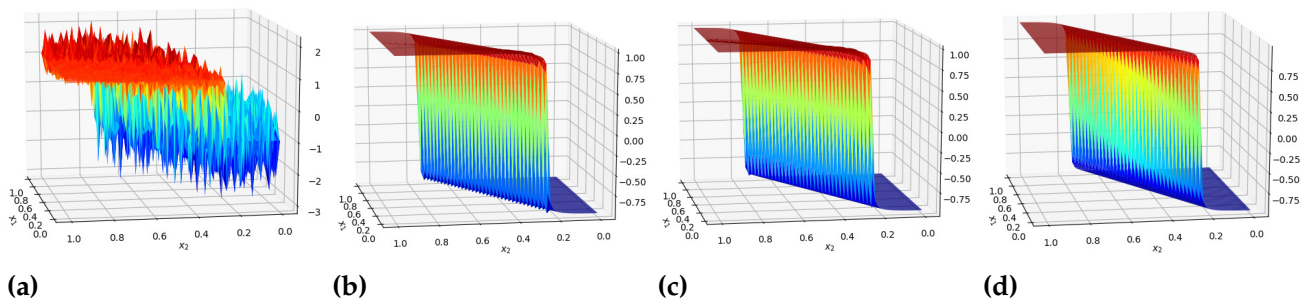


Figure 4. Comparison of approximations to  $u(x_1, x_2)$  obtained with various formulations for solving Application 2: (a) GFEM, (b) SUPG, (c) SUPG- $\text{YZ}\beta$ , and (d) exact solution.

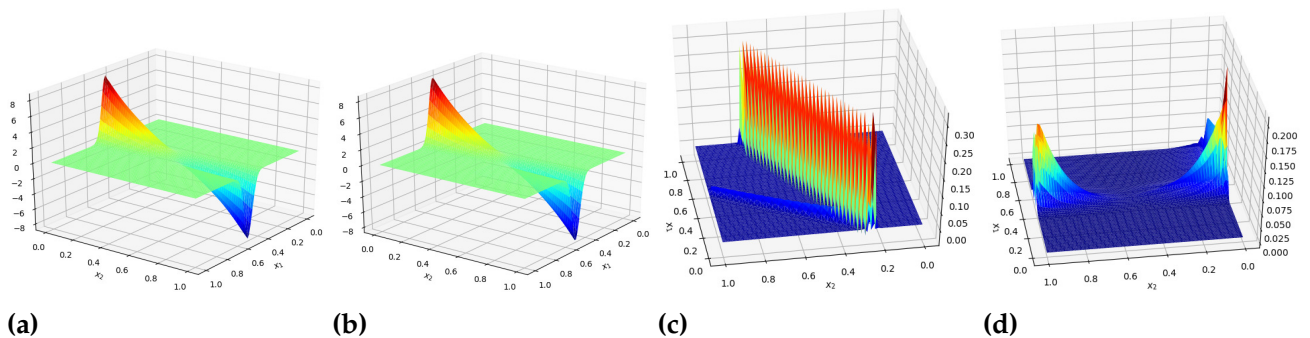


Figure 5. Comparison of SUPG- $\text{YZ}\beta$  approximations with exact solutions for solving Application 2: (a) SUPG- $\text{YZ}\beta$  solution for  $v(x_1, x_2)$ , (b) exact solution to  $v(x_1, x_2)$ , (c) absolute error in SUPG- $\text{YZ}\beta$  approximation for  $u(x_1, x_2)$ , and (d) absolute error in SUPG- $\text{YZ}\beta$  approximation for  $v(x_1, x_2)$ .

Application 3 – Schnakenberg reaction model. Here, we deal with the Schnakenberg reaction model, which was originally introduced by Schnakenberg in [52]. The model can be described as follows [5]:

$$\begin{cases} \frac{\partial u}{\partial t} + \mathbf{a} \cdot \nabla u - \Delta u - \gamma (\alpha - u + u^2 v) = 0, \\ \frac{\partial v}{\partial t} + \mathbf{a} \cdot \nabla v - d \Delta v - \gamma (\beta - u^2 v) = 0, \end{cases} \quad (33)$$

where the diffusion constant  $d$  refers to the relationship between the species diffusivities, the constants  $\alpha$  and  $\beta$  denote the production and consumption for species  $u$  and  $v$ , respectively, and the nonlinear term  $u^2 v$  is the catalysis term, which represents activation for  $u$  and consumption for

*v.* We consider this problem for two different sets of parameters and initial/boundary conditions. *Case I* aims to compare our results with those reported previously. Then, in *Case II*, the parameters and initial/boundary conditions are determined in such a way that the solution to the Schnakenberg model involves sharp gradients. For both computations, we suppose that the problems are defined on the domain  $\Omega = (0, 1)$ , the time-step size is taken as  $\Delta t = 0.005$ , and the final time is  $t_f = 2.5$ . Note that the parameter  $\beta$  given in the model is not related to  $YZ\beta$  shock-capturing.

**Case I:** The set of parameters are [5]:  $\alpha = 0.1$ ,  $\beta = 0.9$ ,  $\gamma = 230.82$ , and the velocity field is  $\mathbf{a} = [-\omega(x_2 - 0.5), \omega(x_1 - 0.5)]$ , where  $\omega = 0.6$ . In computations, a mesh having the same structure as that given in Figure 1b but constructed with 5,408 triangular elements and 2,809 nodes is used. Figure 6a–Figure 6b show the initial conditions for  $u$  and  $v$ , respectively. For determining these conditions, we perturb each reactive component around the steady-states by around 10% [53]. That is, the initial conditions are defined as follows:

$$u(x_1, x_2, t = 0) = u_s + \varepsilon u_s, \tag{34}$$

$$v(x_1, x_2, t = 0) = v_s + \varepsilon v_s, \tag{35}$$

where,  $(u_s, v_s) = \left( \alpha + \beta, \frac{\beta}{(\alpha + \beta)^2} \right)$ . Note that the reaction terms vanish for  $(u, v) = (u_s, v_s)$ . Homogeneous Neumann-type boundary conditions apply on walls.

In Figure 6c–6d, we present SUPG- $YZ\beta$  solutions to *Application 3* for *Case I*. Compared to the results reported in [5], the present solution profiles are in good agreement when a mesh constructed with a similar number of elements is used. This fact indicates that the proposed formulation does not distort the solutions by introducing unnecessary artificial diffusivity. The rotation of the Turing patterns is due to the velocity field  $\mathbf{a}$ , and these rotations are in the same direction as  $\mathbf{a}$ . On the other hand, numerical experiments reveal that when finer meshes are employed, all the proposed formulations yield slightly different approximations than those reported in [5]. The author believes that the slight difference in [5] is due to the coarser mesh used because of the limited computational resources available on those days when the numerical experiments were carried out.

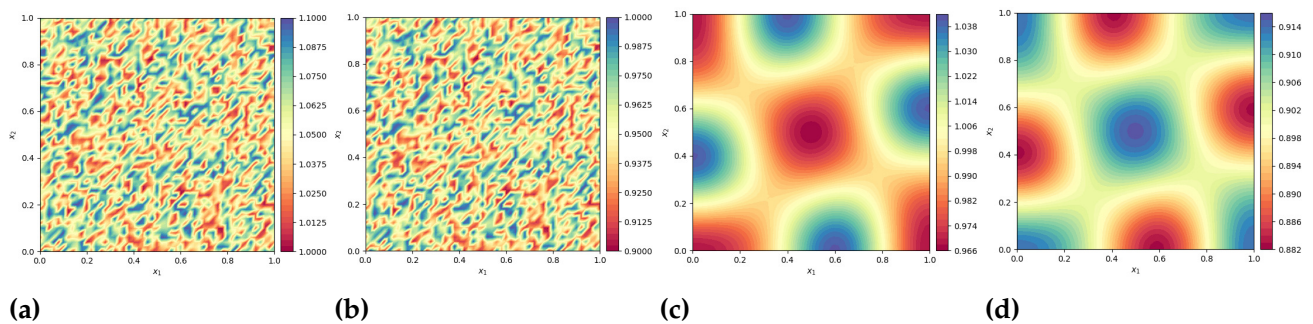


**Figure 6.** *Application 3 – Case I:* (a) initial condition for  $u(x_1, x_2, t)$ , (b) initial condition for  $v(x_1, x_2, t)$ , (c) SUPG- $YZ\beta$  approximation to  $u(x_1, x_2)$ , and (d) SUPG- $YZ\beta$  approximation to  $v(x_1, x_2)$ .

**Case II:** In this case, we modify the original system given by Eq. (33) as follows:

$$\begin{cases} \frac{\partial u}{\partial t} + \mathbf{a}_u \cdot \nabla u - d_u \Delta u - \gamma(\alpha - u + u^2 v) = 0, \\ \frac{\partial v}{\partial t} + \mathbf{a}_v \cdot \nabla v - d_v \Delta v - \gamma(\beta - u^2 v) = 0. \end{cases} \tag{36}$$

We set the parameters as:  $\alpha = 0.1$ ,  $\beta = 0.9$ ,  $\gamma = 0.52$ , the convection vectors are  $\mathbf{a}_u = [x_1, 2x_2]$  and  $\mathbf{a}_v = [x_1, 2x_1]$ , and the diffusion parameters are  $d_u = d_v = 10^{-8}$ . We use the same mesh used for *Case I*. The initial conditions are set as  $u(x_1, x_2, t = 0) = 1.0$  and  $v(x_1, x_2, t = 0) = 0.9$ . The Dirichlet-type boundary conditions are prescribed as follows:

$$g_u(x_1, x_2, t) = \begin{cases} 0.7, & \text{if } (x_1 > 0.1 \text{ and } x_2 > 0.4) \text{ or } x_2 < 0.6, \\ 1.0, & \text{otherwise,} \end{cases} \tag{37}$$

$$g_v(x_1, x_2, t) = \begin{cases} 0.6, & \text{if } x_1 = 1, \\ 0.9, & \text{otherwise.} \end{cases} \tag{38}$$

In **Figure 7**, we compare the SUPG and SUPG- $\text{YZ}\beta$  approximations for solving *Case II* of *Application 3*. The N–R algorithm fails to converge for the GFEM formulation. It can be observed that the sharp gradients in solutions, particularly those obtained for  $u(x_1, x_2, t)$ , are resolved accurately without any significant localized oscillations by employing the SUPG- $\text{YZ}\beta$  formulation.

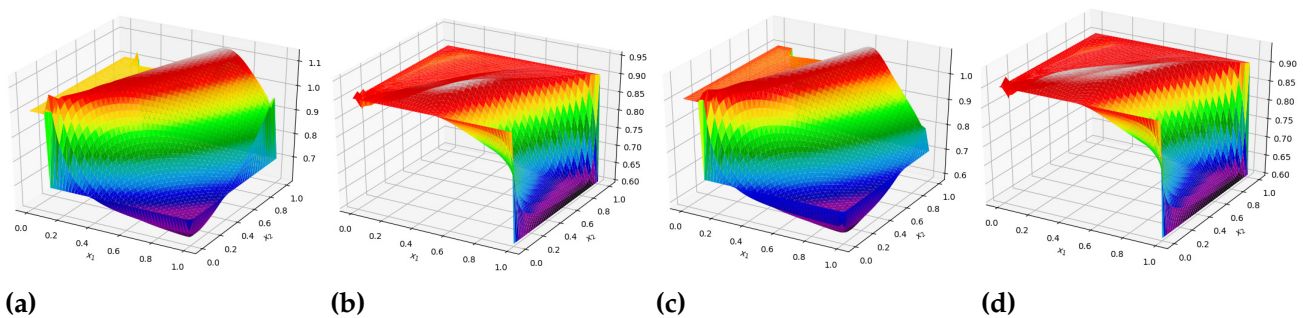


**Figure 7.** *Application 3 – Case II:* (a) SUPG approximation to  $u(x_1, x_2, t)$ , (b) SUPG approximation to  $v(x_1, x_2, t)$ , (c) SUPG- $\text{YZ}\beta$  approximation to  $u(x_1, x_2)$ , and (d) SUPG- $\text{YZ}\beta$  approximation to  $v(x_1, x_2)$ .

*Application 4 – A mussel-algae interaction model.* This 1D model, which was originally introduced in [54] by Koppel et al., is taken from [10] in its nondimensionalized form:

$$\begin{cases} \frac{\partial u}{\partial t} = D_{11} \frac{\partial^2 u}{\partial x_1^2} - q \frac{\partial u}{\partial x_1} + \alpha(1 - u) - uv, \\ \frac{\partial v}{\partial t} = D_{21} \frac{\partial^2 v}{\partial x_1^2} + \sigma uv - \gamma v^2 - \frac{v}{v + 1}, \end{cases} \tag{39}$$

where  $0 < x_1 < L = 10$  and  $t > 0$ . The unknown functions  $u(x_1, t)$  and  $v(x_1, t)$  represent the algae and mussel density, respectively,  $\alpha$  is the exchange rate of mussels, and  $\gamma$  denotes the competition between the mussels (intraspecific competition). One of the primary food sources that mussels consume is algae. Following [10], it is assumed that algae constantly convects at the rate of  $q$ , at which algae is supplied to the mussels bed by unidirectional water flow, from the open sea toward the shore. We consider system (39) for three different sets of parameter and boundary conditions. In the first two cases, we verify the proposed formulation and solvers by comparing the results obtained with those reported by Wang et al. [10]. As to the third scenario, we modify the originally introduced parameter set and conditions such that system (39) becomes convection-dominated. For all cases, the number of elements is  $n_{el} = 256$  and time step-size is set

to  $\Delta t = 0.1$ .

**Case I:** In the first case, system (39) is subject to homogeneous Neumann boundary condition at  $x_1 = L$  and Danckwerts-type inflow boundary condition applies at  $x_1 = 0$  (for further details, see [10, 55]):

$$D_{11} \frac{\partial u(0, t)}{\partial x_1} = qu(0, t), \quad (40)$$

$$\frac{\partial u(L, t)}{\partial x_1} = 0. \quad (41)$$

The parameter set is taken from [10]:  $D_{11} = 0.1$ ,  $D_{21} = 0.3$ ,  $\alpha = 0.6$ ,  $\sigma = 0.5$ , and  $\gamma = 0.2$ . In numerical experiments, we study various values of the advection rate  $q$ , i.e.,  $q = 10^{-4}$ ,  $q = 2$ , and  $q = 6$ . The initial conditions are  $u(x_1, 0) = 0.1$  and  $v(x_1, 0) = 1.0$ . The simulations are run for the terminal time  $t_f = 100$ .

Figure 8 shows that, for a range of convection rate constant  $q$ , the mussels die out and only the algae remain. It implies that mussels cannot exist when the rate at which ingested algae are converted to mussels and their production is less than the rate at which they are consumed. Nonetheless, the algae's biomass is affected by the water flow, i.e., the biomass of the algae decreases as the advection rate  $q$  increases.

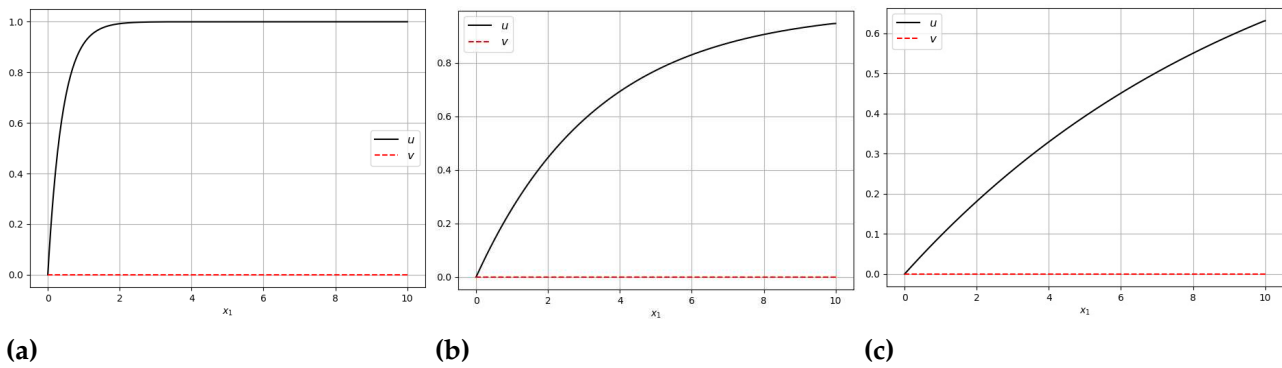


**Figure 8.** Comparison of SUPG- $YZ\beta$  approximations for solving Application 4 – Case I: (a)  $q = 10^{-4}$ , (b)  $q = 2$ , and (c)  $q = 6$ .

**Case II:** In this case, we consider the same boundary conditions used in the first case. The initial conditions are  $u(x_1, 0) = 0.8$  and  $v(x_1, 0) = 0.6$ . As to the parameters, we only change the conversion constant  $\sigma$  to  $\sigma = 2.0$ . The terminal time is set to  $t_f = 100$ .

Figure 9 presents the SUPG- $YZ\beta$  approximations for various values of the convection constant  $q$ . These figures indicate that algae are carried downstream by the water as the advection rate increases. Because of this, mussels have more food available downstream, which causes them to accumulate downstream as well. In both cases (*Case I* and *Case II*), we observe that the results are in pretty good agreement with those reported in [10]. We, in the last case, examine the system given by Eq. (39) for convection dominance.

**Case III:** For this case, the initial conditions are  $u(x_1, 0) = 0.1$  and  $v(x_1, 0) = 1.0$ . The parameter set is:  $D_{11} = 10^{-7}$ ,  $D_{21} = 3 \times 10^{-7}$ ,  $\alpha = 1.6$ ,  $\gamma = 1.2$ ,  $\sigma = 2.0$ , and  $q = 10$ . The Dirichlet-type boundary conditions are prescribed as follows:

$$g_u(x_1 = 0, t) = 0, \quad g_u(x_1 = L, t) = 0, \quad (42)$$

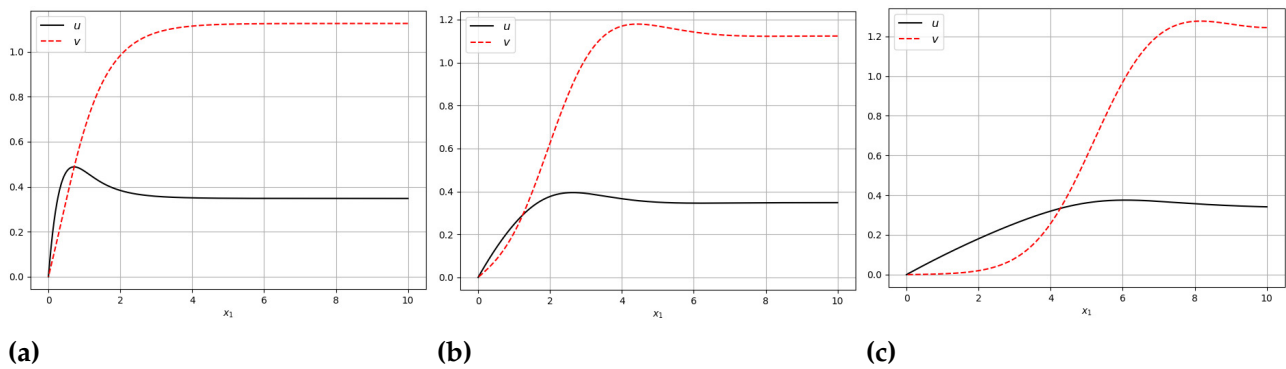


**Figure 9.** Comparison of SUPG- $YZ\beta$  approximations for solving Application 4 – Case II: (a)  $q = 10^{-4}$ , (b)  $q = 2$ , and (c)  $q = 6$ .

and

$$g_v(x_1 = 0, t) = 0, \quad g_v(x_1 = L, t) = 0. \quad (43)$$

The terminal time is set as  $t_f = 10$ .

In **Figure 10a**, it is observed that the GFEM yields approximations completely polluted with node-to-node spurious oscillations. During the numerical simulations, it was revealed that when the number of elements was increased, the situation got even worse. On the other hand, it is seen in **Figure 10b** that the SUPG formulation performs quite well, eliminating almost all nonphysical oscillations but a very tight region near  $x_1 = 10$ . Finally, we observe the effect of the shock-capturing mechanism in **Figure 10c**; it helps capture the steep gradient that occurs near  $x_1 = 10$  successfully without introducing excessive dissipation.

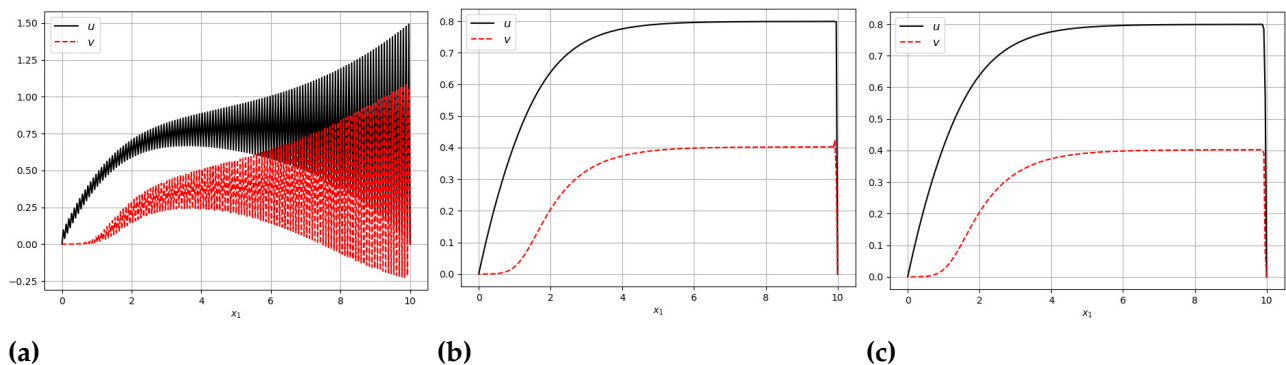


**Figure 10.** Comparison of approximations for solving Application 4 – Case III obtained with: (a) GFEM, (b) SUPG, and (c) SUPG- $YZ\beta$ .

## 5 Concluding remarks

We have proposed a streamline-upwind/Petrov–Galerkin finite element formulation supplemented with  $YZ\beta$  shock-capturing, the so-called SUPG- $YZ\beta$  formulation, for solving coupled systems of reaction-convection-diffusion equations. For comparison purposes, we first tested the accuracy of the proposed formulation and verified the solver codes for numerical experiments available in the literature. In order to assess the genuine performance of the proposed formulation and demonstrate that the standard Galerkin finite element formulation fails in convection dominance, we have modified the original problems by making them convection-dominated.

We have observed that the SUPG- $YZ\beta$  formulation successfully eliminates spurious oscillations. The method accomplishes this by making use of only linear interpolation functions and meshes that are relatively coarser than those used in the majority of reported studies, without the need for any fitted or adaptive mesh strategies. In addition to these, it is also noted that the proposed shock-capturing mechanism does not cause the solutions to become distorted by introducing excessive numerical dissipation. Besides that, although any adaptive mesh strategies are not adopted, coarser meshes are used compared to the reported studies, and only linear interpolation functions are employed, the approximations obtained do not exhibit any significant numerical instabilities for more challenging cases.

Our future research is planned to focus on tumor growth phenomena, which can be represented by a coupled system of partial differential equations of the reaction-convection-diffusion type.

## Declarations

### List of abbreviations

Not applicable.

### Ethical approval

The author states that this research complies with ethical standards. This research does not involve either human participants or animals.

### Consent for publication

Not applicable.

### Conflicts of interest

The author confirms that there is no competing interest in this study.

### Data availability statement

Data availability is not applicable to this article as no new data were created or analyzed in this study.

### Funding

Not applicable.

### Author's contributions

The author has made substantial contributions to the conception, design of the work, the acquisition, analysis, interpretation of data, and the creation of new software used in the work.

## References

- [1] Painter, K.J. Mathematical models for chemotaxis and their applications in self-organisation phenomena. *Journal of Theoretical Biology*, 481, 162-182, (2019). [[CrossRef](#)]
- [2] Bellomo, N., Outada, N., Soler, J., Tao, Y. and Winkler, M. Chemotaxis and cross-diffusion models in complex environments: Models and analytic problems toward a multiscale vision. *Mathematical Models and Methods in Applied Sciences*, 32(04), 713-792, (2022). [[CrossRef](#)]
- [3] Trelles, J.P. Pattern formation and self-organization in plasmas interacting with surfaces. *Journal of Physics D: Applied Physics*, 49(39), 393002, (2016). [[CrossRef](#)]

- [4] Van Gorder, R.A. Influence of temperature on Turing pattern formation. *Proceedings of the Royal Society A: Mathematical, Physical and Engineering Sciences*, 476(2240), 20200356, (2020). [[CrossRef](#)]
- [5] Garzón-Alvarado, D.A., Galeano, C.H. and Mantilla, J.M. Turing pattern formation for reaction-convection-diffusion systems in fixed domains submitted to toroidal velocity fields. *Applied Mathematical Modelling*, 35(10), 4913-4925, (2011). [[CrossRef](#)]
- [6] Sarra, S.A. A local radial basis function method for advection-diffusion-reaction equations on complexly shaped domains. *Applied Mathematics and Computation*, 218(19), 9853-9865, (2012). [[CrossRef](#)]
- [7] Chapwanya, M., Lubuma, J.M.S. and Mickens, R.E. Positivity-preserving nonstandard finite difference schemes for cross-diffusion equations in biosciences. *Computers & Mathematics with Applications*, 68(9), 1071-1082, (2014). [[CrossRef](#)]
- [8] Yücel, H., Stoll, M. and Benner, P. A discontinuous Galerkin method for optimal control problems governed by a system of convection–diffusion PDEs with nonlinear reaction terms. *Computers & Mathematics with Applications*, 70(10), 2414-2431, (2015). [[CrossRef](#)]
- [9] Hidayat, M.I.P. Meshless finite difference method with B-splines for numerical solution of coupled advection-diffusion-reaction problems. *International Journal of Thermal Sciences*, 165, 106933, (2021). [[CrossRef](#)]
- [10] Wang, J., Tong, X. and Song, Y. Dynamics and pattern formation in a reaction-diffusion-advection mussel-algae model. *Zeitschrift für angewandte Mathematik und Physik*, 73, 117, (2022). [[CrossRef](#)]
- [11] Clavero, C., Shiromani, R. and Shanthi, V. A numerical approach for a two-parameter singularly perturbed weakly-coupled system of 2-D elliptic convection-reaction-diffusion PDEs. *Journal of Computational and Applied Mathematics*, 436, 115422, (2024). [[CrossRef](#)]
- [12] Cengizci, S., Uğur, Ö. and Natesan, S. SUPG- $\text{YZ}\beta$  computation of chemically reactive convection-dominated nonlinear models. *International Journal of Computer Mathematics*, 100(2), 283-303, (2023). [[CrossRef](#)]
- [13] Uzunca, M., Karasözen, B. and Manguoğlu, M. Adaptive discontinuous Galerkin methods for non-linear diffusion-convection-reaction equations. *Computers & Chemical Engineering*, 68, 24-37, (2014). [[CrossRef](#)]
- [14] Yücel, H., Stoll, M. and Benner, P. Discontinuous Galerkin finite element methods with shock-capturing for nonlinear convection dominated models. *Computers & Chemical Engineering*, 58, 278-287, (2013). [[CrossRef](#)]
- [15] Joshi, H. and Jha, B.K. Chaos of calcium diffusion in Parkinson's infectious disease model and treatment mechanism via Hilfer fractional derivative. *Mathematical Modelling and Numerical Simulation With Applications*, 1(2), 84-94, (2021). [[CrossRef](#)]
- [16] Joshi, H. and Jha, B.K. Modeling the spatiotemporal intracellular calcium dynamics in nerve cell with strong memory effects. *International Journal of Nonlinear Sciences and Numerical Simulation*, 24(6), 2383-2403, (2021). [[CrossRef](#)]
- [17] Joshi, H., Yavuz, M. and Stamova, I. Analysis of the disturbance effect in intracellular calcium dynamic on fibroblast cells with an exponential kernel law. *Bulletin of Biomathematics*, 1(1), 24-39, (2023). [[CrossRef](#)]
- [18] Brooks, A.N. and Hughes, T.J. Streamline upwind/Petrov-Galerkin formulations for convection dominated flows with particular emphasis on the incompressible Navier-Stokes

- equations. *Computer Methods in Applied Mechanics and Engineering*, 32(1-3), 199-259, (1982). [[CrossRef](#)]
- [19] Hughes, T.J.R. and Brooks A.N. A multi-dimensional upwind scheme with no crosswind diffusion. In: *Finite Element Methods for Convection Dominated Flows*, (pp. 19-35). AMD-Vol. 34, New York, USA: ASME, (1979).
- [20] Tezduyar, T.E. and Hughes, T.J.R. Development of time-accurate finite element techniques for first-order hyperbolic systems with particular emphasis on the compressible Euler equations. *NASA Technical Report NASA-CR-204772*, NASA, 510, (1982).
- [21] Tezduyar, T. and Hughes, T. Finite element formulations for convection dominated flows with particular emphasis on the compressible Euler equations. In: *Proceedings of AIAA 21st Aerospace Sciences Meeting*, AIAA Paper 83-0125, Reno, Nevada, 1983. [[CrossRef](#)]
- [22] Hughes, T.J.R. and Tezduyar, T.E. Finite element methods for first-order hyperbolic systems with particular emphasis on the compressible Euler equations. *Computer Methods in Applied Mechanics and Engineering*, 45(1-3), 217-284, (1984). [[CrossRef](#)]
- [23] Hughes, T.J.R., Franca, L.P. and Mallet, M. A new finite element formulation for computational fluid dynamics: VI. Convergence analysis of the generalized SUPG formulation for linear time-dependent multidimensional advective-diffusive systems. *Computer Methods in Applied Mechanics and Engineering*, 63(1), 97-112, (1987). [[CrossRef](#)]
- [24] Le Beau, G.J. and Tezduyar, T.E. Finite element computation of compressible flows with the SUPG formulation. In: *Advances in Finite Element Analysis in Fluid Dynamics*, (pp. 21-27). FED-Vol. 123, New York, USA: ASME, (1991).
- [25] Tezduyar, T.E. and Park, Y. Discontinuity-capturing finite element formulations for non-linear convection-diffusion-reaction equations. *Computer Methods in Applied Mechanics and Engineering*, 59(3), 307-325, (1986). [[CrossRef](#)]
- [26] Tezduyar, T.E. Finite elements in fluids: Stabilized formulations and moving boundaries and interfaces. *Computers & Fluids*, 36(2), 191-206, (2003). [[CrossRef](#)]
- [27] Tezduyar, T.E. Finite element methods for fluid dynamics with moving boundaries and interfaces. In: E Stein, RD Borst, TJR Hughes (Eds.), *Encyclopedia of Computational Mechanics*, Volume 3: Fluids, Wiley, (2004). [[CrossRef](#)]
- [28] Rispoli, F., Corsini, A. and Tezduyar, T.E. Finite element computation of turbulent flows with the discontinuity-capturing directional dissipation (DCDD). *Computers & Fluids*, 36(1), 121-126, (2007). [[CrossRef](#)]
- [29] Tezduyar, T.E. Computation of moving boundaries and interfaces and stabilization parameters. *International Journal for Numerical Methods in Fluids*, 43(5), 555-575, (2003). [[CrossRef](#)]
- [30] Tezduyar, T.E. and Senga, M. Stabilization and shock-capturing parameters in SUPG formulation of compressible flows. *Computer Methods in Applied Mechanics and Engineering*, 195(13-16), 1621-1632, (2006). [[CrossRef](#)]
- [31] Tezduyar, T.E. and Senga, M. SUPG finite element computation of inviscid supersonic flows with  $\text{YZ}\beta$  shock-capturing. *Computers & Fluids*, 36(1), 147-159, (2007). [[CrossRef](#)]
- [32] Tezduyar, T.E., Senga, M. and Vicker, D. Computation of inviscid supersonic flows around cylinders and spheres with the SUPG formulation and  $\text{YZ}\beta$  shock-capturing. *Computational Mechanics*, 38, 469-481, (2006). [[CrossRef](#)]
- [33] Bazilevs, Y., Calo, V.M., Tezduyar, T.E. and Hughes, T.J.R.  $\text{YZ}\beta$  discontinuity capturing for advection-dominated processes with application to arterial drug delivery. *International Journal*

for *Numerical Methods in Fluids*, 54(6-8), 593-608, (2007). [[CrossRef](#)]

- [34] Cengizci, S. and Uğur, Ö. A stabilized FEM formulation with discontinuity-capturing for solving Burgers'-type equations at high Reynolds numbers. *Applied Mathematics and Computation*, 442, 127705, (2023). [[CrossRef](#)]
- [35] Cengizci, S. and Uğur, Ö. SUPG formulation augmented with  $YZ\beta$  shock-capturing for computing shallow-water equations. *ZAMM-Journal of Applied Mathematics and Mechanics/Zeitschrift für Angewandte Mathematik und Mechanik*, 103(6), e202200232, (2023). [[CrossRef](#)]
- [36] Cengizci, S., Uğur, Ö. and Natesan, S. A SUPG formulation augmented with shock-capturing for solving convection-dominated reaction-convection-diffusion equations. *Computational and Applied Mathematics*, 42, 235, (2023). [[CrossRef](#)]
- [37] Tezduyar, T.E., Ramakrishnan, S. and Sathe, S. Stabilized formulations for incompressible flows with thermal coupling. *International Journal for Numerical Methods in Fluids*, 57(9), 1189-1209, (2008). [[CrossRef](#)]
- [38] John, V. and Knobloch, P. On spurious oscillations at layers diminishing (SOLD) methods for convection-diffusion equations: Part I-A review. *Computer Methods in Applied Mechanics and Engineering*, 196(17-20), 2197-2215, (2007). [[CrossRef](#)]
- [39] John, V. and Knobloch, P. On spurious oscillations at layers diminishing (SOLD) methods for convection-diffusion equations: Part II-Analysis for  $P1$  and  $Q1$  finite elements. *Computer Methods in Applied Mechanics and Engineering*, 197(21-24), 1997-2014, (2008). [[CrossRef](#)]
- [40] John, V., Knobloch, P. and Novo, J. Finite elements for scalar convection-dominated equations and incompressible flow problems: a never ending story?. *Computing and Visualization in Science*, 19, 47-63, (2018). [[CrossRef](#)]
- [41] Ak, T., Karakoç, S.B.G. and Biswas, A. Application of Petrov-Galerkin finite element method to shallow water waves model: Modified Korteweg-de Vries equation. *Scientia Iranica B*, 24(3), 1148-1159, (2017). [[CrossRef](#)]
- [42] Bhowmik, S.K. and Karakoc, S.B.G. Numerical approximation of the generalized regularized long wave equation using Petrov-Galerkin finite element method. *Numerical Methods for Partial Differential Equations*, 35(6), 2236-2257, (2019). [[CrossRef](#)]
- [43] Karakoc, S.B.G., Saha, A. and Sucu, D. A novel implementation of Petrov-Galerkin method to shallow water solitary wave pattern and superperiodic traveling wave and its multistability: Generalized Korteweg-de Vries equation. *Chinese Journal of Physics*, 68, 605-617, (2020). [[CrossRef](#)]
- [44] Shakib, F. *Finite element analysis of the compressible Euler and Navier-Stokes equations*. Ph.D. Thesis, Department of Mechanical Engineering, Stanford University: California, (1988).
- [45] Franca, L.P., Frey, S.L. and Hughes, T.J. Stabilized finite element methods: I. Application to the advective-diffusive model. *Computer Methods in Applied Mechanics and Engineering*, 95(2), 253-276, (1992). [[CrossRef](#)]
- [46] Tezduyar, T.E. Stabilized finite element formulations for incompressible flow computations. *Advances in Applied Mechanics*, 28, 1-44, (1991). [[CrossRef](#)]
- [47] Donea, J. and Huerta, A. *Finite Element Methods for Flow Problems*. John Wiley & Sons: England, (2003). [[CrossRef](#)]
- [48] Abali, B.E. *Computational Reality: Solving Nonlinear and Coupled Problems in Continuum Mechanics*. Advanced Structured Materials, Springer: Singapore, (2016). [[CrossRef](#)]

- [49] Alnæs, M., Blechta, J., Hake, J., Johansson, A., Kehlet, B., Logg, A. et al. The FEniCS project version 1.5. *Archive of Numerical Software*, 3(100), 9-23, (2015). [[CrossRef](#)]
- [50] Logg, A., Mardal, K.A. and Wells, G. *Automated solution of differential equations by the finite element method: The FEniCS book* (Vol. 84). Lecture Notes in Computational Science and Engineering, Springer-Verlag: Berlin, Heidelberg, (2012). [[CrossRef](#)]
- [51] Zhang, J. and Yan, G. Lattice Boltzmann simulation of pattern formation under cross-diffusion. *Computers & Mathematics with Applications*, 69(3), 157-169, (2015). [[CrossRef](#)]
- [52] Schnakenberg, J. Simple chemical reaction systems with limit cycle behaviour. *Journal of Theoretical Biology*, 81(3), 389-400, (1979). [[CrossRef](#)]
- [53] Garzón-Alvarado, D.A., Galeano, C.H. and Mantilla, J.M. Computational examples of reaction-convection-diffusion equations solution under the influence of fluid flow: First example. *Applied Mathematical Modelling*, 36(10), 5029-5045, (2013). [[CrossRef](#)]
- [54] Koppel, J.V.D., Rietkerk, M., Dankers, N. and Herman, P.M.J. Scale-dependent feedback and regular spatial patterns in young mussel beds. *The American Naturalist*, 165(3), E66-E77, (2005). [[CrossRef](#)]
- [55] Jones, D.A., Smith, H.L., Dung, L. and Ballyk, M. Effects of random motility on microbial growth and competition in a flow reactor. *SIAM Journal on Applied Mathematics*, 59(2), 573-596, (1998). [[CrossRef](#)]
- [56] Murray, J.D. *Mathematical Biology II: Spatial Models and Biomedical Applications. Interdisciplinary Applied Mathematics*, New York, NY, USA: Springer, (2013). [[CrossRef](#)]
- [57] Vanegas, J.C., Landinez, N.S. and Garzón-Alvarado, D.A. Modelo matemático de la coagulación en la interfase hueso implante dental. *Revista Cubana de Investigaciones Biomédicas*, 28(3), 167-191, (2009).

Mathematical Modelling and Numerical Simulation with Applications (MMNSA)

(<https://dergipark.org.tr/en/pub/mmnsa>)



**Copyright:** © 2023 by the authors. This work is licensed under a Creative Commons Attribution 4.0 (CC BY) International License. The authors retain ownership of the copyright for their article, but they allow anyone to download, reuse, reprint, modify, distribute, and/or copy articles in MMNSA, so long as the original authors and source are credited. To see the complete license contents, please visit (<http://creativecommons.org/licenses/by/4.0/>).

**How to cite this article:** Cengizci, S. (2023). An enhanced SUPG-stabilized finite element formulation for simulating natural phenomena governed by coupled system of reaction-convection-diffusion equations. *Mathematical Modelling and Numerical Simulation with Applications*, 3(4), 297-317. <https://doi.org/10.53391/mmnsa.1387125>



RESEARCH PAPER

## Optimal control of diabetes model with the impact of endocrine-disrupting chemical: an emerging increased diabetes risk factor

P. Logaprakash <sup>1,†</sup> and C. Monica <sup>1,\*,‡</sup>

<sup>1</sup>Department of Mathematics, School of Advanced Sciences, Vellore Institute of Technology, Vellore 632 014, Tamil Nadu, India

\*Corresponding Author

‡logaprakash.p@vit.ac.in (P. Logaprakash); monica.c@vit.ac.in (C. Monica)

### Abstract

Diabetes, a persistent pathological condition characterized by disruptions in insulin hormone regulation, has exhibited a noteworthy escalation in its prevalence over recent decades. The surge in incidence is notably associated with the proliferation of endocrine-disrupting chemicals (EDCs), which have emerged as primary contributors to the manifestation of insulin resistance and the consequent disruption of beta cell function, ultimately culminating in the onset of diabetes. Consequently, this study endeavors to introduce a model for diabetes that aims to elucidate the ramifications of exposure to EDCs within the diabetic population. In the pursuit of mitigating the deleterious effects of EDC-induced diabetes, we propose a framework for optimal control strategies. The utilization of Pontryagin's maximum principle serves to explicate the principles governing the optimal control mechanisms within the proposed model. Our findings underscore that heightened concentrations of EDCs play a pivotal role in exacerbating the prevalence of diabetes. To substantiate our model, we employ parameter estimation techniques utilizing a diabetes dataset specific to the demographic context of India. This research contributes valuable insights into the imperative need for proactive measures to regulate and diminish EDC exposure, thereby mitigating the escalating diabetes epidemic.

**Keywords:** Diabetes; endocrine-disrupting chemical; mathematical model; optimal control; simulation

**AMS 2020 Classification:** 37M05; 37N25; 49K10; 92C60

### 1 Introduction

Disease has always been a part of human life. Malaria, tuberculosis, plague, and other infectious diseases have decimated human life. The researcher is beginning to predict how the disease will progress and understand how interventions will affect its spread. The mechanisms and kinds of interaction terms vary depending on the disease. Diabetes (a chronic disease) has become

a significant burden for individuals, leading to a variety of health problems in recent years [1]. Diabetes and its consequences have increased globally, likely because of the increasing diabetes risk factors, particularly population aging and obesity. It is a disorder characterized by insulin hormone problems, according to the World Health Organisation (WHO) [2]. According to the American Diabetes Association (ADA) [3], it is a group of metabolic disorders characterized by hyperglycemia secondary to diabetes. Factors that increase one's likelihood of developing diabetes include getting older, leading an unhealthy life, not getting enough exercise, eating a high-calorie diet, having stress, being overweight, and so on [4].

Despite incredible advances in biomedical sciences, diabetes remains an irreversible lifetime disease. Over the past 30 years, the number of people with diabetes has risen quickly in all age and gender groups, as well as in developing and developed countries. According to the International Diabetes Federation (IDF) [5], the prevalence of diabetes has risen even more by over 40 million people over the past quarter century. More than 540 million people had diabetes in 2021. If the current growth rate continues, this number will reach 780 million by 2045. According to the WHO [2], 1.6 million people died of diabetes in 2016, making it the seventh leading cause of death. In 2015, the Malaysian National Health Movement Survey (NHMS) found that 17.5% of adults over the age of 18 had diabetes [6]. Following that, the Malaysian province predicted a 10-year diabetes prevalence project and estimated that the diabetic population will increase by 31.3 percent by 2025 [7]. In 2021, diabetes caused the deaths of 6.7 million people worldwide [5]. It is associated with a 75 percent increase in adult mortality [8]. Hyperglycemia can lead to complications. Retinopathy, nephropathy, neuropathy, and an increased incidence of heart disease and stroke are other complications [9].

During this time of rising diabetes rates, humanity has witnessed large production and release of Endocrine-disrupting chemicals. Endocrine-disrupting chemicals (EDCs) can be either man-made or natural. Because their structure is nearly identical to steroid hormones, they could perhaps interact with hormones, androgen, and progesterone receptors, interfering with any aspect of endogenous hormone function, including biosynthesis, metabolism, transport, elimination, or receptor binding of endogenous hormones, increasing the risk of endocrine and metabolic diseases in humans and animals [10]. An endocrine disruptor is any chemical or chemical mixture from the outside that can interfere with hormones work [11]. According to the European Union, 147 of the 564 chemicals proposed by various organizations as potential EDC in scientific research or reports remain in the ecosystem or are produced in large quantities [12]. Plasticizers (Phthalates and Bisphenol A (BPA) or its derivative bisphenol S (BPS)) and pesticides such as dichlorodiphenyltrichloroethane (DDT), etc. are the most dangerous hazards to human health [13]. Prolonged repeated exposure to EDC compounds with concentrations even lower than the human body's established tolerance threshold for individual substances will also significantly increase the risk of hormonal and metabolic diseases such as diabetes both in men and women [14].

In addition, the development of modern civilization and the growing demand for new chemicals have raised our vulnerability to EDC. The release of these chemicals from everyday objects like food packaging, plastic water bottles, makeup, cash register receipts, clothing, food, contact lenses and dental sealants increases exposure [15]. Some EDCs may be more common in babies and young children than adults due to increased consumption of specific foods and water [16]. Researchers discovered that higher plasma concentrations of perfluorooctanesulfonic acid (PFOS) and perfluorooctanoic acid (PFOA) were associated with an increased risk of Type 2 diabetes (T2D) after controlling for common T2D risk factors such as BMI, family history and physical activity [17]. Prolonged repeated exposure to EDC compounds with concentrations even lower than the human body's established tolerance threshold for individual substances will also significantly increase the risk of hormonal and metabolic diseases such as diabetes both in men and women [14].

Researchers discovered that exposure to any pesticide was associated with a 61% increased risk of T2D in a meta-analysis of 21 prior studies involving over 66,000 people, with some pesticides appearing riskier than others [18].

In many models, authors have tried to describe how diabetes increases among people. Boutayeb et al. [19, 20] introduced a diabetic model, demonstrating the incidence of diabetes and its complications. Derouich et al. [21] proposed an optimal control approach to model the progression of diabetes from prediabetes, with or without control. Widyaningsih et al. [22] analyzed a mathematical model of diabetes with lifestyle and genetic factors. Bassey [23] analyzed the optimal control model for dual treatment of delayed type-II diabetes. Jajarmi et al. [24] created a new and efficient numerical method for the fractional modeling of diabetes and tuberculosis co-existence. Akinsola et al. [25] executed a mathematical analysis with numerical solutions of the diabetes mellitus model with optimal control. Ndi et al. [26] have tried to control the effect of hard water. Anusha et al. [27] studied mathematical modelling co-existence of diabetes and COVID-19 in deterministic and stochastic Approaches. Özköse et al. [28] investigated the interaction between COVID-19 and diabetes using real data. Agwu et al. [29] also analyzed the diabetes and tuberculosis co-existence model. Mollah et al. [30] studied the Optimal control for the diabetes model with an awareness program and treatment. Singh et al. [31] investigated the calcium distribution in the alpha-cell. Balakrishnan et al. [32] created a fractional-order control model for diabetes. A growing body of evidence suggests that environmental chemicals are linked to the rising prevalence of T2D. Therefore, We used the basic diabetes model [19, 21] to develop the model. Our primary goal in this paper is to reduce EDC exposure to reduce diabetes prevalence. The novelty of the proposed model is outlined by the following points:

- A new model was developed to determine the impact of EDC exposure on the diabetes population.
- A food population which gives a more realistic insist for the prevalence of diabetes.
- An optimal control problem is introduced with Possible control variables to reduce the effect of EDC and the prevalence of diabetes.
- The results for simulating different compartments of the model for the parameters  $b$  and  $r$  describe the effect of EDC Exposure.
- The proposed model provides some new ideas about the dynamic behavior of diabetes.

In [Section 2](#), the model's formulation is built and briefly discussed. In [Section 3](#), an optimal control problem is proposed. Furthermore, we established some results for the existence and characterization of optimal control. The numerical simulation is performed to validate the theoretical results discussed in [Section 4](#).

## 2 Model formulation

We construct a diabetes model predicting the growing diabetic population, which suggests that higher EDC concentration levels in our daily routine (food, water, etc.) may be linked to the prevalence of diabetes. The impact of EDC usage is a chief concern since a growing body of evidence from studies has also shown a link between early EDC exposure and the prevalence of T2D late in life. Thus, we have developed a class  $F$  to describe the level of EDC present in the usual diet and lifestyle. The concentration of EDC intake increases at rate  $b$  and is limited by carrying capacity  $K$ , which equals the maximum solubility of each compound in food, air, soil, water and so on. When consuming EDC-exposed products at a rate of  $\beta_H \frac{F}{F+K}$ , people become exposed.  $\beta_H$  represents the rate at which healthy individuals consume EDC daily. The probability of individuals exposed to EDC is determined by the equation  $\frac{F}{F+K}$ , where  $K$  is the maximum concentration of EDC in a food product. The maximum chance of developing diabetes is set at 0.5.

Therefore, the maximum EDC concentration in a food product was equal to its carrying capacity  $K$ . It is also feasible to transition back to a normal lifestyle at a rate of  $\alpha_3$ , provided that one is cognizant of EDC and adopts a health-conscious way of living. The variables and parameters of our model are outlined in [Table 1](#) and [Table 2](#).

**Table 1.** Model variables and their descriptions

Variables	Description
P	Healthy popoulation
S	Pre-diabetes population
D	Diabetes population
C	Diabetes population with complication
E	Exposed population
F	Food exposed with EDC

**Table 2.** Model parameters, their descriptions and values

Parameters	Description	Values	Source
$\Lambda$	Recruitment rate	$\frac{10^6}{365}$	[33]
$\beta_H, \beta_1$	Rate of ingesting of EDC	0.2	Assumed
$\mu$	Natural death rate	$\frac{1}{365 * 65}$	[33]
$\alpha_1$	Rate of healthy persons to become pre-diabetic	0.1	[34]
$\alpha_2$	Rate at which a pre-diabetic person becomes healthy	0.02	[34]
$\alpha_3$	Rate at which a exposed person becomes healthy	0.05	Assumed
$\epsilon$	Probability of people to have complication	0.3	Assumed
$\gamma_1$	Probability of a pre-diabetic to become diabetic	0.1	[35]
$\gamma_2$	Probability of a diabetic developing a complications	0.1	[35]
$\gamma_3$	Probability of a pre-diabetic developing a complication	0.1	[35]
$\theta_1$	Probability of a Exposed to become diabetic	0.05	Assumed
$\theta_2$	Probability of a Exposed developing a complication	0.033	Assumed
$b$	Rate at which concentration of EDC increase	0.3	Assumed
$r$	Rate at which concentration of EDC decrease by control	0.1	Assumed
$\delta$	Disease induced death rate	$\frac{1}{365 * 40}$	[33]

By taking into account the model parameters description and flow diagram given in [Figure 1](#), the system of equations is provided as follows:

$$\begin{aligned}
 \frac{dP}{dt} &= \Lambda - (\alpha_1 + \beta_H \frac{F}{F+K} + \mu)P + \alpha_2 S + \alpha_3 E, \\
 \frac{dS}{dt} &= \alpha_1 P - (\gamma_1 + \gamma_3 + \alpha_2 + \beta_1 \frac{F}{F+K} + \mu)S, \\
 \frac{dD}{dt} &= \left( \gamma_1 + (1 - \epsilon)\beta_1 \frac{F}{F+K} \right) S - (\gamma_2 + \mu)D + \theta_1 E, \\
 \frac{dC}{dt} &= \left( \gamma_3 + \epsilon\beta_1 \frac{F}{F+K} \right) S + \gamma_2 D + \theta_2 E - (\mu + \delta)C, \\
 \frac{dE}{dt} &= \beta_H \frac{F}{F+K} P - (\theta_1 + \theta_2 + \alpha_3 + \mu)E, \\
 \frac{dF}{dt} &= bF \left( \left(1 - \frac{F}{K}\right) - rF \right),
 \end{aligned}
 \tag{1}$$

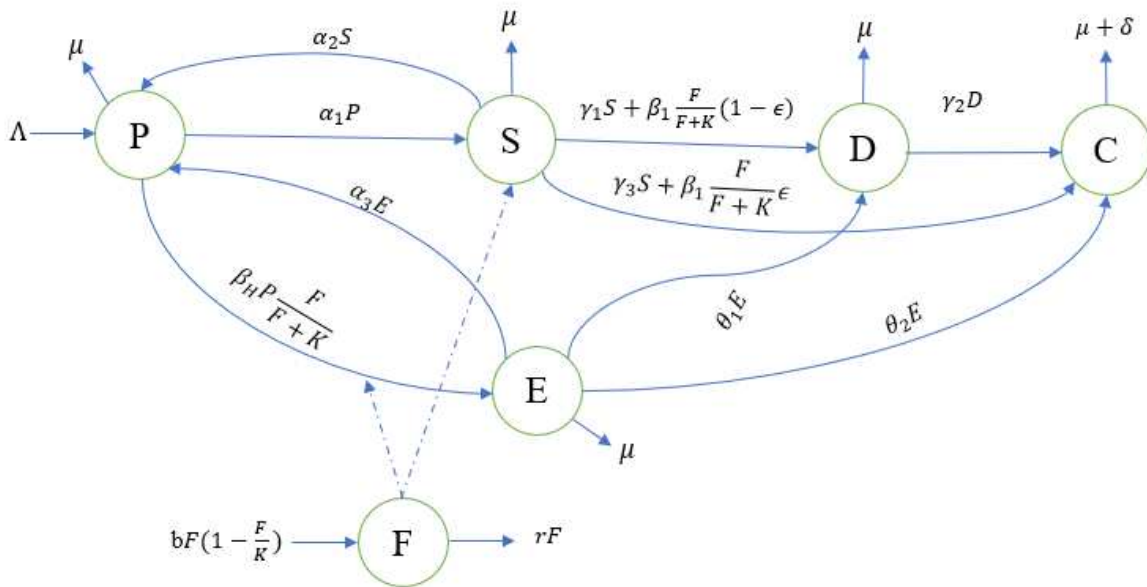


Figure 1. A flow diagram for diabetes model with the effects of EDC

with initial conditions

$$P(0) \geq 0, S(0) \geq 0, D(0) \geq 0, C(0) \geq 0, E(0) \geq 0, \text{ and } F(0) \geq 0. \tag{2}$$

For the diabetes model (1), it is needed to show that its state variables are non-negative for all time  $t > 0$  and that the feasible region is bounded is studied in the following theorems:

**Theorem 1** Suppose that the initial condition (2) of system (1) be non-negative, then the solution  $P(t) \geq 0, S(t) \geq 0, D(t) \geq 0, C(t) \geq 0, E(t) \geq 0$  and  $F(t) \geq 0$  are also non-negative  $\forall t > 0$ .

**Proof** Now, let us take the first equation of system (1) as follows

$$\begin{aligned} \frac{dP}{dt} &= \Lambda - \left(\alpha_1 + \beta_H \frac{F}{F+K} + \mu\right)P + \alpha_2 S + \alpha_3 E \\ &\geq -\left(\alpha_1 + \beta_H \frac{F}{F+K} + \mu\right)P, \end{aligned}$$

$$\frac{dP}{dt} + \left\{\alpha_1 + \beta_H \frac{F}{F+K} + \mu\right\}P \geq 0.$$

Then we obtain,  $\frac{d}{dt}P(t) \exp\left(\int_0^t \left(\alpha_1 + \beta_H \frac{F}{F+K} + \mu\right)ds\right) \geq 0$ . Integrating from 0 to  $t$ ,

$$\int_0^t \frac{d}{dt} \left( P(s) \exp \left( \int_0^s \left( \alpha_1 + \beta_H \frac{F}{F+K} + \mu \right) ds \right) \right) ds \geq 0,$$

then

$$P(t) \geq P(0) \exp \left( \int_0^t \left( \alpha_1 + \beta_H \frac{F}{F+K} + \mu \right) ds \right) \implies P(t) \geq 0.$$

This shows that  $P(t) \geq 0$  for all  $t > 0$ . Similarly, we can show for all other classes. ■

**Theorem 2** Let

$$\omega_H = \left\{ (P, S, D, C, E) \in \mathbb{R}_+^5, 0 \leq P + S + D + C + E \leq \frac{\Lambda}{\mu} \right\}, \tag{3}$$

and

$$\omega_F = \left\{ F \in \mathbb{R}_+, 0 \leq F \leq K\left(1 - \frac{r}{b}\right) \right\}. \tag{4}$$

Define  $\omega = \omega_H \times \omega_F$ . If  $N(0) \leq \frac{\Lambda}{\mu}$  and  $F(0) \leq K\left(1 - \frac{r}{b}\right)$ , then the region  $\omega$  is positively invariant under system (1) with initial condition (2) in  $\mathbb{R}_+^6$ .

**Proof** Let us consider system (1), we have human population  $N = P + S + D + C + E$  and Food compartment  $F$  exposed with concentration of EDC. From adding first five equation of system (1), we have

$$\frac{dN}{dt} = \Lambda - \mu P - \mu S - \mu E - \mu D - \mu C - \delta C \leq \Lambda - \mu N,$$

which yields that

$$N(t) \leq \frac{\Lambda}{\mu} - N(0)e^{-\mu t},$$

where  $\Lambda$  be the recruitment rate and  $N(0)$  represents initial values of total population.

$$\limsup_{t \rightarrow \infty} N(t) = \frac{\Lambda}{\mu} = N_\infty.$$

Assuming  $0 \leq N(0) \leq N_\infty$ , we obtain that  $0 \leq N(t) \leq N_\infty$ , for all  $t > 0$ . For this reason, we define a separate feasible region  $\omega_H$  for the human population as in (3). For the food compartment, it follows that

$$\frac{dF}{dt} = bF \left( 1 - \frac{F}{K} \right) - rF.$$

Let

$$F_\infty = K\left(1 - \frac{r}{b}\right).$$

Note that  $F_\infty$  is the stable equilibrium point of the above differential equation. Assuming  $0 \leq F(0) \leq F_\infty$ . We obtain that  $0 \leq F(t) \leq F_\infty$ . Our compartment  $F$  doesn't exceed  $F_\infty$ . We get feasible region  $\omega_F$  for the Food compartment as in (3). Therefore,  $N(t)$  and  $F(t)$  are bounded for all  $t > 0$ , respectively. Hence every solution of system (1) with initial condition (2) in  $\omega$  are remains in  $\omega$ . ■

### 3 Optimal control problem

In this section, we used an optimal control approach to reduce the consumption of EDC-exposed food products by individuals at higher risk of T2D. In our model (1), we have included the following controls to reduce the impact of EDC among Healthy people as well as Diabetes people.

- $u_1$  be the percentage of healthy people prevented from pre-diabetes.
- $u_2$  be the people prevented from consumption of EDC.
- $u_3$  be a treatment for exposed.
- $u_4$  be the control implemented to decrease the level of EDC.

The optimal control problem for the system (1) is given in the following system of equation.

$$\begin{aligned}
 \frac{dP}{dt} &= \Lambda - (\alpha_1(1 - u_1) + \beta_P(1 - u_2)\frac{F}{F + K} + \mu)H + \alpha_2S + (\alpha_3 + pu_3)E, \\
 \frac{dS}{dt} &= \alpha_1(1 - u_1)H - (\gamma_1 + \gamma_3 + \alpha_2 + \beta_1(1 - u_2)\frac{F}{F + K} + \mu)S, \\
 \frac{dD}{dt} &= (\gamma_1 + (1 - \epsilon)\beta_1(1 - u_2)\frac{F}{F + K})S - (\gamma_2 + \mu)D + \theta_1E, \\
 \frac{dC}{dt} &= (\gamma_3 + \epsilon\beta_1(1 - u_2)\frac{F}{F + K})S + \theta_2E + \gamma_2D - (\mu + \delta)C, \\
 \frac{dE}{dt} &= \beta_P(1 - u_2)\frac{F}{F + K}P - (\theta_1 + \theta_2 + \alpha_3 + \mu + pu_3)E, \\
 \frac{dF}{dt} &= bF(1 - \frac{F}{K}) - u_4F.
 \end{aligned}
 \tag{5}$$

The problem is to minimize the objective functional  $J$  defined as.

$$\begin{aligned}
 J(u_1(t), u_2(t), u_3(t), u_4(t)) = \int_0^T &\left( A_1S + A_2C + A_3D + A_4E + A_5F + \frac{B_1u_1^2}{2} \right. \\
 &\left. + \frac{B_2u_2^2}{2} + \frac{B_3u_3^2}{2} + \frac{B_4u_4^2}{2} \right) dt,
 \end{aligned}
 \tag{6}$$

where  $A_i, B_i, i = 1$  to  $4$  are cost coefficients. They are selected to weigh the relative importance of  $u_i, i = 1$  to  $4$  at time  $t, T$  is the final time. In other words, we seek the optimal controls  $u_i^*, i = 1$  to  $4$  such that

$$J(u_1^*, u_2^*, u_3^*, u_4^*) = \min_{u_i \in U} J(u_1, u_2, u_3, u_4),
 \tag{7}$$

where  $U$  is the set of admissible controls defined by

$$\begin{aligned}
 U = \{ (u_i) / 0 \leq u_{1_{\min}} \leq u_1(t) \leq u_{1_{\max}} \leq 1, 0 \leq u_{2_{\min}} \leq u_2(t) \leq u_{2_{\max}} \leq 1, \\
 0 \leq u_{3_{\min}} \leq u_3(t) \leq u_{3_{\max}} \leq 1, 0 \leq u_{4_{\min}} \leq u_4(t) \leq u_{4_{\max}} \leq 1, t \in [0, T] \}.
 \end{aligned}$$

$$\begin{aligned}
 H(t) = (A_1S + A_2C + A_3D + A_4E + A_5F) + \left( \frac{B_1u_1^2}{2} + \frac{B_2u_2^2}{2} + \frac{B_3u_3^2}{2} + \frac{B_4u_4^2}{2} \right) \\
 + \sum_1^{11} \lambda_i f_i(P, S, D, C, E, F),
 \end{aligned}
 \tag{8}$$

where  $f_i$  is the R.H.S of differential equation (5) of  $i^{th}$  state variable.

### Existence of the optimal control

Using the result of Fleming and Rishel [36], we can prove the existence of optimal control. It follows that the set of controls and corresponding state variables is non-empty. Also, the control space  $U$  is convex and closed by definition. All the R.H.S of equation (5) is continuous, bounded above by a sum of bounded control and state and can be written as a linear function of  $u_i$  with a coefficient depending on the time and state. The integrand in the objective function is convex on  $U$ .

$$L(y, u_i, t) \geq -\delta_1 + \delta_2|u_1|^{\delta} + \delta_3|u_2|^{\delta} + \delta_4|u_3|^{\delta} + \delta_5|u_4|^{\delta}.$$

Thus, the results satisfy all the conditions mentioned in Fleming and Rishel’s work [36]. Therefore, we establish the following theorem:

**Theorem 3** Consider the control problem with the system (5). There exists an optimal control  $u_i, i = 1$  to  $4 \in U^4$  such that

$$J(u_1^*, u_2^*, u_3^*, u_4^*) = \min_{u_i \in U} J(u_1, u_2, u_3, u_4). \tag{9}$$

**Proof** The existence of the optimal control obtained using the result of Fleming and Rishel [36], checking the following steps:

- It follows that the controls and corresponding state variables are non-empty. We will use a simplified version of an existence result.
- $J(u_1(t), u_2(t), u_3(t), u_4(t))$  is convex in  $U$ .
- The control space  $U = (u_i)/u_i, i = 1$  to  $4$  is measurable.  $0 \leq u_{1_{\min}} \leq u_1(t) \leq u_{1_{\max}} \leq 1, 0 \leq u_{2_{\min}} \leq u_2(t) \leq u_{2_{\max}} \leq 1, 0 \leq u_{3_{\min}} \leq u_3(t) \leq u_{3_{\max}} \leq 1, 0 \leq u_{4_{\min}} \leq u_4(t) \leq u_{4_{\max}} \leq 1, t \in [0, T]$  is convex and closed by definition.
- All the R.H.S of equation (5) is continuous, bounded above by a sum of bounded control and state and can be written as a linear function of  $u_i$  with a coefficient depending on the time and state.
- The integrand in the objective functional  $\left( \frac{B_1 u_1^2}{2} + \frac{B_2 u_2^2}{2} + \frac{B_3 u_3^2}{2} + \frac{B_4 u_4^2}{2} \right)$  is clearly convex on  $U$ .
- Since the solution of system (5) is bounded, the system satisfies the Lipschitz property with respect to the variables  $P, S, D, C, E$  and  $F$ . Therefore, there exists an optimal control.

Hence, from Fleming and Rishel [36], we conclude that there exists an optimal control. ■

### Characterization of the optimal control

To derive the necessary conditions for the optimal control, we apply Pontryagin’s maximum principle to the Hamiltonian  $H$  given by equation (8) at time  $t$ .

**Theorem 4** Given the optimal control  $(u_1, u_2, u_3, u_4)$  and the solution  $P^*, S^*, D^*, C^*, E^*, F^*$  of the corresponding state system (5), there exists adjoint variable  $\lambda_i, for i = 1$  to  $6$  satisfying

$$-\frac{d\lambda_p}{dt} = \frac{\partial H}{\partial P}, -\frac{d\lambda_s}{dt} = \frac{\partial H}{\partial S}, -\frac{d\lambda_d}{dt} = \frac{\partial H}{\partial D}, -\frac{d\lambda_c}{dt} = \frac{\partial H}{\partial C}, -\frac{d\lambda_e}{dt} = \frac{\partial H}{\partial E}, -\frac{d\lambda_f}{dt} = \frac{\partial H}{\partial F},$$

with the transversality conditions at time  $T, \lambda_j(T) = 0, j = p, s, d, c, e, f$ . Furthermore, for  $t \in [0, T]$ , the

optimal controls  $u_1^*, u_2^*, u_3^*, u_4^*$  are given by

$$\begin{aligned}
 u_1^*(t) &= \max \left\{ 0, \min \left\{ 1 - \varepsilon, \frac{(\lambda_2 - \lambda_1)\alpha_1 P}{B_1} \right\} \right\}, \\
 u_2^*(t) &= \max \left\{ 0, \min \left\{ 1 - \varepsilon, \frac{(\lambda_1 - \lambda_5)\beta_P P}{B_2} \frac{F}{F + K} + \frac{(\lambda_3 - \lambda_2)\beta_1 S}{B_2} \frac{F}{F + K} + \frac{(\lambda_4 - \lambda_3)\varepsilon\beta_1 S}{B_2} \frac{F}{F + K} \right\} \right\}, \\
 u_3^*(t) &= \max \left\{ 0, \min \left\{ 1 - \varepsilon, \frac{(\lambda_5 - \lambda_1)p_1 E}{B_3} \right\} \right\}, \\
 u_4^*(t) &= \max \left\{ 0, \min \left\{ 1 - \varepsilon, \frac{\lambda_6 F}{B_4} \right\} \right\}.
 \end{aligned}$$

**Proof** For  $t \in [0, T]$ , the adjoint equation and transversality conditions obtained by using Pontryagin’s principle such that

$$\begin{aligned}
 \lambda_1' &= \lambda_1 \left( \alpha_1(1 - u_1) - \beta_P(1 - u_2) \frac{F}{F + K} + \mu \right) - \lambda_2 \alpha_1(1 - u_1) - \lambda_5(1 - u_2) \beta_P \frac{F}{F + K}, \\
 \lambda_2' &= -A_1 - \lambda_1 \alpha_2 + \lambda_2(\gamma_1 + \gamma_3 + \alpha_2 + \beta_1(1 - u_2) \frac{F}{F + K} + \mu) - \lambda_3(\beta_1(1 - \varepsilon)(1 - u_2) \frac{F}{F + K} + \gamma_1) \\
 &\quad - \lambda_4(\varepsilon\beta_1(1 - u_2) \frac{F}{F + K} + \gamma_3), \\
 \lambda_3' &= -A_2 + \lambda_3(\gamma_2 + \mu) - \lambda_4 \gamma_2, \\
 \lambda_4' &= -A_3 + \lambda_4(\mu + \delta), \\
 \lambda_5' &= -A_4 - \lambda_1(\alpha_3 + p_1 u_3) - \lambda_3 \theta_1 - \lambda_4 \theta_2 + \lambda_5(\theta_1 + \theta_2 + \alpha_3 + p_1 u_3 + \mu), \\
 \lambda_6' &= -A_5 + \beta_P P(\lambda_1 - \lambda_5)(1 - u_2) \frac{K}{(K + F)^2} + \beta_1 S(\lambda_2 - \lambda_3(1 - \varepsilon) - \lambda_4 \varepsilon)(1 - u_2) \frac{K}{(K + F)^2} \\
 &\quad - \lambda_6 \left( b(1 - \frac{F}{K}) - b \frac{F}{K} - u_4 \right),
 \end{aligned}$$

with transversality conditions  $\lambda_i = 0, i = 1$  to 11. For  $t \in [0, T]$ , the optimal controls  $u_1^*, u_2^*, u_3^*, u_4^*$  can be solved by the optimality conditions  $\frac{\partial H}{\partial u_i}$ .

$$\begin{aligned}
 u_1^*(t) &= \frac{(\lambda_2 - \lambda_1)\alpha_1 P}{B_1}, \\
 u_2^*(t) &= \frac{(\lambda_1 - \lambda_5)\beta_P P}{B_2} \frac{F}{F + K} + \frac{(\lambda_3 - \lambda_2)\beta_1 S}{B_2} \frac{F}{F + K} + \frac{(\lambda_4 - \lambda_3)\varepsilon\beta_1 S}{B_2} \frac{F}{F + K}, \\
 u_3^*(t) &= \frac{(\lambda_5 - \lambda_1)p_1 E}{B_3}, \\
 u_4^*(t) &= \frac{\lambda_6 F}{B_4}.
 \end{aligned}$$

By the bounds in  $U$  of the controls, it is easy to obtain the optimal controls. ■

#### 4 Numerical simulation and discussion

Simulation is required to understand the reasoning behind theoretical findings. It changes according to the values assigned to the parameters. We stimulate the diabetes model using Euler’s method. The optimal control problem is solved using the Forward-backward sweep method.

Initial and final conditions exist for state and adjacent systems, respectively. The weight constants and initial conditions are  $A_1 = A_2 = A_3 = A_4 = A_5 = 1$ ,  $B_1 = B_2 = B_3 = B_4 = 2000$ .

The parameter values described in Table 2 are applied to simulate the diabetes model using the Matlab program. We have used diabetes data for India from 1980 to 2015. The diabetes dataset is available on the NCD-RisC website (<https://ncdrisc.org/index.html>). Then, using manual calibration, we fitted each parameter to get the best fit to our proposed model (1). Figure 2 shows that our model fits almost to the dataset. The range of parameter values used in calibration are from the literature. The parameters  $b$  and  $r$  are essential for regulating the EDC density of the food.

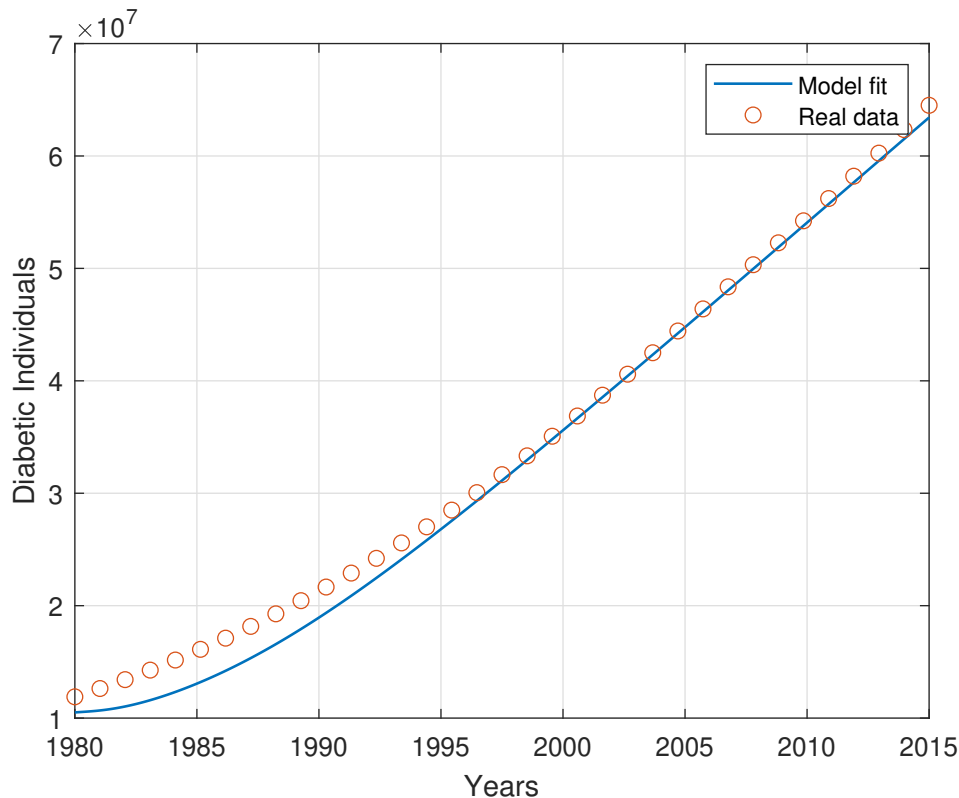
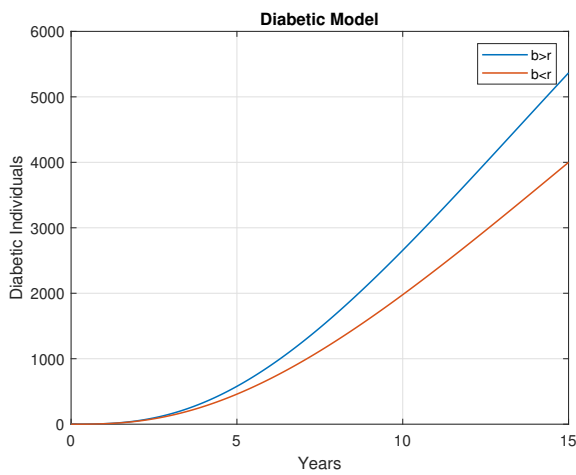


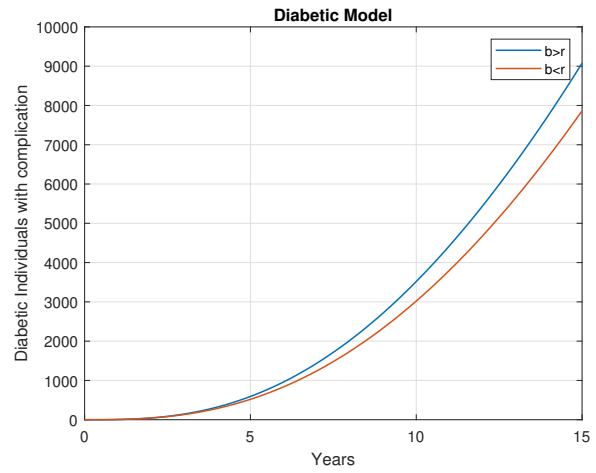
**Figure 2.** The diabetes population data from 1980 to 2015 in India and best curve fit of the proposed model

As a basic guideline,  $r$  must be higher than  $b$ . It means that  $r$  is the controlling parameter of EDC in any product. Parameter  $b$  is higher than parameter  $r$ . It represents that higher concentrations of EDC in food may affect humans. Every population with  $b < c$  and  $b > c$  is depicted in Figure 3.

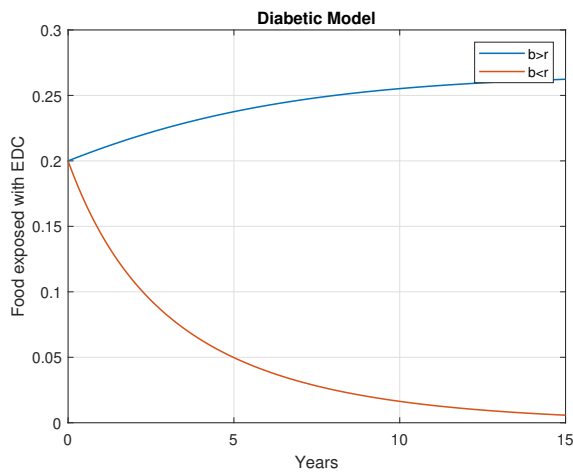
It noted that whenever the control parameter  $r$  fails to control the level of Endocrine, the diabetes prevalence increases. Figure 4 depicts each compartment with and without control. Diabetes is largely preventable by taking the proposed control variable. Figure 5 illustrates the control profile with  $B_4 = 20$  and  $B_4 = 2000$ . The graph indicates that if control costs are low, people can afford them for a long time. If the control cost is reasonable, then more individuals will be able to get better. According to the findings in Figure 6, the concentration of EDC in food products is reduced more effectively over time if the cost of control is affordable and the exposed population seems minimized. The graph indicates that lowering the concentration of EDC impacts T2D, although other regulations are applied to reduce diabetes incidence. The prevalence of diabetes has decreased after implementing the necessary controls. The graph clearly shows that the lower the control costs, the higher the likelihood of recovery.



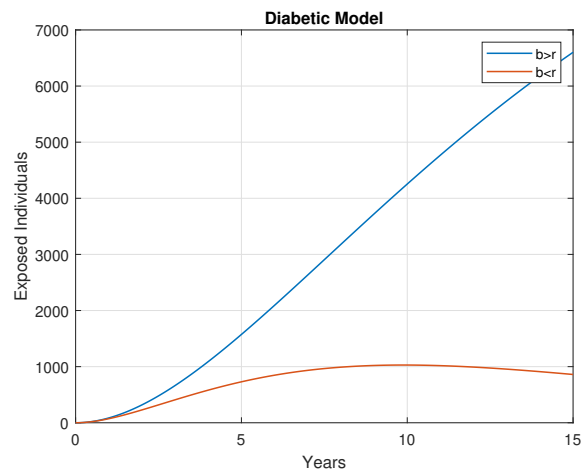
(a) Profile of diabetes population for  $b > r$  and  $b < r$



(b) Profile of diabetes population with complication for  $b > r$  and  $b < r$

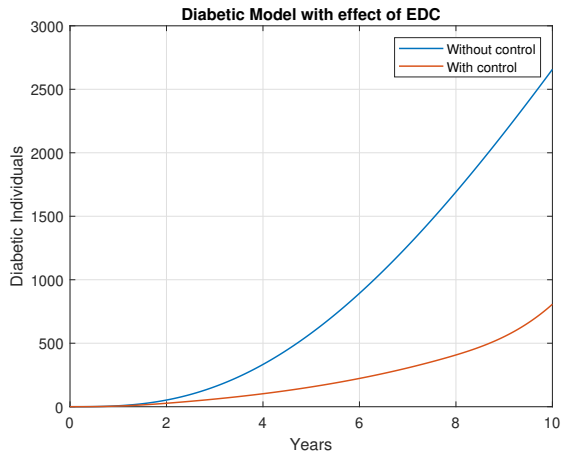


(c) Profile of food exposed with EDC compartment for  $b > r$  and  $b < r$

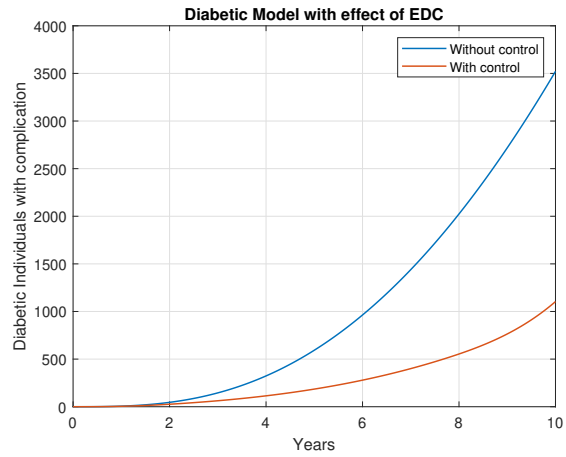


(d) Profile of exposed population with EDC for  $b > r$  and  $b < r$

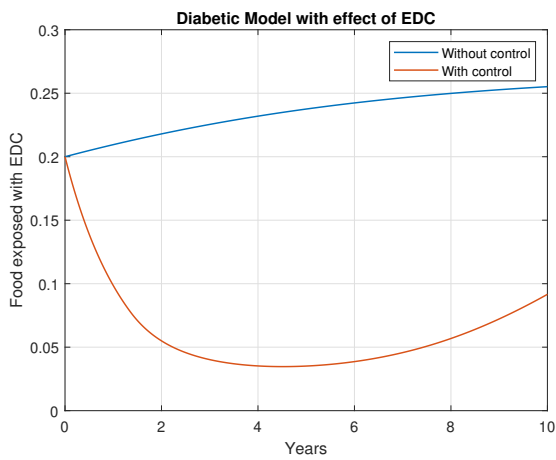
**Figure 3.** The dynamic of variables  $D, C, E, F$  for  $b > r$  and  $b < r$



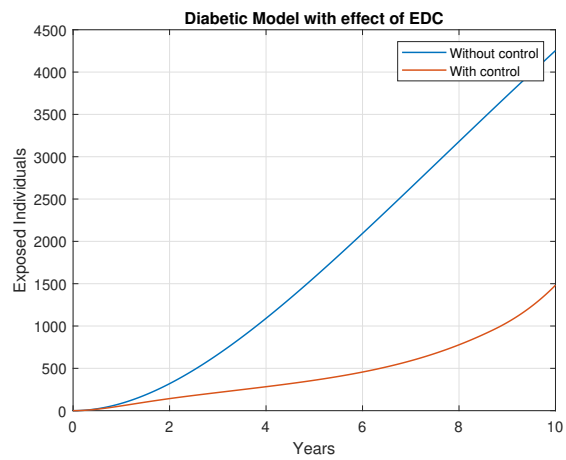
(a) Profile of diabetes population without control and with control



(b) Profile of diabetes population with complication without control and with control

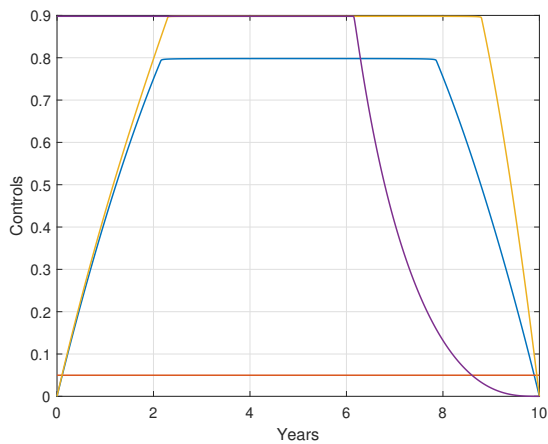


(c) Profile of food exposed with EDC compartment without control and with control

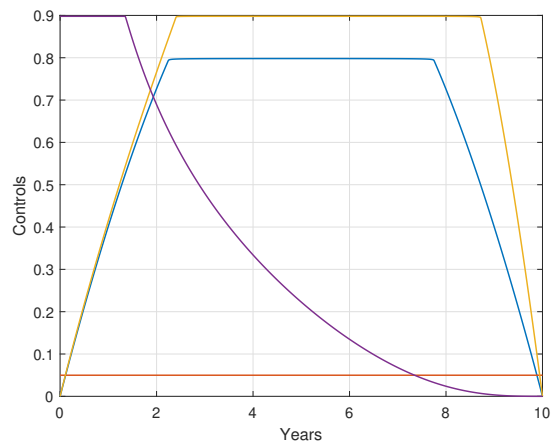


(d) Profile of exposed population with EDC without control and with control

**Figure 4.** The dynamic of variables with and without control

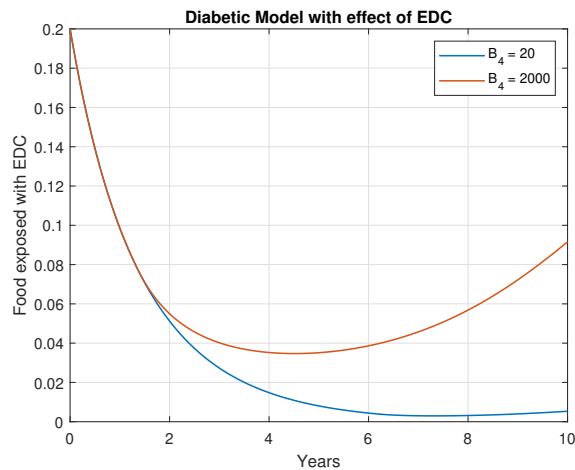
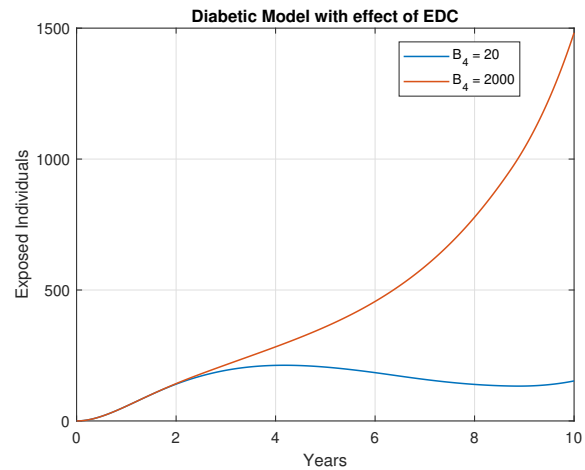
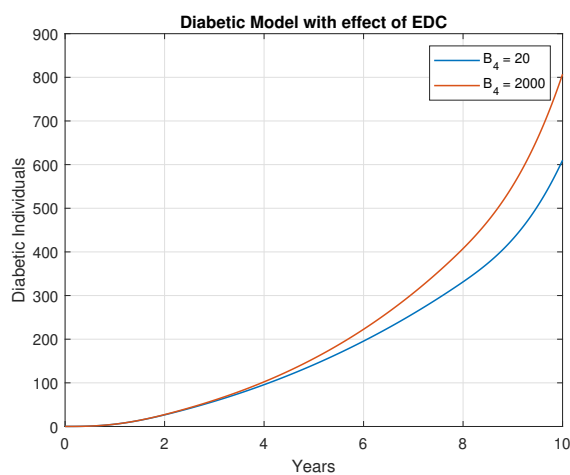
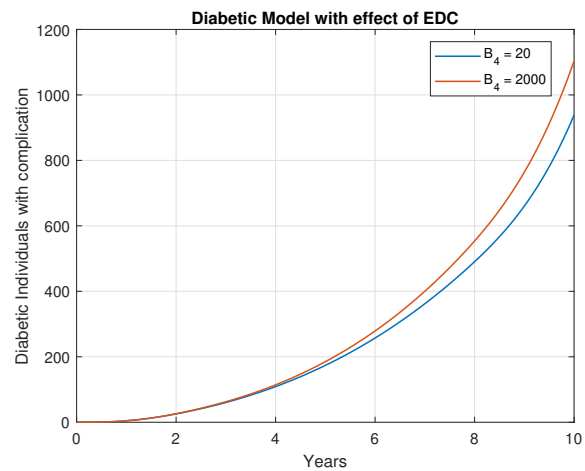


(a) Profile of control with  $B_4 = 50$



(b) Profile of control with  $B_4 = 5000$

**Figure 5.** The control profile with different values of cost of controls

(a) Profile of food exposed with EDC with  $B_4 = 20$  and 2000(b) Profile of exposed with EDC with  $B_4 = 20$  and 2000(c) Profile of diabetes population with  $B_4 = 20$  and 2000(d) Profile of diabetes population with complication with  $B_4 = 20$  and 2000**Figure 6.** The profile of E, D, C and F with different values of the cost of controls

## 5 Conclusion

In this paper, we have developed a mathematical model of the diabetic population with the effect of EDC. This proposed model offers a different approach to understanding the prevalence of diabetes, particularly when the daily consumption of food is exposed to some harmful chemicals that lead to health problems. A suitable control strategy discussed includes intervention for exposed people, diabetes prevention, control of EDC concentration on daily consumption, and prevention of consuming EDC. We have found the optimal control strategies that are more effective in controlling the prevalence of diabetes. The findings demonstrate the efficacy of the proposed control strategies. The results show that less EDC exposure is better for diabetes control. In the future, one can try to incorporate other sources of T2D with fractional-order differential equations and cost-effective analysis to improve the effective way of controlling diabetes. Also, studying the nature of equilibrium and stability analysis can be considered.

## Declarations

### List of abbreviations

Not applicable.

### Ethical approval

The authors state that this research complies with ethical standards. This research does not involve either human participants or animals.

### Consent for publication

Not applicable.

### Conflicts of interest

The authors confirm that there is no competing interest in this study.

### Data availability statement

Data availability is not applicable to this article as no new data were created or analyzed in this study.

### Funding

Not applicable.

### Author's contributions

L.P.: Conceptualization, Methodology, Software, Validation, Data Curation, Writing - Original Draft. M.C.: Writing - Review & Editing, Supervision. All authors have read and agreed to the published version of the manuscript.

### Acknowledgements

The authors would like to thank the anonymous reviewers for taking the time and effort necessary to review the manuscript. They sincerely appreciate all valuable comments and suggestions, which helped them to improve the quality of the manuscript.

### References

- [1] Wu, H., Eggleston, K.N., Zhong, J., Hu, R., Wang, C., Xie, K. et al. How do type 2 diabetes mellitus (T2DM)-related complications and socioeconomic factors impact direct medical costs? A cross-sectional study in rural Southeast China. *BMJ Open*, 8(11), e020647, (2018). [[CrossRef](#)]
- [2] World Health Organization, Health Topics, Diabetes. <https://www.who.int/health-topics/diabetes>, [Accessed: 15.10.2023].
- [3] The American Diabetes Association®(ADA). <https://www.diabetes.org/diabetes>, [Accessed: 15.10.2023].
- [4] Scheen, A. Pathophysiology of type 2 diabetes. *Acta Clinica Belgica*, 58(6), 335-341, (2003). [[CrossRef](#)]
- [5] International diabetes federation, IDF Diabetes Atlas 2021. <https://diabetesatlas.org/>, [Accessed: 15.10.2023].

- [6] Institute for Public Health. "National Health Morbidity Survey 2015 (NHMS 2015). Vol. II: Non-Communicable Diseases, Risk Factors & Other Health Problems." Minist. Health Malays. 2: 185-186 (2015). Retrieved from <https://www.moh.gov.my/moh/resources/nhmsreport2015vol2.pdf>
- [7] Malaysian Ministry of Health (MMH), 2016. National Strategic Plan for Non-Communicable Disease (NSP- NCD) 2016-2025. Retrieved from [https://www.iccp-portal.org/system/files/plans/MYS\\_B3\\_NSP%20NCD%202016-2025%2C%20FINAL.pdf](https://www.iccp-portal.org/system/files/plans/MYS_B3_NSP%20NCD%202016-2025%2C%20FINAL.pdf)
- [8] Dal Canto, E., Ceriello, A., Rydén, L., Ferrini, M., Hansen, T.B., Schnell, O. et al. Diabetes as a cardiovascular risk factor: An overview of global trends of macro and micro vascular complications. *European Journal of Preventive Cardiology*, 26(2<sub>s</sub>uppl), 25-32, (2019). [CrossRef]
- [9] Forbes, J.M. and Cooper, M.E. Mechanisms of diabetic complications. *Physiological Reviews*, 93(1), 137-188 (2013). [CrossRef]
- [10] Alonso-Magdalena, P., Quesada, I. and Nadal, A. Endocrine disruptors in the etiology of type 2 diabetes mellitus. *Nature Reviews Endocrinology*, 7, 346-353, (2011). [CrossRef]
- [11] Zoeller, R.T., Brown, T.R., Doan, L.L., Gore, A.C., Skakkebaek, N.E., Soto, A.M. et al. Endocrine-disrupting chemicals and public health protection: a statement of principles from The Endocrine Society. *Endocrinology*, 153(9), 4097-4110, (2012). [CrossRef]
- [12] Kunysz, M., Mora-Janiszewska, O. and Darmochwał-Kolarz, D. Epigenetic modifications associated with exposure to endocrine disrupting chemicals in patients with gestational diabetes mellitus. *International Journal of Molecular Sciences*, 22(9), 4693, (2021). [CrossRef]
- [13] Street, M.E., Angelini, S., Bernasconi, S., Burgio, E., Cassio, A., Catellani, C. et al. Current knowledge on endocrine disrupting chemicals (EDCs) from animal biology to humans, from pregnancy to adulthood: highlights from a national Italian meeting. *International Journal of Molecular Sciences*, 19(6), 1647, (2018). [CrossRef]
- [14] Sargis, R.M. and Simmons, R.A. Environmental neglect: endocrine disruptors as underappreciated but potentially modifiable diabetes risk factors. *Diabetologia*, 62, 1811-1822, (2019). [CrossRef]
- [15] Beszterda, M. and Frański, R. Endocrine disruptor compounds in environment: As a danger for children health. *Pediatric Endocrinology Diabetes and Metabolism*, 24(2), 88-95, (2018). [CrossRef]
- [16] Selevan, S.G., Kimmel, C.A. and Mendola, P. Identifying critical windows of exposure for children's health. *Environmental Health Perspectives*, 108(suppl 3), 451-455, (2000). [CrossRef]
- [17] Sun, Q., Zong, G., Valvi, D., Nielsen, F., Coull, B. and Grandjean, P. Plasma concentrations of perfluoroalkyl substances and risk of type 2 diabetes: A prospective investigation among US women. *Environmental Health Perspectives*, 126(3), 037001, (2018). [CrossRef]
- [18] Lind, P.M. and Lind, L. Endocrine-disrupting chemicals and risk of diabetes: an evidence-based review. *Diabetologia*, 61, 1495-1502, (2018). [CrossRef]
- [19] Boutayeb, A., Twizell, E.H., Achouayb, K. and Chetouani, A. A mathematical model for the burden of diabetes and its complications. *BioMedical Engineering OnLine*, 3, 20, (2004). [CrossRef]
- [20] Boutayeb, A., Chetouani, A., Achouyab, A. and Twizell, E.H. A non-linear population model of diabetes mellitus. *Journal of Applied Mathematics and Computing*, 21, 127-139, (2006). [CrossRef]
- [21] Derouich, M., Boutayeb, A., Boutayeb, W. and Lamlili, M. Optimal control approach to the

- dynamics of a population of diabetics. *Applied mathematical sciences*, 8(56), 2773-2782, (2104). [[CrossRef](#)]
- [22] Widyaningsih, P., Affan, R.C. and Saputro, D.R.S. A mathematical model for the epidemiology of diabetes mellitus with lifestyle and genetic factors. In Proceedings, *Journal of Physics: Conference Series* (Vol. 1028), pp. 012110, Makassar, Indonesia, (2018, October). [[CrossRef](#)]
- [23] Bassey, B.E. Optimal control model for dual treatment of delayed type-II diabetes infection in human population. *Open Science Journal of Mathematics and Application*, 7(1), 34-49, (2019).
- [24] Jajarmi, A., Ghanbari, B. and Baleanu, D. A new and efficient numerical method for the fractional modeling and optimal control of diabetes and tuberculosis co-existence. *Chaos: An Interdisciplinary Journal of Nonlinear Science*, 29, 093111, (2019). [[CrossRef](#)]
- [25] Akinsola, V.O. and Oluyo, T.O. Mathematical analysis with numerical solutions of the mathematical model for the complications and control of diabetes mellitus. *Journal of Statistics and Management systems*, 22(5), 845-869, (2019). [[CrossRef](#)]
- [26] Ndi, M.Z., Berkanis, F.R., Tambaru, D., Lobo, M., Ariyanto and Djahi, B.S. Optimal control strategy for the effects of hard water consumption on kidney-related diseases. *BMC Research Notes*, 13, 201, (2020). [[CrossRef](#)]
- [27] Anusha, S. and Athithan, S. Mathematical modelling co-existence of diabetes and COVID-19: Deterministic and stochastic approach. *Research Square*, (2021). [[CrossRef](#)]
- [28] Özköse, F. and Yavuz, M. Investigation of interactions between COVID-19 and diabetes with hereditary traits using real data: A case study in Turkey. *Computers in biology and medicine*, 141, 105044, (2022). [[CrossRef](#)]
- [29] Agwu, C.O., Omame, A. and Inyama, S.C. Analysis of mathematical model of diabetes and Tuberculosis co-infection. *International Journal of Applied and Computational Mathematics*, 9, 36, (2023). [[CrossRef](#)]
- [30] Mollah, S. and Biswas, S. Optimal control for the complication of Type 2 diabetes: the role of awareness programs by media and treatment. *International Journal of Dynamics and Control*, 11, 877-891, (2023). [[CrossRef](#)]
- [31] Singh, T. and Adlakha, N. Numerical investigations and simulation of calcium distribution in the alpha-cell. *Bulletin of Biomathematics*, 1(1), 40-57, (2023). [[CrossRef](#)]
- [32] Balakrishnan, G.P., Chinnathambi, R. and Rihan, F.A. A fractional-order control model for diabetes with restraining and time-delay. *Journal of Applied Mathematics and Computing*, 69, 3403-3420, (2023). [[CrossRef](#)]
- [33] Nasir, H. Stability analysis and optimal control of a five-state diabetic population model. *Journal of Statistics and Management Systems*, 25(1), 245-267, (2022). [[CrossRef](#)]
- [34] Boutayeb, W., Lamlili, M.E.N., Boutayeb, A. and Derouich, M. The dynamics of a population of healthy people, pre-diabetics and diabetics with and without complications with optimal control. In Proceedings of the *Mediterranean Conference on Information & Communication Technologies: MedCT 2015*, (Vol. 1), pp. 463-471, Springer International Publishing, (2016, April). [[CrossRef](#)]
- [35] Kouidere, A., Youssoufi, L.E., Ferjouchia, H., Balatif, O. and Rachik, M. Optimal control of mathematical modeling of the spread of the COVID-19 pandemic with highlighting the negative impact of quarantine on diabetics people with cost-effectiveness. *Chaos, Solitons & Fractals*, 145, 110777, (2021). [[CrossRef](#)]
- [36] Fleming, W.H. and Rishel, R.W. *Deterministic and Stochastic Optimal Control* (Vol. 1). Springer-

Verlag: New York, (2012). [[CrossRef](#)]

Mathematical Modelling and Numerical Simulation with Applications (MMNSA)  
(<https://dergipark.org.tr/en/pub/mmnsa>)



**Copyright:** © 2023 by the authors. This work is licensed under a Creative Commons Attribution 4.0 (CC BY) International License. The authors retain ownership of the copyright for their article, but they allow anyone to download, reuse, reprint, modify, distribute, and/or copy articles in MMNSA, so long as the original authors and source are credited. To see the complete license contents, please visit (<http://creativecommons.org/licenses/by/4.0/>).

**How to cite this article:** Logaprakash, P. & Monica, C. (2023). Optimal control of diabetes model with the impact of endocrine-disrupting chemical: an emerging increased diabetes risk factor. *Mathematical Modelling and Numerical Simulation with Applications*, 3(4), 318-334. <https://doi.org/10.53391/mmnsa.1397575>



RESEARCH PAPER

## Examination of Sturm-Liouville problem with proportional derivative in control theory

Bahar Acay Öztürk <sup>1,\*</sup> ‡

<sup>1</sup>Department of Mathematics, Science Faculty, Firat University, 23119 Elazığ, Türkiye

\*Corresponding Author

‡bacay@firat.edu.tr (Bahar Acay Öztürk)

### Abstract

The current study is intended to provide a comprehensive application of Sturm-Liouville (S-L) problem by benefiting from the proportional derivative which is a crucial mathematical tool in control theory. This advantageous derivative, which has been presented to the literature with an interesting approach and a strong theoretical background, is defined by two tuning parameters in control theory and a proportional-derivative controller. Accordingly, this research is presented mainly to introduce the beneficial properties of the proportional derivative for analyzing the S-L initial value problem. In addition, we reach a novel representation of solutions for the S-L problem having an importing place in physics, supported by various graphs including different values of arbitrary order and eigenvalues under a specific potential function.

**Keywords:** Proportional-derivative controller; proportional integral; Sturm-Liouville problem; control theory; local derivative

**AMS 2020 Classification:** 00A69; 34B24; 00A05

### 1 Motivation

The advantage of using non-integer order integral-derivative operators lies in the fact that they express numerous real-world problems better than classical analysis tools. Fractional calculus provides a natural and intrinsic characterization of complex dynamical systems [1]. Also, the concepts in fractional calculus shed some new light on the solutions methods of differential equations, especially when the traditional tools are limited and insufficient. As a way of describing events in nature, this field whose history is as old as the classical differential has become quite interesting. Several fractional integral and derivative operators with various features have recently been introduced to the literature. While some researchers place a strong emphasis on the value of local derivatives, others highlight the benefits of non-local and singular kernel operators, while

others make the case that non-local and non-singular kernel operators are also beneficial. Although this situation might be confusing, the availability of several derivative-integral definitions has evolved into a fundamental motivational tool for researchers in order to produce superior findings for the problems at hand. The amount of complex systems that have been studied from the perspective of fractional dynamics has significantly increased over the past few decades. Fractional calculus can be used to assess a variety of phenomena, including transmission line theory, heat transfer, diffusion, electrochemistry, fractal processes, deoxyribonucleic acid decoding for prototype systems, financial considerations, earthquake events, global warming, and even musical rhythms. In addition, the existence of numerous complex systems, both natural and human-made, shows the abundance of phenomena that can be described and studied with the help of concepts in fractional calculus. The major goal is to establish the analysis framework of the problems under consideration by enlarging it in the perspective of fractional calculus. Although fractional calculus helps to expand the traditional definitions of derivative and integral, which then obviously lead to fractional-type models, neither the restrictions of their application nor the processes and tools for comprehending them are well-defined at the current stage of scientific evaluation. With Caputo's formulation of the fractional derivative, the scope of applications for non-integer order differential operators has been widened, and exciting results have been obtained by using them more frequently. The usage of fractional derivatives, which is expanding rapidly today, is especially useful for characterizing processes and describing physical phenomena. It has also taken on crucial tasks like eliminating the deficiencies in differential equations created with classical derivatives.

The usage of local derivative and integral definitions defined in the limit form has also grown in popularity, in addition to fractional derivatives, which are non-local because they are defined in the integral form. The "proportional derivative" definition, which was developed with the proportional derivative controller used in control theory, is one of them and may be the most advantageous one. This derivative is defined with the help of two tuning parameters in control theory and a proportional-derivative (PD) controller given by

$$\mathbf{u}(t) = k_p E(t) + k_d \dot{E}(t), \quad (1)$$

for the controller output  $\mathbf{u}$  at time  $t$  [2]. PD is a successful control method that is straightforward to comprehend. Here,  $k_p$  stands for the proportional gain,  $k_d$  for the derivative gain, and  $E$  for the error between the state and process variables. It is well-recognized that the proportional derivative controller effectively addresses problems with real-world control. Also, the proportional term offers a general control action that, via the gain coefficient, is proportionate to the error signal. The derivative term improves the transient response through high-frequency compensation. Intuitively, for these concepts, it makes sense to say that P depends on the current error and D is an estimate of future errors. Controlling the considered system by the weighted sum of these two actions results in the system reaching the desired state. Suppose that for  $\eta \in [0, 1]$ ,  $K_0, K_1 : [0, 1] \times \mathbb{R} \rightarrow [0, \infty)$  functions are continuous and satisfy the following conditions:

$$\lim_{\eta \rightarrow 0^+} K_1(\eta, t) = 1, \quad \lim_{\eta \rightarrow 0^+} K_0(\eta, t) = 0, \quad (2)$$

$$\lim_{\eta \rightarrow 1^-} K_1(\eta, t) = 0, \quad \lim_{\eta \rightarrow 1^-} K_0(\eta, t) = 1. \quad (3)$$

Then, for all  $t \in \mathbb{R}$ ,  $K_1(\eta, t) \neq 0$ ,  $\eta \in [0, 1)$  and  $K_0(\eta, t) \neq 0$ ,  $\eta \in (0, 1]$ , the proportional derivative

is defined as

$${}_p\mathbf{D}^\eta \omega(t) = K_1(\eta, t)\omega(t) + K_0(\eta, t)\omega'(t). \quad (4)$$

On the other hand, the proportional exponential function is given by

$$e_p(t, r) = e^{\int_r^t \frac{p(\tau) - K_1(\eta, \tau)}{K_0(\eta, \tau)} d\tau}, \quad e_0(t, r) = e^{-\int_r^t \frac{K_1(\eta, \tau)}{K_0(\eta, \tau)} d\tau}, \quad (5)$$

where  $\chi \in (0, 1]$ ,  $r, t \in \mathbb{R}$ ,  $r \leq t$ ,  $p : [r, t] \rightarrow \mathbb{R}$ , and  $k_0, k_1 : [0, 1] \times \mathbb{R} \rightarrow [0, \infty)$  are continuous functions. Also,  $p/k_0$  and  $k_1/k_0$  are Riemann integrable on  $[s, t]$ . Furthermore, for  $\eta \in (0, 1]$ , proportional integral on  $[a, b]$  is

$${}_p\mathbf{I}^\eta \omega(t) = \int_a^t \omega(r) e_0(t, r) d_\eta r = \int_a^t \frac{\omega(r) e_0(t, r)}{K_0(\eta, r)} dr, \quad d_\eta r = \frac{1}{K_0(\eta, r)} dr. \quad (6)$$

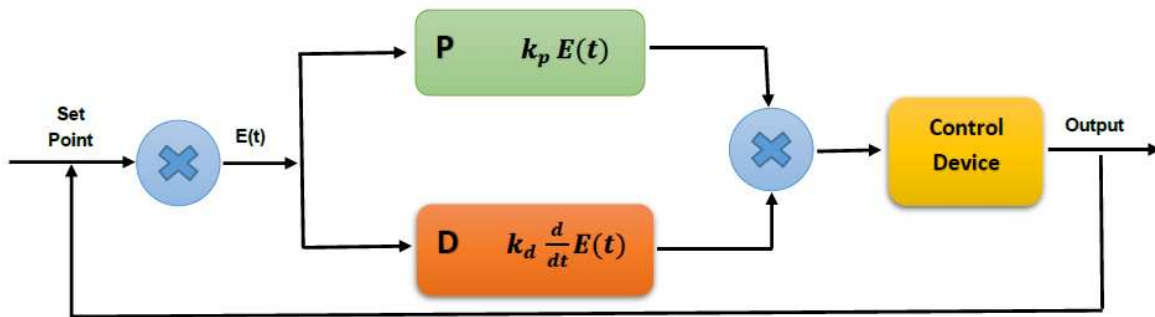


**Figure 1.** Block diagram of control system with proportional-derivative controller.

The derivative control method is known to change the controller output proportionally to the rate of the error signal change. Derivative control, on the other hand, observes how much the error has altered and tries to identify the current error. In order to minimize potential errors, it also generates control motion through using the rate of change. The integral technique is occasionally added in addition to the proportional method since the derivative method only affects the controller output when the error changes. In this context, it can be stated that the derivative control approaches can never be employed alone. The derivative value is determined by the rate of change of the error signal, that is, by the slope of the error signal. An ideal derivative technique is expected to respond with an infinite variation to the controller output and the derivative effect for quickly changing signals is constrained. In the derivative receiver circuit, the frequency of the signal applied at the input must be smaller than the cutoff frequency of the circuit, while the period of the signal applied at the input is desired to be close to the derivative time for the differentiation process to take place.

The difference signal between the set value and the measured value is subjected to a derivative operation in proportional-derivative control. After the error signal first passes through the proportional controller, the derivative signal, balancing voltage, and proportional signal are collected in the collector circuit. **Figure 1** depicts the control system diagram with a PD controller. As shown in the diagram, the PD controller continuously determines the error value  $E(t)$  [3].

## 2 Introduction

The study of Sturm between 1829 and 1836 serves as the basis of the Sturm-Liouville (S-L) theory. Later, the brief but crucial study of Sturm-Liouville was published in 1837. In this study, they addressed the boundary value problem (BVP) for the differential equation given as

$$-y'' + q(x)y = \lambda y, \quad 0 \leq x \leq 1, \quad (7)$$

where  $\lambda$  is a complex parameter and  $q$  is a real-valued function that can be quadratically integrated over the interval  $[0, 1]$ . Sturm and Liouville examined whether there are nontrivial solutions of Eq. (7) satisfying the following boundary conditions [4]:

$$\begin{aligned} y(0) \cos \gamma_1 + y'(0) \sin \gamma_1 &= 0, \\ y(1) \cos \gamma_2 + y'(1) \sin \gamma_2 &= 0. \end{aligned} \quad (8)$$

Here,  $\gamma_1$  and  $\gamma_2$  are real numbers between 0 and  $\pi$ . If (7)-(8) BVP is solved, the complex number  $\lambda$  is called the eigenvalue of  $q$ ,  $\gamma_1$ , and  $\gamma_2$ . Also, the nontrivial solutions for  $\lambda$  are called eigenfunctions of  $q$ ,  $\gamma_1$ , and  $\gamma_2$ . The set of all eigenvalues is the spectrum of the BVP given by (7)-(8). Significant advances in spectral theory have been achieved for the Sturm-Liouville operator as follows

$$l = -\frac{d^2}{dx^2} + q(x), \quad (9)$$

sometimes also called the one-dimensional time-dependent Schrödinger operator.

The first investigations on spectral theory for such operators were performed by Bernoulli, D'alambert, Euler, Sturm, and Liouville for rod vibration problems. In the 20th century, spectral theory developed rapidly for different classes of differential and integral operators. Famous mathematicians including Birkhoff, Hilbert, Neumann, Steklov, Stone, and Weyl as well as many others have made major contributions to this topic through outstanding ideas. On the other hand, the main conclusions regarding the inverse problems of spectral theory were obtained in the second half of the 20th century. Particularly in the latter half of the 20th century, the techniques employed to study the Sturm-Liouville operator have continuously improved. For instance, in 1967, a group of American physicists and mathematicians Gardner, Greene, Kruskal, and Miura developed an important method by solving the Korteweg-de Vries (KDV) equation for a proposed initial condition through using the inverse scattering method. In 1968, Lax evaluated the inverse scattering method in a more general frame by solving the KDV equation with the help of linear equations, and this frame later opened the way for generalizing the technique as a method for solving other partial differential equations. The initial value problems of nonlinear partial differential equations can be solved utilizing the inverse scattering method. The approach is based on converting the initial value problem into a linear integral equation. Both mathematicians and physicists continue to focus more on the inverse scattering problems of quantum theory for singular Sturm-Liouville operators, which have numerous applications in this area and geophysics [4]. For more information of fractional calculus in application, S-L problem and to see the S-L problem in fractional calculus we refer the reader to [5–14].

This manuscript is organized as follows: In [Section 1](#), we give a motivation part on the proportional derivative by mentioning its importance in control theory before writing the introduction part in [Section 2](#). Then, the model description and solution method in order to solve the S-L problem are given in [Section 3](#). Additionally, we obtain the representation of the solution for the S-L

problem through the proportional derivative operator in Section 4. On the other hand, in Section 5, various graphs are shown for different values of arbitrary order  $\eta$  and eigenvalues. Finally, we introduce some crucial concluding remarks of this study in Section 6.

### 3 Model description and solution method

The Sturm-Liouville operator  $T$  can be expressed through the proportional derivative as below:

$$T \equiv -{}_p\mathbf{D}^\eta ({}_p\mathbf{D}^\eta) + q(x), \quad (10)$$

where  $\eta \in (0, 1]$  and  $q(x)$  is a real-valued continuous function on interval  $[a, b]$ . Here, the main objective is to consider the S-L problem having separated boundary conditions given by

$$Ty(x) = -{}_p\mathbf{D}^\eta [{}_p\mathbf{D}^\eta y(x)] + q(x)y(x) = \lambda y(x), \quad (11)$$

$$\begin{aligned} y(a) \cos \gamma_1 + {}_p\mathbf{D}^\eta y(a) \sin \gamma_1 &= 0, \\ y(b) \cos \gamma_2 + {}_p\mathbf{D}^\eta y(b) \sin \gamma_2 &= 0. \end{aligned} \quad (12)$$

If we take  $\cot \gamma_1 = -h$  and  $\cot \gamma_2 = H$  for  $a = 0$  and  $b = \pi$ , that is  $x \in [0, \pi]$ , the boundary condition (12) takes the following form

$$\begin{aligned} {}_p\mathbf{D}^\eta y(0) - hy(0) &= 0, \\ {}_p\mathbf{D}^\eta y(\pi) + Hy(\pi) &= 0. \end{aligned} \quad (13)$$

Furthermore, the BVP (11)-(12) has a nontrivial solution denoted by  $y(x, \lambda_n)$  for any  $\lambda_n$ . Also,  $\lambda_n$  and  $y(x, \lambda_n)$  are called as eigenvalue and eigenfunction, respectively. In [15], the variation of parameters method is defined by means of the proportional derivative. While this generalization can be used to solve many real-life problems, it also enables the behavior of the problems to be examined in more detail by obtaining more general solutions.

Let  $0 \leq \eta \leq 1$  and  $n \in \{1, 2, 3, \dots\}$ , then  ${}_p\mathbf{D}^{n\eta} y(x)$  is given by  ${}_p\mathbf{D}^{n\eta} y = {}_p\mathbf{D}^\eta {}_p\mathbf{D}^\eta \dots {}_p\mathbf{D}^\eta y$ . For simplicity of notation, one can write  $y^{(n\eta)}(x)$  instead of  ${}_p\mathbf{D}^{n\eta} y(x)$ . Hence, here, the expression of  $y^{(2\eta)}(x)$  means that  $\frac{d^{2\eta}}{dx^{2\eta}} \left( \frac{d^\eta y}{dx^\eta} \right)$ .

The variation of parameters method, which is often used to find a particular solution of non-homogeneous linear differential equations with constant or variable coefficients, is defined by the proportional derivative as follows. It is well-known that the homogeneous part of a differential equation of form (11) has two linearly independent solutions,  $y_1(x)$  and  $y_2(x)$ . In this situation, we have a particular solution of the proposed equation as  $y_p(x) = v_1(x)y_1(x) + v_2(x)y_2(x)$ . Hence, with respect to the proportional variation of parameters method, we have the formulas addressed by

$$v_1'(x) = \frac{q(x)y(x)y_2(x)}{K_0^2(\eta, x)W_p(y_1, y_2)(x)}, \quad v_2'(x) = \frac{-q(x)y(x)y_1(x)}{K_0^2(\eta, x)W_p(y_1, y_2)(x)}, \quad (14)$$

where  $W_p(y_1, y_2)(x)$  is the proportional Wronskian defined as

$$W_p(y_1, y_2)(x) = \begin{vmatrix} y_1(x) & y_2(x) \\ {}_p\mathbf{D}^\eta y_1(x) & {}_p\mathbf{D}^\eta y_2(x) \end{vmatrix}. \quad (15)$$

Therefore, if we apply the integral to the functions  $v_1'(x)$  and  $v_2'(x)$ , we get the functions  $v_1(x)$  and  $v_2(x)$ . By substituting these functions to the  $y_p(x)$ , we reach the particular solution. As a result, the general solution is obtained by calculating the sum of the solution of the homogeneous part of the equation under consideration and particular solution  $y_p(x)$ . For more information on proportional derivatives and applications of different types of fractional derivatives, we refer the reader to [16–20].

#### 4 Main results

In the current section, we introduce the representation of the solution for the S-L problem employing the proportional derivative. Here, we use two suitable initial conditions and so we get two representations of the solution by utilizing the proportional variation of parameters method. Let  $\varphi(x, \lambda)$  be the solution of Eq. (11) with the initial condition given as

$$\varphi(0, \lambda) = 1, \quad {}_p\mathbf{D}^\eta \varphi(0, \lambda) = h, \quad (16)$$

and the other solution is  $\Phi(x, \lambda)$  under the following initial condition

$$\Phi(0, \lambda) = 0, \quad {}_p\mathbf{D}^\eta \Phi(0, \lambda) = 1. \quad (17)$$

In order to obtain the solutions  $\varphi(x, \lambda)$  and  $\Phi(x, \lambda)$ , we benefit from the proportional variation of parameters method. For this purpose, we employ the solution of the homogeneous counterpart of Eq. (11) obtained as

$$y_h(x) = c_1 e_0(x, 0) \cos \left( \int_0^x \frac{\sqrt{\lambda}}{K_0(\eta, s)} ds \right) + c_2 e_0(x, 0) \sin \left( \int_0^x \frac{\sqrt{\lambda}}{K_0(\eta, s)} ds \right). \quad (18)$$

On the other hand, for the non-homogeneous equation (11), we assume that

$$y_p(x) = v_1(x) e_0(x, 0) \cos \left( \int_0^x \frac{\sqrt{\lambda}}{K_0(\eta, s)} ds \right) + v_2(x) e_0(x, 0) \sin \left( \int_0^x \frac{\sqrt{\lambda}}{K_0(\eta, s)} ds \right). \quad (19)$$

Also, the p-Wronskian can be computed as below:

$$W_p = \begin{vmatrix} e^{-\int_0^x \frac{K_1(\eta, \tau)}{K_0(\eta, \tau)} d\tau} \cos \left( \int_0^x \frac{\sqrt{\lambda}}{K_0(\eta, s)} ds \right) & e^{-\int_0^x \frac{K_1(\eta, \tau)}{K_0(\eta, \tau)} d\tau} \sin \left( \int_0^x \frac{\sqrt{\lambda}}{K_0(\eta, s)} ds \right) \\ {}_p\mathbf{D}^\eta \left[ e^{-\int_0^x \frac{K_1(\eta, \tau)}{K_0(\eta, \tau)} d\tau} \cos \left( \int_0^x \frac{\sqrt{\lambda}}{K_0(\eta, s)} ds \right) \right] & {}_p\mathbf{D}^\eta \left[ e^{-\int_0^x \frac{K_1(\eta, \tau)}{K_0(\eta, \tau)} d\tau} \sin \left( \int_0^x \frac{\sqrt{\lambda}}{K_0(\eta, s)} ds \right) \right] \end{vmatrix}, \quad (20)$$

and if we choice  $K_1(\eta, s) = 1 - \eta$  and  $K_0(\eta, s) = \eta$ , we reach

$$W_p = \begin{vmatrix} e^{-\frac{(1-\eta)}{\eta}x} \cos \left( \frac{\sqrt{\lambda}}{\eta}x \right) & e^{-\frac{(1-\eta)}{\eta}x} \sin \left( \frac{\sqrt{\lambda}}{\eta}x \right) \\ {}_p\mathbf{D}^\eta \left[ e^{-\frac{(1-\eta)}{\eta}x} \cos \left( \frac{\sqrt{\lambda}}{\eta}x \right) \right] & {}_p\mathbf{D}^\eta \left[ e^{-\frac{(1-\eta)}{\eta}x} \sin \left( \frac{\sqrt{\lambda}}{\eta}x \right) \right] \end{vmatrix}, \quad (21)$$

$${}_p\mathbf{D}^\eta \left[ e^{-\frac{(1-\eta)}{\eta}x} \cos \left( \frac{\sqrt{\lambda}}{\eta}x \right) \right] = e^{-\frac{(1-\eta)}{\eta}x} \left[ \cos \left( \frac{\sqrt{\lambda}}{\eta}x \right) - \sqrt{\lambda} \sin \left( \frac{\sqrt{\lambda}}{\eta}x \right) \right], \quad (22)$$

and

$${}_p\mathbf{D}^\eta \left[ e^{-\frac{(1-\eta)x}{\eta}} \sin \left( \frac{\sqrt{\lambda}}{\eta} x \right) \right] = e^{-\frac{(1-\eta)x}{\eta}} \left[ \sin \left( \frac{\sqrt{\lambda}}{\eta} x \right) - \sqrt{\lambda} \cos \left( \frac{\sqrt{\lambda}}{\eta} x \right) \right]. \quad (23)$$

Hence we get p-Wronskian as

$$W_p = \sqrt{\lambda} e^{\frac{2(\eta-1)x}{\eta}}. \quad (24)$$

By taking the integral of following expressions

$$v_1'(x) = \frac{y_2(x)q(x)y(x)}{\eta^2 W_p}, \quad v_2'(x) = \frac{-y_1(x)q(x)y(x)}{\eta^2 W_p}, \quad (25)$$

it can be reached the functions  $v_1(x)$  and  $v_2(x)$  as follows

$$v_1(x) = \int_0^x \frac{e^{-\frac{(1-\eta)t}{\eta}} \sin \left( \frac{\sqrt{\lambda}}{\eta} t \right)}{\eta^2 \sqrt{\lambda} e^{\frac{2(\eta-1)t}{\eta}}} q(t)y(t) dt, \quad v_2(x) = - \int_0^x \frac{e^{-\frac{(1-\eta)t}{\eta}} \cos \left( \frac{\sqrt{\lambda}}{\eta} t \right)}{\eta^2 \sqrt{\lambda} e^{\frac{2(\eta-1)t}{\eta}}} q(t)y(t) dt. \quad (26)$$

If we arrange the above formulas, we get

$$v_1(x) = \frac{1}{\eta^2 \sqrt{\lambda}} \int_0^x e^{\frac{(1-\eta)t}{\eta}} \sin \left( \frac{\sqrt{\lambda}}{\eta} t \right) q(t)y(t) dt, \quad (27)$$

and

$$v_2(x) = \frac{-1}{\eta^2 \sqrt{\lambda}} \int_0^x e^{\frac{(1-\eta)t}{\eta}} \cos \left( \frac{\sqrt{\lambda}}{\eta} t \right) q(t)y(t) dt. \quad (28)$$

Substituting the functions  $v_1(x)$  and  $v_2(x)$  into Eq. (19), one can readily have

$$\begin{aligned} y_p(x) &= e^{-\frac{(1-\eta)x}{\eta}} \cos \left( \frac{\sqrt{\lambda}}{\eta} x \right) \frac{1}{\eta^2 \sqrt{\lambda}} \int_0^x e^{\frac{(1-\eta)t}{\eta}} \sin \left( \frac{\sqrt{\lambda}}{\eta} t \right) q(t)y(t) dt \\ &\quad - e^{-\frac{(1-\eta)x}{\eta}} \sin \left( \frac{\sqrt{\lambda}}{\eta} x \right) \frac{1}{\eta^2 \sqrt{\lambda}} \int_0^x e^{\frac{(1-\eta)t}{\eta}} \cos \left( \frac{\sqrt{\lambda}}{\eta} t \right) q(t)y(t) dt. \end{aligned} \quad (29)$$

Thereby, the general solution is obtained as

$$\begin{aligned} y(x) &= c_1 e^{-\frac{(1-\eta)x}{\eta}} \cos \left( \frac{\sqrt{\lambda}}{\eta} x \right) + c_2 e^{-\frac{(1-\eta)x}{\eta}} \sin \left( \frac{\sqrt{\lambda}}{\eta} x \right) \\ &\quad + \frac{1}{\eta^2 \sqrt{\lambda}} \int_0^x q(t)y(t) e^{\frac{(1-\eta)t}{\eta}} \sin \left[ \frac{\sqrt{\lambda}}{\eta} (x-t) \right] dt. \end{aligned} \quad (30)$$

Let  $\lambda$  be  $s^2$ , then by applying the initial condition (16), we have the solution as follows

$$\begin{aligned} \varphi(x, s) = & e^{-\frac{(1-\eta)}{\eta}x} \cos\left(\frac{s}{\eta}x\right) + \frac{h}{s} e^{-\frac{(1-\eta)}{\eta}x} \sin\left(\frac{s}{\eta}x\right) \\ & + \frac{1}{s\eta^2} \int_0^x q(t)\varphi(t) e^{\frac{(1-\eta)}{\eta}t} \sin\left[\frac{s}{\eta}(x-t)\right] dt, \end{aligned} \quad (31)$$

and utilizing the initial condition (17), we can get the solution

$$\Phi(x, s) = \frac{1}{s} e^{-\frac{(1-\eta)}{\eta}x} \sin\left(\frac{s}{\eta}x\right) + \frac{1}{s\eta^2} \int_0^x q(t)\Phi(t) e^{\frac{(1-\eta)}{\eta}t} \sin\left[\frac{s}{\eta}(x-t)\right] dt. \quad (32)$$

## 5 Visual results and discussions

This section includes graphs of the solution functions of S-L problem that are achieved by employing the benefits of proportional derivative. The behavior of the representation of solution function  $\varphi(x, s)$  for the classical situation is first demonstrated when  $s = 1, 2, 3$ , and then it is shown how the solution curve motions vary for  $\eta = 0.9, 0.7, 0.5$  in [Figure 2](#) and [Figure 3](#). On the S-L problem, which has physically crucial meanings, it has been clearly observed how different order values of the proportional derivative affect the problem and how they change the behavior of the solution functions.

On the other hand, it should be expressed that the reason for using the same eigenvalues is to see the effect of different order values. In [Figure 4-Figure 5](#), we demonstrate how the solutions change as the  $\eta$  parameter takes different values for  $s=1, s=3$  and  $s=5$ , respectively. Additionally, [Figure 6](#) shows the behavior of the function  $\varphi(x, s)$  for  $\eta = 1, 0.8, 0.6, 0.4$  when  $s = \sqrt{0.1}$ . Afterwards, similarly, we plot the graphs for the solution function  $\varphi(x, s)$  by using the same parameter values for the solution function  $\Phi(x, s)$  in [Figure 7-Figure 10](#). Here, the representation of solution function  $\varphi(x, s)$  under the condition (16) is

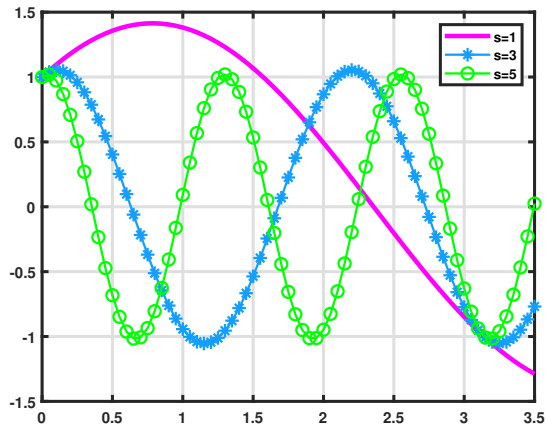
$$\begin{aligned} \varphi(x, s) = & e^{-\frac{(1-\eta)}{\eta}x} \cos\left(\frac{s}{\eta}x\right) + \frac{h}{s} e^{-\frac{(1-\eta)}{\eta}x} \sin\left(\frac{s}{\eta}x\right) \\ & + \frac{1}{s\eta^2} \int_0^x q(t)\varphi(t) e^{\frac{(1-\eta)}{\eta}t} \sin\left[\frac{s}{\eta}(x-t)\right] dt, \end{aligned} \quad (33)$$

and the representation of solution function  $\Phi(x, s)$  under the condition (17) is

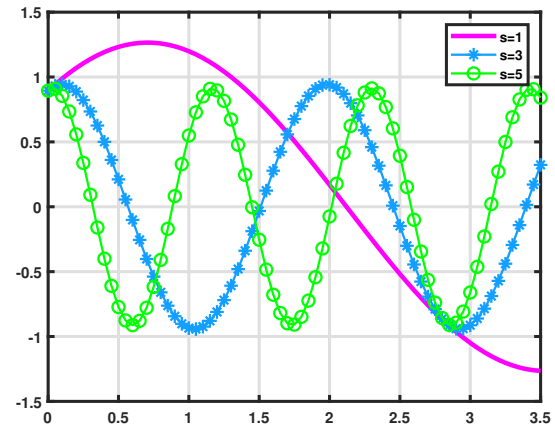
$$\Phi(x, s) = \frac{1}{s} e^{-\frac{(1-\eta)}{\eta}x} \sin\left(\frac{s}{\eta}x\right) + \frac{1}{s\eta^2} \int_0^x q(t)\Phi(t) e^{\frac{(1-\eta)}{\eta}t} \sin\left[\frac{s}{\eta}(x-t)\right] dt. \quad (34)$$

All graphs are obtained by the various values of arbitrary order and eigenvalues when the potential function  $q(t) = 0$ . Accordingly, the main objective of the graphs is to see the effect of the eigenvalues, which are important for the problem under investigation, on the solution functions and to observe the effect of the proportional derivative on the S-L problem. To observe these two situations separately, which are important for the current study, in some graphs, eigenvalues are not changed, while arbitrary order of proportional derivative values are changed.

In a similar way, to see the effect of the eigenvalues, the derivative order is not changed and the eigenvalues are changed.

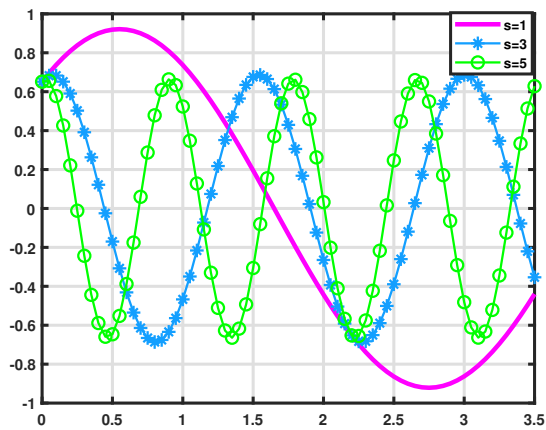


(a)

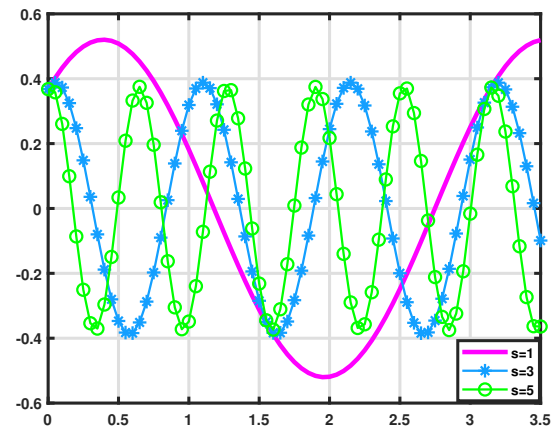


(b)

**Figure 2.** The solutions curves of the function  $\varphi(x, s)$  when  $\eta = 1$  (classical case) (a) and  $\eta = 0.9$  (arbitrary order case) (b) for the values of  $s = 1, 3, 5$  (this corresponds to the  $\lambda = 1, 9, 25$  eigenvalues) under the condition (16).

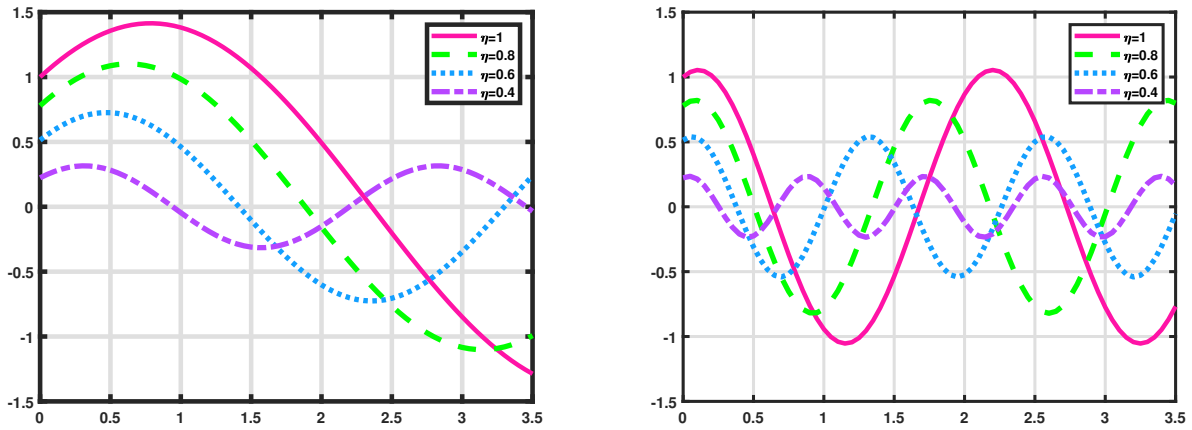


(a)



(b)

**Figure 3.** The solutions curves of the function  $\varphi(x, s)$  when  $\eta = 0.7$  (a) and  $\eta = 0.5$  (b) for the values of  $s = 1, 3, 5$  (this corresponds to the  $\lambda = 1, 9, 25$  eigenvalues) under the condition (16).



(a)

(b)

**Figure 4.** The solutions curves of the function  $\varphi(x, s)$  when  $s = 1$  (a) and  $s = 3$  (b) for different values of arbitrary order  $\eta = 1, 0.8, 0.6, 0.4$ .

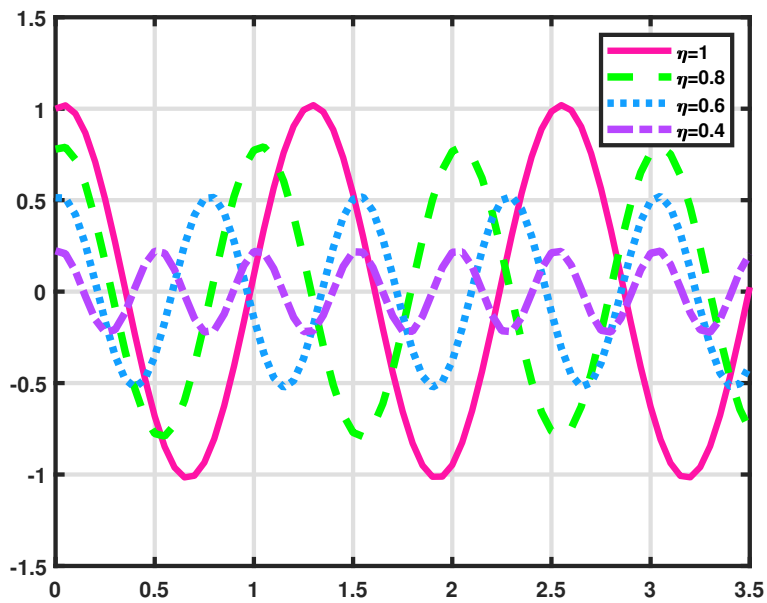


**Figure 5.** The solutions curves of the function  $\varphi(x, s)$  when  $s = 5$  for different values of arbitrary order  $\eta = 1, 0.8, 0.6, 0.4$ .

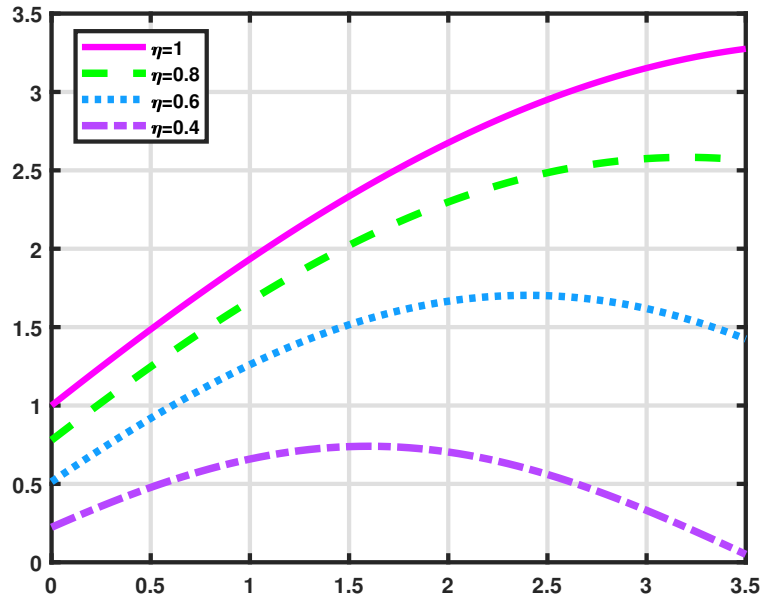
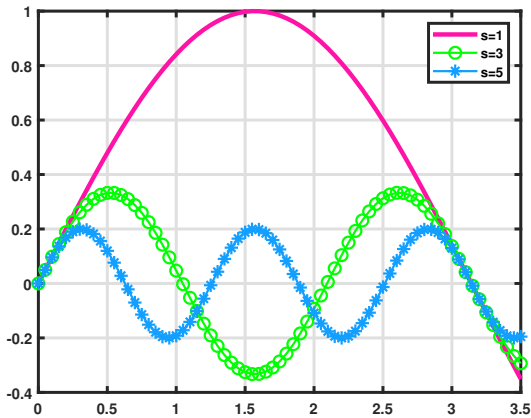
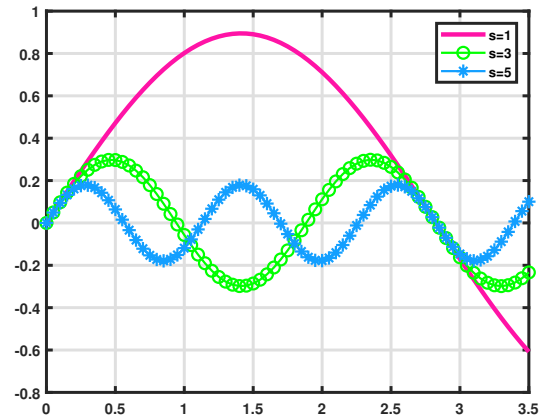


Figure 6. The solution curves of the function  $\varphi(x, s)$  when  $s = \sqrt{0.1}$  for different values of arbitrary order  $\eta = 1, 0.8, 0.6, 0.4$ .



(a)



(b)

Figure 7. The solutions curves of the function  $\Phi(x, s)$  when  $\eta = 1$  (classical case) (a) and  $\eta = 0.9$  (arbitrary order case) (b) for the values of  $s = 1, 3, 5$  (this corresponds to the  $\lambda = 1, 9, 25$  eigenvalues) under the condition (17).

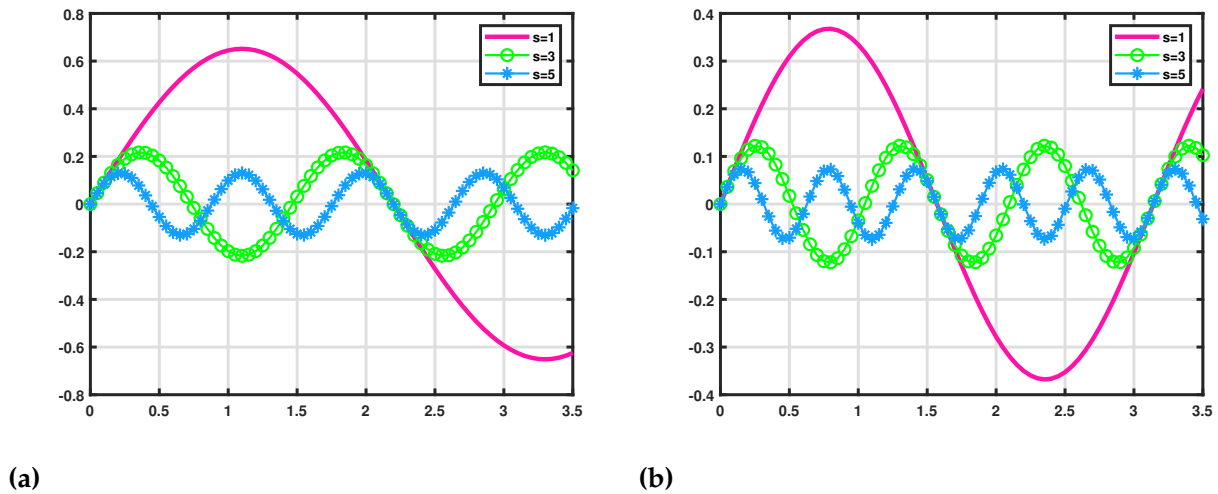


**Figure 8.** The solutions curves of the function  $\Phi(x, s)$  when  $\eta = 0.7$  (a) and  $\eta = 0.5$  (b) for the values of  $s = 1, 3, 5$  (this corresponds to the  $\lambda = 1, 9, 25$  eigenvalues) under the condition (17).

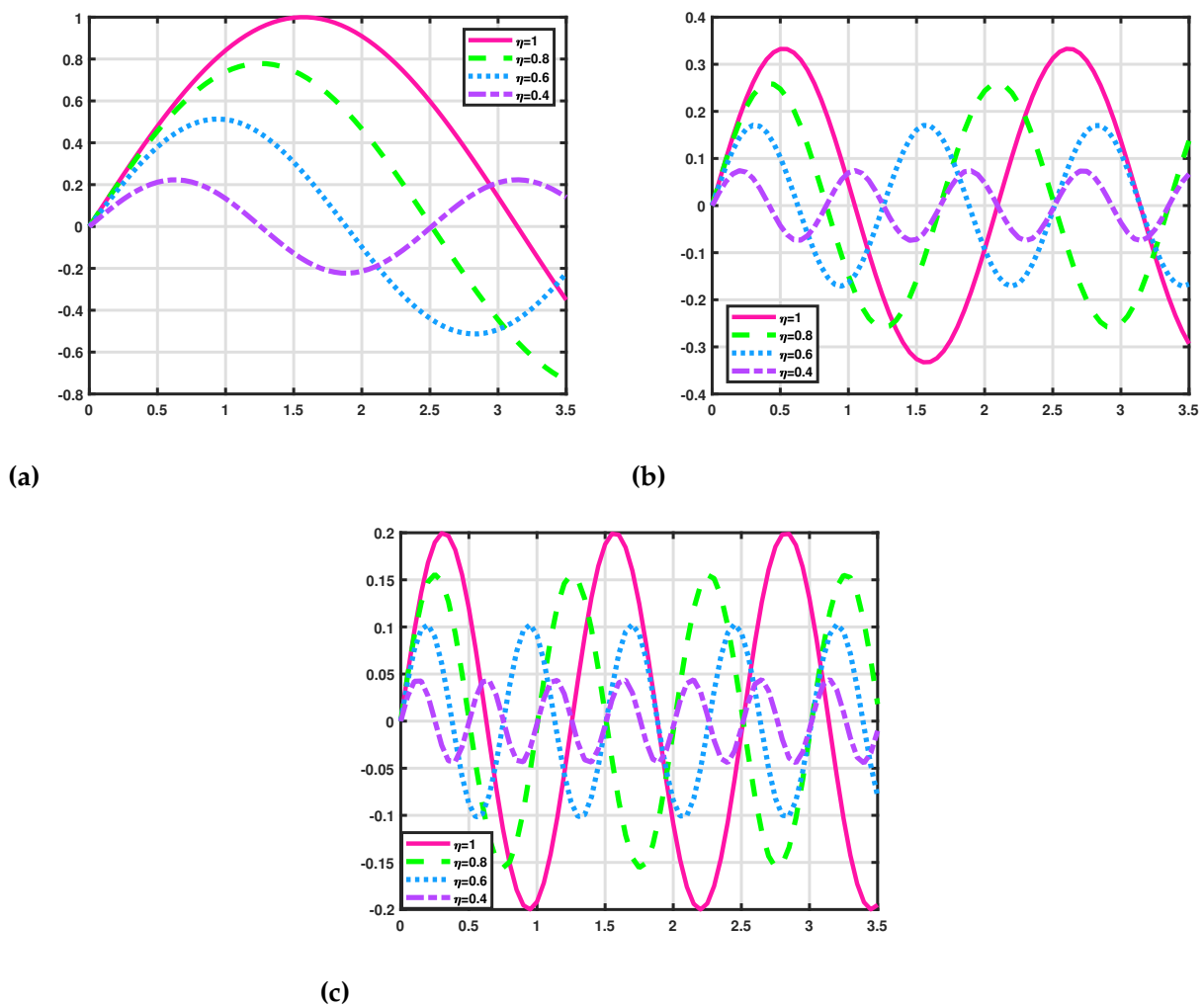


**Figure 9.** The solutions curves of the function  $\Phi(x, s)$  when  $s = 1$  (a),  $s = 3$  (b), and  $s = 5$  (c) for different values of arbitrary order  $\eta = 1, 0.8, 0.6, 0.4$ .

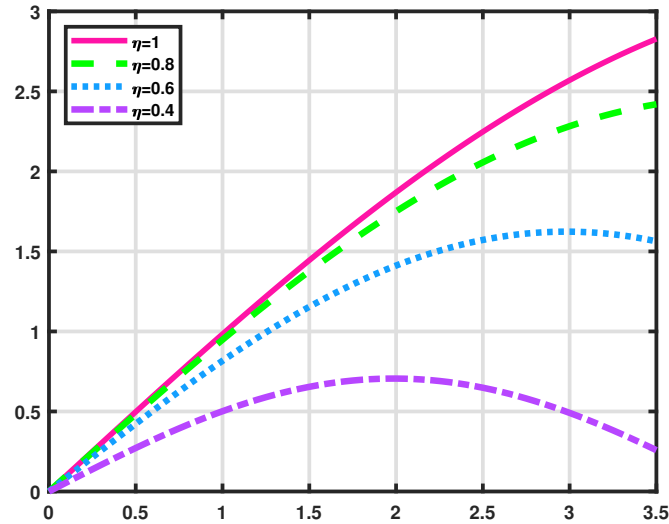


**Figure 10.** The solution curves of the function  $\Phi(x, s)$  when  $s = \sqrt{0.1}$  for different values of arbitrary order  $\eta = 1, 0.8, 0.6, 0.4$ .

## 6 Concluding remarks

The proportional derivative, which is considered in the class of local derivatives including arbitrary order, is considered more advantageous than other local derivatives in terms of its features. Since it is based on control theory, it has an important place, especially in engineering. In [2], the authors state that since the unit operator cannot be obtained for the other local derivatives when  $\mathcal{D}^0\omega \neq \omega$ , that is,  $\chi \rightarrow 0$ , and on the other hand, there is a  $t \geq 0$  condition to satisfy the  $\mathbf{D}^\chi\omega(t) = t^{1-\chi}\omega'(t)$  formula, they have introduced a novel definition of local derivative called proportional derivative in order to overcome these restrictions. This new and seemingly more well-founded local derivative definition is created in such a way that  $\mathbf{D}^0$  corresponds to the unit operator and  $\mathbf{D}^1$  corresponds to the integer-order classical derivative, while  $0 \leq \chi \leq 1$  and  $t \in \mathbb{R}$ . In the definition of the proportional derivative, various special cases can be obtained for different choices of the functions  $K_1(\eta, t)$  and  $K_0(\eta, t)$ . For example, proportional derivatives of special types can be obtained by choosing for any  $\omega \in (0, \infty)$ ,  $K_1 \equiv (1 - \chi)\omega^\chi$  and  $K_0 \equiv \chi\omega^{1-\chi}$ ,  $K_1 = (1 - \chi)|t|^\chi$  and  $K_0 = \chi|t|^{1-\chi}$  on  $\mathbb{R} \setminus \{0\}$ , or  $K_1 = \cos(\chi\pi/2)|t|^\chi$  and  $K_0 = \sin(\chi\pi/2)|t|^{1-\chi}$ . This can be seen as another advantage of the proportional derivative. Because, in application, one can have the opportunity to obtain better results by making the special choices needed according to the behavior of the problem under consideration. Therefore, attention should be paid to whether the special choices made are useful and meaningful in application. Due to all these advantages, the proportional derivative is preferred in solving the S-L equation in this study. It is thought that the results obtained as an alternative to the classical derivative will be useful for experts in the field.

Also, it should be emphasized that addressing and examining the S-L problem, which is of great physical importance, with the help of proportional derivatives used in control theory, can make a significant contribution to the literature. It is known that there are many different S-L problems in the literature. Therefore, this study is important in terms of encouraging the application of proportional derivative to different problems in this field.

## Declarations

### List of abbreviations

Not applicable.

### Ethical approval

The author states that this research complies with ethical standards. This research does not involve either human participants or animals.

### Consent for publication

Not applicable.

### Conflicts of interest

The author confirms that there is no competing interest in this study.

### Data availability statement

Data availability is not applicable to this article as no new data were created or analyzed in this study.

### Funding

This research received no specific grant from any funding agency in the public, commercial, or not-for-profit sectors.

### Author's contributions

The author has made substantial contributions to the conception, design of the work, the acquisition, analysis, interpretation of data, and the creation of new software used in the work.

## References

- [1] Miller, K.S. and Ross, B. *An introduction to the fractional calculus and fractional differential equations*. New York: John Wiley and Sons, (1993).
- [2] Anderson, D.R. and Ulness, D.J. Newly defined conformable derivatives. *Advances in Dynamical Systems and Applications*, 10(2), 109-137, (2015). [[CrossRef](#)]
- [3] Li, Y., Ang, K.H. and Chong, G.C.Y. PID control system analysis and design. *IEEE Control Systems Magazine*, 26(1), 32-41, (2006). [[CrossRef](#)]
- [4] Levitan, B.M. and Sargsujan, I.S. *Introduction to Spectral Theory: Selfadjoint Ordinary Differential Operators* (Vol. 39). American Mathematical Society: Providence, (1975).
- [5] Klimek, M. and Agrawal, O.P. Fractional Sturm–Liouville problem. *Computers & Mathematics with Applications*, 66(5), 795-812, (2013). [[CrossRef](#)]
- [6] Zayernouri, M. and Karniadakis, G.E. Fractional Sturm–Liouville eigen-problems: Theory and numerical approximation. *Journal of Computational Physics*, 252, 495-517, (2013). [[CrossRef](#)]
- [7] Al-Mdallal, Q.M. An efficient method for solving fractional Sturm–Liouville problems. *Chaos, Solitons & Fractals*, 40(1), 183-189, (2009). [[CrossRef](#)]
- [8] Allahverdiev, B.P., Tuna, H. and Yalçinkaya, Y. Conformable fractional Sturm-Liouville equation. *Mathematical Methods in the Applied Sciences*, 42(10), 3508-3526, (2019). [[CrossRef](#)]

- [9] Bas, E. and Acay, B. The direct spectral problem via local derivative including truncated Mittag-Leffler function. *Applied Mathematics and Computation*, 367, 124787, (2020). [[CrossRef](#)]
- [10] Ercan, A. Comparative analysis for fractional nonlinear Sturm-Liouville equations with singular and non-singular kernels. *AIMS Mathematics*, 7(7), 13325-13343, (2022). [[CrossRef](#)]
- [11] Ercan, A. Conformable Discontinuous Sturm-Liouville Problem with Applied Results. *International Journal of Applied Mathematics and Statistics*, 61(1), 71-81, (2022). [[CrossRef](#)]
- [12] Ercan, A. and Panakhov, E. Stability of the reconstruction discontinuous Sturm-Liouville problem. *Communications Faculty of Sciences University of Ankara Series A1 Mathematics and Statistics*, 68(1), 484-499, (2019). [[CrossRef](#)]
- [13] Hammouch, Z., Yavuz, M. and Özdemir, N. Numerical solutions and synchronization of a variable-order fractional chaotic system. *Mathematical Modelling and Numerical Simulation with Applications*, 1(1), 11-23, (2021). [[CrossRef](#)]
- [14] Yavuz, M., Ozdemir, N. and Baskonus, H.M. Solutions of partial differential equations using the fractional operator involving Mittag-Leffler kernel. *The European Physical Journal Plus*, 133, 215, (2018). [[CrossRef](#)]
- [15] Acay, B., Inc, M., Chu, Y.M. and Almohsen, B. Modeling of pressure-volume controlled artificial respiration with local derivatives. *Advances in Difference Equations*, 2021, 1-21, (2021). [[CrossRef](#)]
- [16] Baleanu, D., Fernandez, A. and Akgül, A. On a fractional operator combining proportional and classical differintegrals. *Mathematics*, 8(3), 1-13, (2020). [[CrossRef](#)]
- [17] Jarad, F., Alqudah, M.A., Abdeljawad, T. On more general forms of proportional fractional operators. *Open Mathematics*, 18(1), 167-176, (2020). [[CrossRef](#)]
- [18] Jarad, F., Abdeljawad, T. and Alzabut, J. Generalized fractional derivatives generated by a class of local proportional derivatives. *The European Physical Journal Special Topics*, 226, 3457-3471, (2017). [[CrossRef](#)]
- [19] Acay, B. and Inc, M. Electrical circuits RC, LC, and RLC under generalized type non-local singular fractional operator. *Fractal and Fractional*, 5(1), 9, (2021). [[CrossRef](#)]
- [20] Acay, B., Bas, E. and Abdeljawad, T. Non-local fractional calculus from different viewpoint generated by truncated M-derivative. *Journal of Computational and Applied Mathematics*, 366, 112410, (2020). [[CrossRef](#)]

Mathematical Modelling and Numerical Simulation with Applications (MMNSA)

(<https://dergipark.org.tr/en/pub/mmnsa>)



**Copyright:** © 2023 by the authors. This work is licensed under a Creative Commons Attribution 4.0 (CC BY) International License. The authors retain ownership of the copyright for their article, but they allow anyone to download, reuse, reprint, modify, distribute, and/or copy articles in MMNSA, so long as the original authors and source are credited. To see the complete license contents, please visit (<http://creativecommons.org/licenses/by/4.0/>).

**How to cite this article:** Acay Öztürk, B. (2023). Examination of Sturm-Liouville problem with proportional derivative in control theory. *Mathematical Modelling and Numerical Simulation with Applications*, 3(4), 335-350. <https://doi.org/10.53391/mmnsa.1392796>



RESEARCH PAPER

## Genocchi collocation method for accurate solution of nonlinear fractional differential equations with error analysis

Mohamed El-Gamel <sup>1,†</sup>, Nesreen Mohamed <sup>2,‡</sup> and Waleed Adel <sup>1,3,\*,‡</sup>

<sup>1</sup>Department of Mathematics and Engineering Physics, Faculty of Engineering, Mansoura University, 35511, Egypt, <sup>2</sup>Department of Basic Science, Faculty of Engineering, Horus University Egypt, New Damietta, 34518, Egypt, <sup>3</sup>Laboratoire Interdisciplinaire de l'Universite Francaise d'Egypte (UFEID Lab), Universite Francaise d'Egypte, Cairo, 11837, Egypt

\*Corresponding Author

† gamel-eg@yahoo.com (Mohamed El-Gamel); nesreen.msedik@gmail.com (Nesreen Mohamed); waleedadel@mans.edu.eg (Waleed Adel)

### Abstract

In this study, we introduce an innovative fractional Genocchi collocation method for solving nonlinear fractional differential equations, which have significant applications in science and engineering. The fractional derivative is defined in the Caputo sense and by leveraging fractional-order Genocchi polynomials, we transform the nonlinear problem into a system of nonlinear algebraic equations. A novel technique is employed to solve this system, enabling the determination of unknown coefficients and ultimately the solution. We derive the error bound for our proposed method and validate its efficacy through several test problems. Our results demonstrate superior accuracy compared to existing techniques in the literature, suggesting the potential for extending this approach to tackle more complex problems of critical physical significance.

**Keywords:** Fractional-order modelling; collocation method; nonlinear phenomena; error bound

**AMS 2020 Classification:** 34A08; 65L60; 65L70

### 1 Introduction

During the last few years, fractional calculus (FC) has gained significant attention in the scientific and engineering communities due to its ability to provide more realistic simulations of real-life complex phenomena. FC is defined as the branch of mathematics that deals with derivatives and integrals of non-integer orders. Unlike traditional calculus, which focuses on integer-order derivatives and integrals, FC extends these operations to include fractional orders. The importance

of the application of FC comes from the fact that it involves the derivative and integral of any order and is particularly useful in simulating models that exhibit memory effects or cannot be adequately described by classical approaches. With these important remarks and properties, researchers have been trying over the years to develop several definitions of FC [1]. One of the common definitions of FC is the Riemann-Liouville fractional derivative, which is defined as the integral of a function raised to a fractional power, followed by differentiation. On the other hand, another well-known important definition is the Caputo fractional derivative, which is defined as the integral of a function multiplied by a weight function, followed by differentiation [2]. The Caputo fractional derivative is one of the most important definitions in the field of FC due to many reasons. First, it can handle initial conditions more efficiently and can handle non-smooth functions and discontinuities. In addition, unlike other operators that require knowledge of the function's history at all times, the Caputo derivative only requires the function's values at the current time. This property makes this definition suitable for modeling real-world phenomena where the initial conditions are unknown or hard to obtain. Also, this definition provides the ability to handle non-smooth functions and discontinuities more effectively compared to other fractional operators. This makes it more versatile and applicable in a wider range of applications. Other definitions of fractional operators include the Grunwald-Letnikov fractional derivative, which is defined as a finite difference approximation of the fractional derivative, and the Atangana-Baleanu fractional derivative, which is defined using the Caputo fractional derivative and a non-singular kernel. Each of these definitions has its advantages and limitations and is suitable for specific applications. Choosing the appropriate fractional operator for a given problem requires careful consideration of the problem's nature and the desired properties of the solution.

In many real-life applications, differential equations are used to model physical processes, and the development of fractional calculus has led to a growing interest in fractional differential equations (FDEs). The study of FDEs has significant implications in various fields, including physics, engineering, and finance. For example, Kilbas et al. [3] were among the first to introduce the basics of fractional calculus and its application to differential equations. Podlubny [4] further expanded on the possible applications of fractional calculus to differential equations and was one of the earliest researchers to study FDEs. Agarwal et al. [5] investigated solutions to a class of semi-linear FDEs in the form of periodic solutions. In the field of biology, Rahman et al. [6] adapted the singular-type and nonsingular fractional-order derivatives for simulating the plant-pathogen-herbivore interactions model. Additionally, Ali et al. [7] employed the new sub-equation method to attain new traveling wave solutions of conformable time FDEs. Moreover, Uzun et al. [8] studied the forced oscillatory theory for higher-order fractional differential equations with a damping term via the  $\psi$ -Hilfer fractional derivative. In the field of biology, FDEs have been contributing to the understanding of the dynamics and spread of many viruses. For example, Atede et al. [9] investigated the solution of a COVID-19 model incorporating the effect of vaccination through a fractional model with verification using real data from Nigeria. Also, Anjam et al. [10] simulated the dynamics of a fractional pollution model in a system of three interconnecting lakes. These are some examples of the applications of FDEs in simulating real-life phenomena. For more details on the application of FDEs, the reader may refer to [11–17] and references therein.

In this paper, we introduce the Genocchi collocation method for solving the following form of fractional differential equation

$$u^{(\eta)}(x) = \sum_{m=0}^r \sigma_m u^{(m)}(x) + \mu(x, u(x)), \quad a < x < b, \quad r-1 < \eta < r, \quad (1)$$

and boundary conditions

$$u^{(i)}(a) = \alpha_i, \quad u^{(i)}(b) = \beta_i. \quad (2)$$

The study of fractional calculus has led to the development of various methods for solving fractional differential equations (FDEs) of the form  $\mathcal{D}^\eta u(x) = f(x)$ , where  $\eta$  is the fractional order of the derivative,  $u(x)$  and  $f(x)$  are continuous functions, and  $\mathcal{D}^\eta$  denotes the fractional derivative operator. Many of these methods aim to find the most accurate approximation for the solution. For instance, Jajarmi et al. [18] developed a new iterative method to solve a class of non-linear fractional boundary value problems (BVPs), while Patnaik et al. [19] provided a fractional order nonlocal continuum model of an Euler-Bernoulli beam along with its analytic form and finite element solution. Isah et al. [20] suggested using a novel operational approach based on Genocchi polynomials to numerically solve nonlinear FDEs, while El-Gamel et al. [21] solved the Bagley-Torvik equation using Legendre basis functions. Abd-Elhameed et al. [23] created sixth-order Chebyshev polynomials for numerically solving linear and nonlinear forms of fractional order differential equations, and Zaky [24] created and examined a singularity-preserving spectral-collocation approach for the numerical solution of nonlinear tempered fractional differential equations. Chuanli Wang et al. [25] provided a Legendre spectral collocation method for Caputo fractional boundary value problems, while Ismail et al. [26] proposed a numerical technique using the Green function, which combines cosine and sine functions, to solve linear and nonlinear FDEs. Akguel and Yalcin [27] solved problems involving fourth-order fractional boundary values using the reproducing kernel Hilbert space approach, and Li et al. [28] provided a new reproducing kernel collocation technique for solving nonlocal fractional boundary value problems with nonsmooth solutions. Rehman et al. [29, 30] presented a numerical method based on the operational matrices of integration of the Haar wavelet to solve linear two-point and multi-point boundary value problems for FDEs, while Saeed et al. [31] used the Haar wavelet-quasilinearization approach to solve the nonlinear heat transfer equation. Pedas et al. [32, 33] presented spline and piecewise polynomial collocation techniques for numerical solutions of a class of boundary value problems for nonlinear Caputo fractional differential equations, respectively. Finally, Ur Rehman et al. [34] solved FDEs using Legendre wavelets and developed an operational matrix of fractional order integration to convert them into a system of algebraic equations. These methods contribute to the development of effective and efficient techniques for solving FDEs, which have significant applications in science and engineering.

The paper aims to investigate the solution of FDEs using the collocation technique accompanied by Genocchi polynomials. This technique offers several advantages and disadvantages that need to be considered when applying it. Firstly, one advantageous aspect of using the Genocchi collocation method is its simplicity and ease of implementation in selecting collocation points within the specified domain to approximate the solution of the model. Additionally, the flexibility of the proposed method in handling different forms of boundary conditions makes it suitable for simulating physical models with complex behavior. Furthermore, this method often leads to sparse linear systems, which can be efficiently solved using numerical techniques, thus reducing computational costs and improving efficiency. However, the choice of collocation points plays a crucial role in obtaining accurate results. Moreover, the method may encounter difficulties when dealing with problems involving irregular or complex geometries. To the best of the authors' knowledge, this is the first time FDEs have been solved using the Genocchi collocation technique. The novelty of the paper lies in the following points:

- A new design of a novel collocation approach based on Genocchi polynomials for simulating the model.

- The proposed algorithm is implemented to solve both linear and nonlinear fractional models of different complexities.
- An error analysis for the proposed algorithm is conducted to determine the error bound and estimate the residual error.
- The effectiveness of the method in solving these models suggests its potential application to other similar models.
- The proposed results obtained from the Genocchi collocation scheme are compared for each variant to verify the accuracy of the newly designed system.

The organization of the paper is as follows: In [Section 2](#), some basic properties and definitions of fractional calculus are illustrated. [Section 3](#) provides the properties of Genocchi polynomials, which are used in the subsequent sections to simulate the general model. [Section 4](#) introduces a new approach to illustrate the main steps for solving the main model. [Section 5](#) is devoted to investigating the error bound and residual error function of the proposed method through theorems. In [Section 6](#), multiple examples are simulated to demonstrate the efficiency of our technique. The conclusion for the work is given in [Section 7](#).

## 2 Basic definitions

In this section, we will introduce some important definitions using later in next sections for solving fractional boundary value problems, starting by the following definitions.

**Definition 1** [3] *The Riemann-Liouville fractional integral of order  $\eta$  of  $f(t)$  is given by*

$$I^\eta f(t) = \frac{1}{\Gamma(\eta)} \int_0^t (t-\tau)^{\eta-1} f(\tau) d\tau, \quad t > 0, \eta \in \mathbb{R}^+, \quad (3)$$

where  $\Gamma(\eta)$  is the well known gamma function.

**Definition 2** [3] *The Riemann Liouville fractional derivative of order  $\eta > 0$  is defined by*

$$\mathcal{D}_t^\eta f(t) = \left( \frac{d}{dt} \right)^m I^{m-\eta} f(t), \quad (\eta > 0, m-1 < \eta < m).$$

Some properties of  $I^\eta$  are as following:

$$I^\eta I^\varphi f(t) = I^{\eta+\varphi} f(t), \quad \eta > 0, \varphi > 0, \quad (4)$$

$$I^\eta t^\varphi = \frac{\Gamma(\varphi+1)}{\Gamma(\eta+\varphi+1)} t^{\varphi+\eta}. \quad (5)$$

**Definition 3** [3] *The Caputo fractional derivative  $D^\eta$  of a function  $f(t)$  is defined as*

$$\mathcal{D}^\eta f(t) = \frac{1}{\Gamma(n-\eta)} \int_0^t \frac{f^{(n)}(\tau)}{(t-\tau)^{\eta-n+1}} d\tau, \quad n-1 < \eta < n, n \in \mathbb{N}. \quad (6)$$

Some properties of Caputo fractional derivatives are as follows:

$$D^\eta t^\varphi = \begin{cases} 0, & \varphi \in N \cup \{0\} \text{ and } \varphi < [\eta] \\ \frac{\Gamma(\varphi+1)}{\Gamma(\eta+1-\varphi)} t^{\varphi-\eta}, & \varphi \in N \cup \{0\} \text{ and } \varphi \geq [\eta] \\ & \text{or } \varphi \notin N \text{ and } \varphi > [\eta] \end{cases}, \tag{7}$$

where,  $[\eta]$  denotes the largest integer less than or equal to  $\eta$  and  $\lceil \eta \rceil$  is the smallest integer greater than or equal to  $\eta$ .

$$D^\eta C = 0, \quad C = \text{constant}. \tag{8}$$

The operator  $D^\eta$  is a linear operator, since,

$$D^\eta (Af(t) + Bg(t)) = AD^\eta f(t) + BD^\eta g(t), \tag{9}$$

where  $A$  and  $B$  are constants. The novelty of the paper lies in the fact that the use of the Genocchi polynomials has many advantages over other similar polynomials. The Genocchi polynomials have the advantage of providing accurate results with high accuracy of less basis. In addition, the computational cost of finding an accurate solution is less than the other methods in the literature.

### 3 Fundamental relations

In this section, we will illustrate the basic concepts of Genocchi polynomials and Genocchi operational matrix for integer and fractional derivatives that will be needed in later sections for solving this type of equation.

#### Genocchi polynomials and their properties

In this subsection, we will illustrate the basic concepts of Genocchi polynomials. The generating function of the Genocchi polynomials can take the following form [35–37]:

$$Q(x, t) = \frac{2te^{xt}}{e^t + 1} = \sum_{n=0}^{\infty} G_n(x) \frac{t^n}{n!}, \quad (|t| < \pi), \tag{10}$$

where  $G_n(x)$  is the Genocchi polynomials of degree  $n$  and are defined on interval  $[0, 1]$  as

$$G_n(x) = \sum_{k=0}^n \binom{n}{k} G_k x^{n-k}, \tag{11}$$

where  $G_k$  is the Genocchi numbers and are defined by the generating function

$$Q(t) = \frac{2t}{e^t + 1} = \sum_{n=0}^{\infty} G_n \frac{t^n}{n!}, \quad (|t| < \pi). \tag{12}$$

The first few Genocchi polynomials can be found in the form

$$\begin{aligned} G_1(x) &= 1, \\ G_2(x) &= 2x - 1, \\ G_3(x) &= 3x^2 - 3x, \end{aligned}$$

$$\begin{aligned}G_4(x) &= 4x^3 - 6x^2 + 1, \\G_5(x) &= 5x^4 - 10x^3 + 5x.\end{aligned}$$

These polynomials have many interesting properties and one of these important properties is the differential property. By differentiating both sides of Eq. (11) with respect to  $x$ , we get the following:

$$\frac{dG_n(x)}{dx} = nG_{n-1}(x), \quad n \geq 1. \quad (13)$$

If we differentiate Eq. (11)  $k$  times, then we have

$$\frac{d^k G_n(x)}{dx^k} = \begin{cases} 0, & n \leq k \\ k! \binom{n}{k} G_{n-k}(x), & n > k \end{cases} \quad k, n \in N \cup \{0\}, \quad (14)$$

$$G_n(1) + G_n(0) = 0, \quad n > 1. \quad (15)$$

In the next two subsections, we introduce the differentiation matrices for both integer and fractional derivatives of boundary value problems.

### Genocchi operational matrix of integer derivative

First, we express the approximate solution in Eq. (11) in the following form

$$u_N(x) = \sum_{n=1}^N c_n G_n(x) = \mathbf{G}(x)\mathbf{C}, \quad (16)$$

where  $\mathbf{C}$  are the unknown Genocchi coefficients and  $G(x)$  are the Genocchi polynomials of the first kind, then they are given by

$$\mathbf{C}^t = [c_1 \quad c_2 \quad \dots \quad c_N], \quad \mathbf{G}(x) = [G_1(x) \quad G_2(x) \quad \dots \quad G_N(x)].$$

The  $k$ th derivative of  $u_N(x)$  can be expressed by

$$u_N^{(k)}(x) = \sum_{n=1}^N c_n G_n^{(k)}(x) = \mathbf{G}(x)\mathbf{M}^k \mathbf{C}, \quad k = 1, 2, \dots \quad (17)$$

where  $\mathbf{M}$  is  $N \times N$  operational matrix of derivative, and is given by

$$\mathbf{M} = \begin{bmatrix} 0 & 2 & 0 & \dots & 0 \\ 0 & 0 & 3 & \dots & 0 \\ \vdots & \vdots & \vdots & \dots & \vdots \\ 0 & 0 & 0 & \dots & N \\ 0 & 0 & 0 & \dots & 0 \end{bmatrix}.$$

### Genocchi operational matrix of fractional derivative

We can find the fractional derivative of Genocchi polynomials in Eq. (11) from the following theorem.

**Theorem 1** [20] Let  $\mathbf{G}(x) = [G_1(x) \ G_2(x) \ \dots \ G_N(x)]$  is the Genocchi vector and  $\eta > 0$ . Then the fractional derivative for any Genocchi polynomial can be found from

$$D^\eta G_i(x) = \sum_{k=1}^i \frac{i!G_{i-k}}{(i-k)!k!} D^\eta x^k = \sum_{k=\lceil \eta \rceil}^i \frac{i!G_{i-k}}{(i-k)!\Gamma(k+1-\eta)} x^{k-\eta}, \tag{18}$$

where

$$D^\eta G_i(x) = 0, \quad i \leq \lceil \eta \rceil,$$

and the matrix form of the fractional derivative will be in the form

$$\mathbf{H}(x) = \begin{bmatrix} 0 & 0 & \dots & H_{\lceil \eta \rceil+1}(x) & \dots & H_N(x) \end{bmatrix}. \tag{19}$$

### 4 Method of solution

In this section, we solve the fractional differential boundary value problems with linear and nonlinear forms using Genocchi collocation method. First we approximate  $u(x)$  as following

$$u_N(x) = \sum_{n=1}^N c_n G_n(x) = \mathbf{G}(x)\mathbf{C}, \tag{20}$$

and approximate the fractional derivative from Eq. (20) as

$$u_N^{(\eta)}(x) = \sum_{n=1}^N c_n G_n^{(\eta)}(x) = \mathbf{H}(x)\mathbf{C}. \tag{21}$$

#### Linear case

First, let  $\mu(x, u(x)) = f(x)$  in Eq. (1), then

$$u^{(\eta)}(x) = \sum_{m=0}^r \sigma_m u^{(m)}(x) + f(x), \quad 0 < x < 1, \quad r-1 < \eta < r, \tag{22}$$

after substituting equations (20), (21), and (17) in Eq. (22), we reach the following theorem.

**Theorem 2** If the assumed approximate solution of the fractional problem (22), and (2) are (20), (17), and (21), then the discrete Genocchi system for calculating the unknown coefficients is given by

$$\sum_{n=1}^N c_n H_n(x_i) = \sum_{m=0}^r \sum_{n=1}^N \sigma_m c_n G_n^{(m)}(x_i) + f(x_i). \tag{23}$$

**Proof** By replacing each term in Eq. (22) with its approximation from equations (20), (17), and (21) and substituting collocation points given by the following equation

$$x_i = \frac{i-1}{N-1}, \quad i = 1, 2, \dots, N. \tag{24}$$

■

The matrix form of system (23) can be written by

$$\Psi \mathbf{C} = \mathbf{F}, \tag{25}$$

where

$$\Psi = \mathbf{H} - \left( \sum_{m=0}^r \sigma_m \mathbf{G} \mathbf{M}^m \right), \tag{26}$$

and

$$\sigma_m = \begin{bmatrix} \sigma_m & 0 & \dots & 0 \\ 0 & \sigma_m & \dots & 0 \\ \vdots & \vdots & \ddots & \vdots \\ 0 & 0 & \dots & \sigma_m \end{bmatrix}, \quad \mathbf{F} = \begin{bmatrix} f(x_1) \\ f(x_2) \\ \vdots \\ f(x_N) \end{bmatrix},$$

$$\mathbf{H} = \begin{bmatrix} 0 & 0 & \dots & H_{[\eta]+1}(x_1) & \dots & H_N(x_1) \\ 0 & 0 & \dots & H_{[\eta]+1}(x_2) & \dots & H_N(x_2) \\ \vdots & \vdots & \dots & \vdots & \dots & \vdots \\ 0 & 0 & \dots & H_{[\eta]+1}(x_N) & \dots & H_N(x_N) \end{bmatrix}.$$

The matrix forms of boundary conditions are given by

$$\mathbf{G}(0) \mathbf{M}^i \mathbf{C} = [\alpha_i], \quad \mathbf{G}(1) \mathbf{M}^i \mathbf{C} = [\beta_i]. \tag{27}$$

After replacing  $r$  rows of the augmented matrix with boundary conditions, then the new augmented matrix takes the form

$$\bar{\Psi} \mathbf{C} = \bar{\mathbf{F}}. \tag{28}$$

Finally, obtaining the unknown coefficients  $\mathbf{C}$  by solving the resulting  $N \times N$  system of linear algebraic equations.

In the next subsection, we will treat with nonlinear case of fractional boundary value problem.

### Nonlinear case

By replacing  $\mu(x, u(x)) = \sum_{m=1}^r \zeta_m u^m(x) + f(x)$ , we reach the nonlinear form

$$u^{(\eta)}(x) = \sum_{m=0}^r \sigma_m u^{(m)}(x) + \sum_{m=1}^r \zeta_m u^m(x) + f(x), \quad 0 < x < 1, \quad r-1 < \eta < r, \tag{29}$$

the nonlinear terms in Eq. (29) can be approximated according to the following theorem:

**Theorem 3 [38]** *The nonlinear term of the function  $u^v(x_i), i = 1, 2, \dots, N$  can be expressed as in the following matrix form*

$$\begin{aligned} \begin{bmatrix} u^m(x_1) \\ u^m(x_2) \\ \vdots \\ u^m(x_N) \end{bmatrix} &= \begin{bmatrix} u(x_1) & 0 & \dots & 0 \\ 0 & u(x_2) & \dots & 0 \\ \vdots & \vdots & \ddots & \vdots \\ 0 & 0 & \dots & u(x_N) \end{bmatrix}^{m-1} \begin{bmatrix} u(x_1) \\ u(x_2) \\ \vdots \\ u(x_N) \end{bmatrix} \\ &= (\bar{\mathbf{U}})^{m-1} \mathbf{u} \\ &= (\bar{\mathbf{G}}\bar{\mathbf{C}})^{m-1} \mathbf{G}\mathbf{C}, \end{aligned} \tag{30}$$

where

$$\bar{\mathbf{G}} = \begin{bmatrix} \mathbf{G}(x_1) & 0 & \dots & 0 \\ 0 & \mathbf{G}(x_2) & \dots & 0 \\ \vdots & \vdots & \ddots & \vdots \\ 0 & 0 & \dots & \mathbf{G}(x_N) \end{bmatrix}, \quad \bar{\mathbf{C}} = \begin{bmatrix} \mathbf{C} & 0 & \dots & 0 \\ 0 & \mathbf{C} & \dots & 0 \\ \vdots & \vdots & \ddots & \vdots \\ 0 & 0 & \dots & \mathbf{C} \end{bmatrix}.$$

After substituting equations (20), (21), and (17) in Eq. (29), we reach the following theorem:

**Theorem 4** *If the assumed approximate solution of the fractional problem (29), and (2) are (20), (17), and (21), then the discrete Genocchi system for calculating the unknown coefficients is given by*

$$\sum_{n=1}^N c_n H_n(x_i) = \sum_{m=0}^r \sum_{n=1}^N \sigma_m c_n G_n^{(m)}(x_i) + \sum_{m=1}^r \sum_{n=1}^N \zeta_m c_n G_n^m(x_i) + f(x_i). \tag{31}$$

**Proof** We begin by replacing each term in Eq. (29) with its approximation from equations (20), (17), and (21). Then, by substituting collocation points given by Eq. (24) into this system, we get the following matrix form:

$$\Psi \mathbf{C} = \mathbf{F}, \tag{32}$$

where

$$\Psi = \mathbf{H} - \left( \sum_{m=0}^r \sigma_m \mathbf{G}\mathbf{M}^m - \sum_{m=1}^r \zeta_m (\bar{\mathbf{G}}\bar{\mathbf{C}})^{m-1} \mathbf{G} \right), \tag{33}$$

and

$$\zeta_m = \begin{bmatrix} \zeta_m & 0 & \dots & 0 \\ 0 & \zeta_m & \dots & 0 \\ \vdots & \vdots & \ddots & \vdots \\ 0 & 0 & \dots & \zeta_m \end{bmatrix},$$

after replacing  $r$  rows of augmented matrix with boundary conditions matrices from Eq. (27), then the new augmented matrix take the form

$$\bar{\Psi}C = \bar{F}. \tag{34}$$

Finally, obtaining the unknown coefficients  $C$  by solving the resulting  $N \times N$  system of nonlinear algebraic equations by using the following algorithm:

**Algorithm**

- input (integer)  $N$ .
- input (double)  $\text{tol}$ .
- input (array)  $C_{old} = C_0$ , (initial approximation,  $C_0$  with  $N$  dimension, can be chosen so that the boundary conditions are satisfied.)
- $\bar{\Psi}(C_{old}).C_{new} = \bar{F}$  is a linear algebraic equation system. This system is solved and  $C_{new}$  is found.
- If  $|C_{old} - C_{new}| < \text{tol}$  then  $C_{new} = C$ . break (the program is finished).
- Else then  $C_{old} \leftarrow C_{new}$ .
- Go to the second stage. ■

## 5 Error bound

### Error bound estimate

In this subsection, we will provide the error bound for the obtained solution of model 1. We provide the error bound for a special case of the model where the value of  $\mu(x, u(x)) = g(x)$ . Suppose that  $g(x) \in C^{n+1}[0, 1]$  and the space  $\Xi = \text{Span}\{G_1(x), G_2(x), \dots, G_N(x)\}$ . Next, if the best approximation of  $g(x)$  can be in the form  $C^T G(x)$ , then we reach the following theorem:

**Theorem 5** Suppose that  $g(x) \in C^{n+1}[0, 1]$  and define  $\Xi = \text{Span}\{G_1(x), G_2(x), \dots, G_N(x)\}$  where  $C^T G(x)$  is the best approximation of the function  $g(x)$  out of  $\Xi$ , then we have

$$\|g(x) - C^T G(x)\| \leq \frac{\mathfrak{J}^{\frac{2m+3}{2}} \mathfrak{R}}{(m+1)! \sqrt{2m+3}}, \quad x \in [x_i, x_{i+1}] \subseteq [0, 1],$$

where  $\mathfrak{R} = \max_{x \in [x_i, x_{i+1}]} |g^{(m+1)}(x)|$  and  $\mathfrak{J} = x_{i+1} - x_i$ .

**Proof** To prove this theorem. We first expand the function  $u(x)$  in the following Taylor expansion form

$$u_1(x) = g(x_i) + g'(x_i)(x - x_i) + g''(x_i) \frac{(x - x_i)^2}{2!} + \dots + g^{(n)}(x_i) \frac{(x - x_i)^n}{n!}. \tag{35}$$

Then, for the previous form of Taylor expansion, if we apply the modulus for both sides of Eq. (35), we can deduce in the following compact form

$$|g(x) - u_1(x)| \leq |g^{(n+1)}(\mathfrak{N}_x)| \frac{(x - x_i)^{n+1}}{(n+1)!},$$

where

$$\mathfrak{N}_x \in [x_i, x_{i+1}].$$

With the assumption that  $\mathbf{C}^T \mathbf{G}(t)$  is the best approximation of the function  $g(x)$  out of the space  $\Xi$  and that  $u_1(t) \in \Xi$ , then we have

$$\begin{aligned} \|g(x) - \mathbf{C}^T \mathbf{G}(x)\|_2^2 &\leq \|g(x) - u_1(x)\|_2^2 = \int_{x_i}^{x_{i+1}} |g(h) - u_1(h)|^2 dh \\ &\leq \int_{x_i}^{x_{i+1}} \|g(x)^{(m+1)}(\mathfrak{R}_x)\|^2 \frac{(h - x_i)^{m+1}}{(m + 1)!} dh \leq \frac{\mathfrak{J}^{2m+3} \mathfrak{R}^2}{((m + 1)!)^2 (2m + 3)}. \end{aligned}$$

Then, finally taking the square root for both sides, we conclude that

$$\|g(x) - \mathbf{C}^T \mathbf{G}(x)\| \leq \frac{\mathfrak{J}^{\frac{2m+3}{2}} \mathfrak{R}}{(m + 1)! \sqrt{2m + 3}}.$$

■

This theorem provides a local error bound for the proposed main equation of  $\mathcal{O}(\mathfrak{J}^{\frac{2m+3}{2}})$ .

### Residual error function

In this subsection, We can easily check the accuracy of the suggested method in terms of the residual error function. Since the truncated Genocchi series in Eq. (16) is considered as an approximate solution of Eq. (1), then by substituting the approximate solution  $u_N(x)$  and its derivatives into Eq. (1), the resulting equation must be satisfied, and when substituting the collocation points defined as

$$x = x_i \in [0, 1], \quad i = 1, 2, \dots, N,$$

the residual error function for the approximate solution can be calculated in the form

$$|\mathfrak{R}_N(x_i)| = |u^{(\eta)}(x) - \sum_{m=0}^r \sigma_m u^{(m)}(x) - \mu(x, u(x))| \cong 0, \tag{36}$$

or

$$\mathfrak{R}_N(x_i) \leq 10^{-\tau i},$$

where  $\mathfrak{R}_N(x_i)$  are the residual error function defined at the collocation points  $x_i$  and  $\tau i$  is any positive integer. If  $\max 10^{\tau i} = 10^\tau$  ( $\tau$  is any positive integer) can be prescribed which can be considered as the tolerance for the obtained error, then the value of the number of iterations  $N$  is increased until the residual error  $\mathfrak{R}_N(x_i)$  at each of the points become smaller than the prescribed tolerance  $10^\tau$  which shall prove that the method converge to the desired solution as the residual error approaches zero. Also, we can calculate the error function at each of the collocation points to prove the efficiency of the proposed technique which can be described as

$$\mathfrak{R}_N(x_i) = u^{(\eta)}(x) - \sum_{m=0}^r \sigma_m u^{(m)}(x) - \mu(x, u(x)).$$

Then, if  $u_N(x) \rightarrow 0$ , as  $N$  has sufficiently enough value, then the residual error decreases and this proves that the proposed method converges correctly.

## 6 Numerical simulation

In this section, we present 7 examples [20, 21, 25, 33, 34, 39, 40] for linear and nonlinear forms of fractional problems using Genocchi collocation method. The error measurements for verifying the results in the later examples can be used in the following form

$$\mathbf{e}_N(x) = |(u(x) - u_N(x))|,$$

and the maximum absolute error is given by

$$\|\mathbf{e}_N(x)\|_\infty = \max \|u(x) - u_N(x)\|.$$

In addition, the  $L_2$  norm can be defined in the following form:

$$\|\mathbf{e}_N(x)\|_2 = \sqrt{\frac{1}{N} \sum_{i=1}^N (\mathbf{e}_N(x))^2}.$$

**Example 1** [21] Consider the following linear fractional BVP

$$u'' + u^{(3/2)} + u = x + 1, \quad 0 < x < 1,$$

with boundary conditions

$$u(0) = 1, \quad u(1) = 2,$$

and exact solution  $u = x + 1$ . We provide the details for obtaining the approximate solution for  $N = 6$  as follows, let the approximate solution in the form

$$u(x) = c_1 G_1(x) + c_2 G_2(x) + \dots + c_6 G_6(x),$$

then

$$M^2 = \begin{bmatrix} 0 & 0 & 6 & 0 & 0 & 0 \\ 0 & 0 & 0 & 12 & 0 & 0 \\ 0 & 0 & 0 & 0 & 20 & 0 \\ 0 & 0 & 0 & 0 & 0 & 30 \\ 0 & 0 & 0 & 0 & 0 & 0 \\ 0 & 0 & 0 & 0 & 0 & 0 \end{bmatrix}.$$

Using collocation points  $x_i = \frac{i-1}{5}$ ,  $i = 1, 2, \dots, 6$ , then we have

$$G = \begin{bmatrix} 1 & -1 & 0 & 1 & 0 & -3 \\ 1 & -0.6 & -0.48 & 0.792 & 0.928 & -2.42208 \\ 1 & -0.2 & -0.72 & 0.296 & 1.488 & -0.92256 \\ 1 & 0.2 & -0.72 & -0.296 & 1.488 & 0.92256 \\ 1 & 0.6 & -0.48 & -0.792 & 0.928 & 2.42208 \\ 1 & 1 & 0 & -1 & 0 & 3 \end{bmatrix}_{(6 \times 6)},$$

$$H = \begin{bmatrix} 0 & 0 & 0 & 0 & 0 & 0 \\ 0 & 0 & 3.02776 & -4.44071 & -3.39109 & 13.42249 \\ 0 & 0 & 4.28190 & -3.99644 & -7.76451 & 12.95335 \\ 0 & 0 & 5.24423 & -2.09770 & -10.90800 & 6.37099 \\ 0 & 0 & 6.05552 & 0.80740 & -11.62659 & -3.38417 \\ 0 & 0 & 6.77027 & 4.51352 & -9.02703 & -12.57337 \end{bmatrix}_{(6 \times 6)},$$

and the augmented matrix becomes as

$$[\Psi, F] = \begin{bmatrix} 1 & -1 & 6 & -11 & 0 & 27 & , & 1 \\ 1 & -0.6 & 8.54776 & -10.84871 & -12.06309 & 34.76041 & , & 1.2 \\ 1 & -0.2 & 9.56190 & -6.10044 & -20.67651 & 20.91079 & , & 1.4 \\ 1 & 0.2 & 10.52423 & 0.00631 & -23.82000 & -1.58645 & , & 1.6 \\ 1 & 0.6 & 11.57552 & 7.21540 & -20.29860 & -24.72209 & , & 1.8 \\ 1 & 1 & 12.77028 & 15.51352 & -9.02703 & -39.573377 & , & 2 \end{bmatrix}.$$

Next, the augmented matrix for the boundary conditions according to Eq. (27) can take the forms

$$[\psi_1, \alpha_0] = [1 \quad -1 \quad 0 \quad 1 \quad 0 \quad -3 \quad , \quad 1],$$

$$[\psi_2, \beta_0] = [1 \quad 1 \quad 0 \quad -1 \quad 0 \quad 3 \quad , \quad 2].$$

Replacing the first and last rows with the previous representation of the boundary conditions, the new augmented matrix takes the form

$$[\bar{\Psi}, \bar{F}] = \begin{bmatrix} 1 & -1 & 0 & 1 & 0 & -3 & , & 1 \\ 1 & -0.6 & 8.54776 & -10.84871 & -12.06309 & 34.76041 & , & 1.2 \\ 1 & -0.2 & 9.56190 & -6.10044 & -20.67651 & 20.91079 & , & 1.4 \\ 1 & 0.2 & 10.52423 & 0.00631 & -23.82000 & -1.58645 & , & 1.6 \\ 1 & 0.6 & 11.57552 & 7.21540 & -20.29860 & -24.72209 & , & 1.8 \\ 1 & 1 & 0 & -1 & 0 & 3 & , & 2 \end{bmatrix}.$$

Then, by solving the above linear system the Genocchi coefficients can be found as

$$C = \begin{bmatrix} 1.5000 \\ 0.5000 \\ -3.1258E - 17 \\ -2.6724E - 16 \\ -1.3235E - 17 \\ -8.2262E - 17 \end{bmatrix},$$

and the approximate solution is

$$u_6(x) = 1 + x + 0.2757E - 15x^2 - 0.9366E - 15x^3 + 0.1168E - 14x^4 - 0.4936E - 15x^5.$$

By using Genocchi collocation method for solving this form of fractional boundary value problem at  $N = 6$  having the exact solution  $u = x + 1$ , we reach that the approximate solution is equal to the exact solution with running time 5.079 seconds. For  $N = 14$  the absolute error and the residual error are represented in

**Table 1.** From this table, it can be noted that the method provides accurate results using a few numbers of Genocchi bases. In addition, a comparison between exact and approximate solutions is presented in [Figure 1](#).

**Table 1.** Absolute and residual error for [Example 1](#) at  $N = 14$ .

x	$ e_N(x) $	$ \mathcal{R}_N $
0.0	1.5543E-15	9.1807E-15
0.1	1.3323E-15	9.6109E-16
0.2	8.8818E-16	5.0143E-16
0.3	4.4409E-16	3.0309E-16
0.4	0.0000	3.1559E-16
0.5	2.2204E-16	1.4750E-16
0.6	4.4409E-16	1.2567E-16
0.7	8.8818E-16	1.1833E-16
0.8	1.1102E-15	6.3519E-17
0.9	1.5543E-15	1.3599E-16
1.0	1.7764E-15	1.6221E-15

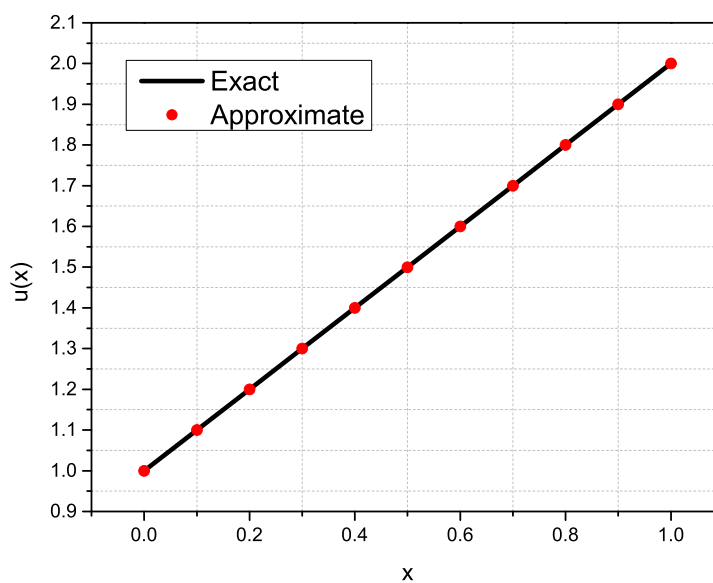


**Figure 1.** Comparison between exact and Genocchi solution for [Example 1](#).

**Example 2** [21, 22] Consider the linear fractional IVP taken the form

$$u'' + u^{(3/2)} + u = 7x + \frac{8}{\sqrt{\pi}}x^{3/2} + x^3 + 1, \quad 0 < x < 1,$$

with initial conditions

$$u(0) = 1, \quad u'(0) = 1,$$

and exact solution

$$u = x^3 + x + 1.$$

Comparing the approximate solution obtained by Genocchi collocation method and shifted Legendre collocation method [21] at  $N = 15$  with the exact solution in Table 2 and the Genocchi solution and shifted Legendre solution are represented in Figure 3. The absolute error for Genocchi solution when  $N = 15$  is appearing in Table 3 and compared to the results reported by using the Lucas Wavelet Scheme in [22]. Based on these results, it can be seen that the proposed method provides better accuracy. In addition, it can be noticed from Figure 2, which appears the exact and Genocchi approximate solution that our method is very accurate.

**Table 2.** Exact and approximate solution for Example 2.

x	Exact	Approximate	Shifted Legendre [21]
0.10	1.101000	1.101000	1.101000
0.25	1.265625	1.265625	1.265625
0.50	1.625000	1.625000	1.625000
0.75	2.171875	2.171875	2.171875
1.0	3.000000	3.000000	3.000002

**Table 3.** Absolute error for Example 2.

x	$ e_N(x) $	Lucas Wavelet [22]
0.0	2.2204E-16	×
0.1	4.4409E-16	1.99E-15
0.2	4.4409E-16	×
0.3	6.6613E-16	×
0.4	6.6613E-16	×
0.5	6.6613E-16	4.90E-14
0.6	6.6613E-16	×
0.7	4.4409E-16	×
0.8	0.0000	×
0.9	0.0000	×
1.0	4.4409E-16	1.96E-13

**Example 3** [39] Consider another form of linear fractional IVP

$$u^{(\eta)} + u = (x^2 + 2x^{2-\eta} / \Gamma(3 - \eta)) + (x^3 + 6x^{3-\eta} / \Gamma(4 - \eta)), \quad 0 < x < 1,$$

with initial condition

$$u(0) = 0,$$

the exact solution

$$u = x^3 + x^2.$$

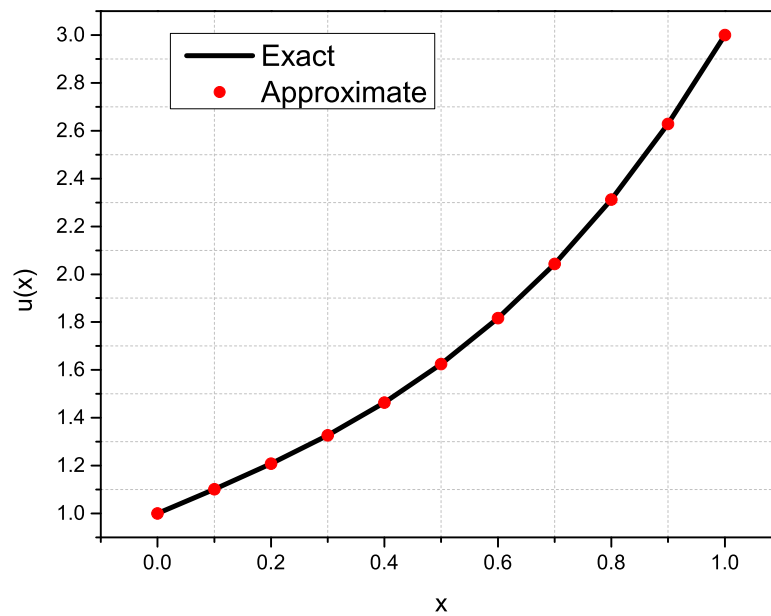


**Figure 2.** Comparison between exact and Genocchi solution for [Example 2](#).

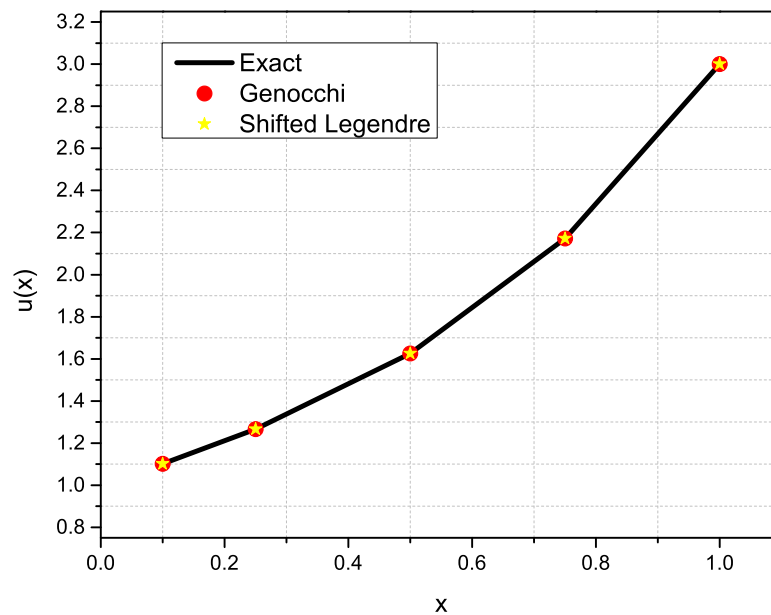


**Figure 3.** Comparison between Genocchi solution and Shifted Legendre for [Example 2](#).

Taking the value of  $\eta = 1/2$ , we reach the absolute error for  $N = 6$  using Genocchi collocation method tabulated in [Table 4](#). In addition, the running time for simulating the results is found to be 5.651 seconds with an error norm of  $\|e_6(x)\|_2 = 3.0978E - 15$ . The value of the acquired norm reveals the ability of the method to provide accurate solutions. In addition, the behavior of exact and approximate Genocchi solution is in [Figure 4](#).

**Table 4.** Absolute error for **Example 3.**

x	$ e_N(x) $
0.0	1.8111E-15
0.1	1.9082E-16
0.2	1.5127E-15
0.3	2.9143E-15
0.4	3.8580E-15
0.5	4.3299E-15
0.6	4.4409E-15
0.7	4.2188E-15
0.8	3.7748E-15
0.9	2.8866E-15
1.0	1.7764E-15

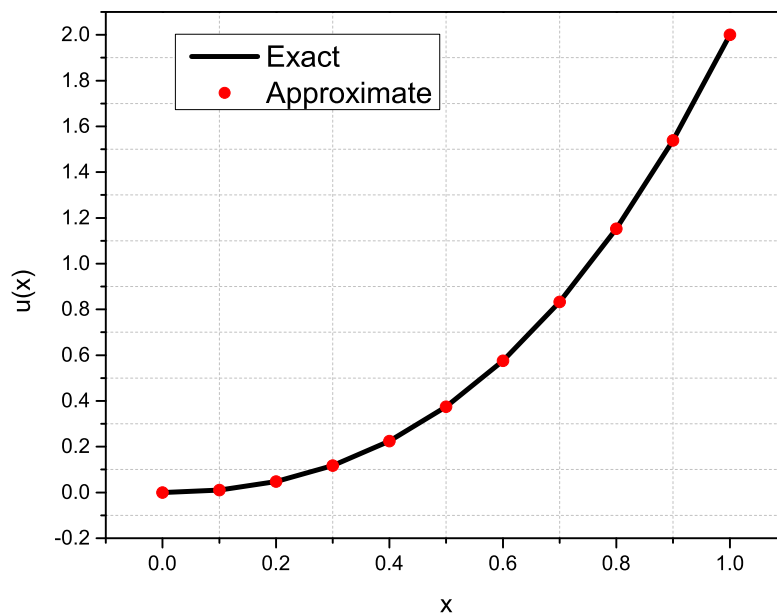


**Figure 4.** Comparison between exact and Genocchi solution for **Example 3.**

**Example 4** [20] Consider the following nonlinear fractional BVP

$$u'' + \Gamma\left(\frac{4}{5}\right)x^{\frac{6}{5}}u^{\left(\frac{6}{5}\right)} + \frac{11}{9}\Gamma\left(\frac{5}{6}\right)x^{\frac{1}{6}}u^{\left(\frac{1}{6}\right)} - (u')^2 = 2 + \frac{1}{10}x^2, \quad 0 < x < 1,$$

with boundary conditions

$$u(0) = 1, \quad u(1) = 2,$$

and exact solution

$$u = x^2 + 1.$$

Seeing from **Table 5** which represents the absolute error obtained by Genocchi collocation method for  $N = 6$  with a running time 10.912 seconds, our method is very accurate for solving this type of fractional BVPs.

Besides that comparison between exact and approximate Genocchi solution is shown in [Figure 5](#).

**Table 5.** Absolute error for [Example 4](#).

x	$ e_N(x) $
0.0	0.0000
0.1	3.1752E-14
0.2	5.6177E-14
0.3	6.6391E-14
0.4	4.5519E-14
0.5	1.9762E-14
0.6	1.3101E-13
0.7	2.6557E-13
0.8	3.6660E-13
0.9	3.3085E-13
1.0	0.0000

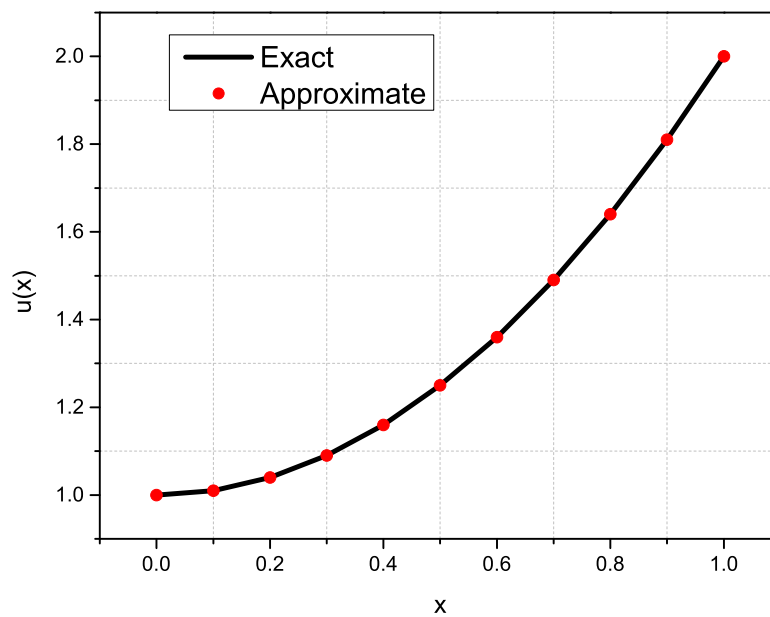


**Figure 5.** Comparison between exact and Genocchi solution for [Example 4](#).

**Example 5** [33] Consider the following nonlinear fractional BVP

$$u^{(\frac{3}{2})} - u^3 = \frac{\Gamma(2.9)}{\Gamma(1.4)} x^{0.4} - (x^{1.9} - 1)^3,$$

with boundary conditions

$$u(0) = -1, \quad u(1) = 0,$$

the exact solution is

$$u = x^{1.9} - 1.$$

Representing the absolute error obtained by Genocchi collocation method with  $N = 10$  in Table 6 and the comparison between maximum absolute error obtained by Genocchi collocation method and spline collocation method [33] for different values of  $N$  in Table 7. In addition, the exact and approximate Genocchi solutions are shown in Figure 6.

**Table 6.** Absolute error for Example 5.

x	$ e_N(x) $
0.0	6.6613E-16
0.1	2.3761E-4
0.2	2.9613E-4
0.3	3.0385E-4
0.4	2.9104E-4
0.5	2.6203E-4
0.6	2.1928E-4
0.7	1.6267E-4
0.8	9.4943E-5
0.9	1.2709E-5
1.0	6.3838E-16

**Table 7.** Comparison between maximum absolute error for Example 5.

N	$\ e_N(x)\ $	Spline collocation [33]
4	1.8688E-03	1.24E-3
8	4.6148E-04	3.57E-4

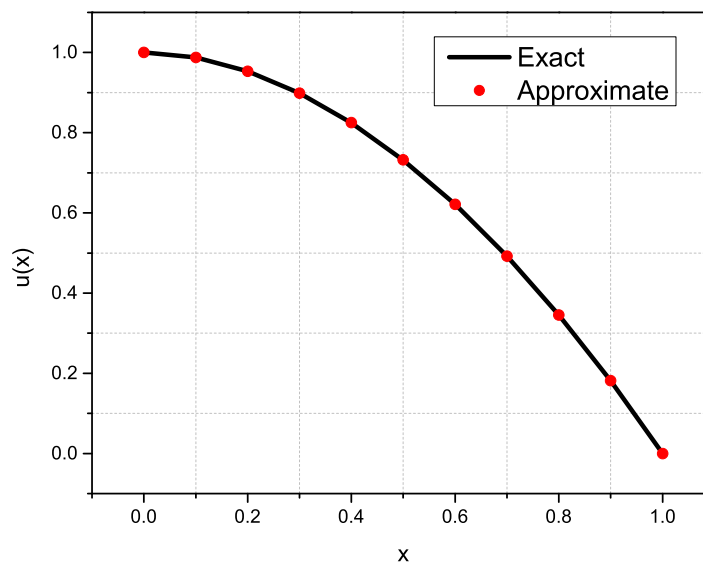


**Figure 6.** Comparison of exact and Genocchi solutions at  $\eta = 3/2$  for Example 5.

**Example 6** [40] Consider the following nonlinear fractional BVP

$$u^{(\frac{3}{2})} + e^{-2\pi}u^2 = \frac{105\sqrt{\pi}}{32}x^2 + e^{-2\pi}x^7, \quad 0 < x < 1,$$

with boundary conditions

$$u(0) = 0, \quad u(1) = 1,$$

the exact solution

$$u = x^{7/2}.$$

**Table 8** represents the comparison between the absolute error obtained by Genocchi collocation method  $N = 10$ , and Legendre wavelet method [34]. In addition, it is found that the error measure of the  $\|e_6(x)\|_2 = 8.0268E - 06$  and the behavior of exact and approximate solutions is graphed in **Figure 7**.

**Table 8.** Comparison of absolute error for **Example 6**.

x	$ e_N(x) $	Legendre wavelet [34]
0.0	5.7246E-17	x
0.1	1.0507E-5	9.6996E-5
0.2	1.3141E-5	9.3927E-4
0.3	1.2742E-5	1.5087E-3
0.4	1.1182E-5	3.3989E-4
0.5	8.7996E-6	2.4163E-3
0.6	5.9264E-6	3.1023E-4
0.7	2.5945E-6	1.4799E-3
0.8	9.2167E-7	6.3407E-4
0.9	5.2079E-6	4.6701E-3
1.0	1.1102E-16	x

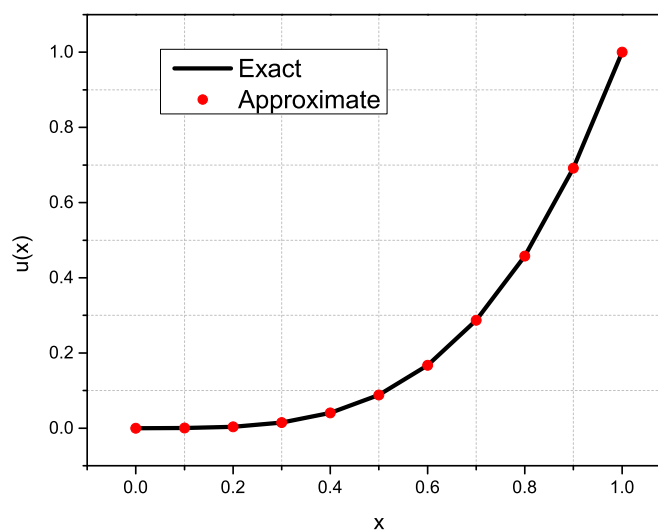


**Figure 7.** Comparison between exact and Genocchi solution at  $\eta = 3/2$  for **Example 6**.

**Example 7** [25] Consider the following nonlinear fractional BVP

$$u^{(5/4)} - u^2 = -\frac{\Gamma(128/17)}{\Gamma(128/17 - \eta)} x^{111/17 - \eta} - (x - x^{111/17})^2, \quad 0 < x < 1,$$

with boundary condition

$$u(0) = 0, \quad u(1) = 0,$$

the exact solution

$$u = x - x^{111/17}.$$

A comparison between exact and approximate Genocchi solution is represented in [Figure 8](#), and the absolute error for  $N = 10$  obtained by Genocchi collocation method is represented in [Table 9](#).

**Table 9.** Absolute error for [Example 7](#).

x	$ e_N(x) $
0.0	1.9559E-16
0.1	1.4825E-07
0.2	3.2983E-08
0.3	1.0581E-07
0.4	2.6299E-07
0.5	4.4011E-07
0.6	6.3645E-07
0.7	8.6430E-07
0.8	1.1047E-06
0.9	1.4344E-06
1.0	1.9559E-16

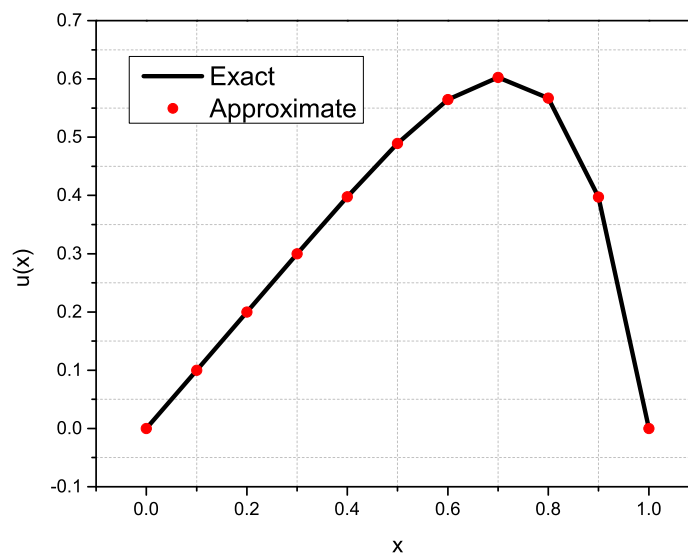


**Figure 8.** Comparison between exact and Genocchi solution at  $\eta = 5/4$  for [Example 7](#).

## 7 Conclusion

In this paper, we have examined the application of the Genocchi collocation technique for solving a general form of linear and nonlinear fractional models. The models of fractional order have great applications in science and engineering. Some basic definitions for the fractional order derivative are introduced and utilized for treating the fractional term in the main model. Then, the collocation technique is adapted for converting the model into a system of nonlinear algebraic equations which is then solved using a novel technique to find the values of the unknown coefficients, and hence, the solution is found. The error bound for the proposed technique is provided ensuring that the proposed technique has a local bound of  $\mathcal{O}(\mathcal{J}^{\frac{2m+3}{2}})$ . The accuracy of the proposed technique is tested for several examples of different forms and the results are compared to other forms the literature provides the effectiveness of the technique in providing more accurate results with less computational cost. Thus, the method proved to be an effective technique for simulating similar models and has other important applications.

### Declarations

#### List of abbreviations

Not applicable.

#### Ethical approval

The authors state that this research complies with ethical standards. This research does not involve either human participants or animals.

#### Consent for publication

Not applicable.

#### Conflicts of interest

The authors confirm that there is no competing interest in this study.

#### Data availability statement

Data availability is not applicable to this article as no new data were created or analyzed in this study.

#### Funding

Not applicable.

#### Author's contributions

M.G.: Conceptualization, Methodology, Writing - Original Draft, Writing - Review & Editing, Project administration, Supervision. N.S.: Methodology, Software, Validation, Formal analysis, Data Curation, Writing - Original Draft, Visualization. W.A.: Conceptualization, Methodology, Software, Validation, Formal analysis, Data Curation, Writing - Original Draft, Writing - Review & Editing, Supervision. All authors have read and agreed to the published version of the manuscript.

#### Acknowledgements

The authors would like to convey many thanks to the editor and anonymous reviewers for their helpful comments and suggestions, which further improved this study.

## References

- [1] Teodoro, G.S., Machado, J.T. and De Oliveira, E.C. A review of definitions of fractional derivatives and other operators. *Journal of Computational Physics*, 388, 195-208, (2019). [[CrossRef](#)]
- [2] Li, C., Qian, D. and Chen, Y.Q. On Riemann-Liouville and Caputo derivatives. *Discrete Dynamics in Nature and Society*, 2011, 562494, (2011). [[CrossRef](#)]
- [3] Kilbas, A.A., Srivastava, H.M. and Trujillo, J.J. *Theory and Applications of Fractional Differential Equations* (Vol. 204). Elsevier: Netherlands, (2006).
- [4] Podlubny, I. *Fractional Differential Equations: An Introduction to Fractional Derivatives, Fractional Differential Equations, to Methods of their Solution and Some of their Applications* (Vol. 198). Elsevier, (1999).
- [5] Agarwal, R.P., Cuevas, C. and Soto, H. Pseudo-almost periodic solutions of a class of semi-linear fractional differential equations. *Journal of Applied Mathematics and Computing*, 37(1-2), 625-634, (2011). [[CrossRef](#)]
- [6] Ur Rahman, M., Arfan, M. and Baleanu, D. Piecewise fractional analysis of the migration effect in plant-pathogen-herbivore interactions. *Bulletin of Biomathematics*, 1(1), 1-23, (2023). [[CrossRef](#)]
- [7] Kurt, A., Tasbozan, O. and Durur, H. The exact solutions of conformable fractional partial differential equations using new sub equation method. *Fundamental Journal of Mathematics and Applications*, 2(2), 173-179, (2019). [[CrossRef](#)]
- [8] Yalçın Uzun, T. Oscillatory criteria of nonlinear higher order  $\Psi$ -Hilfer fractional differential equations. *Fundamental Journal of Mathematics and Applications*, 4(2), 134-142, (2021). [[CrossRef](#)]
- [9] Atede, A.O., Omame, A. and Inyama, S.C. A fractional order vaccination model for COVID-19 incorporating environmental transmission: a case study using Nigerian data. *Bulletin of Biomathematics*, 1(1), 78-110, (2023). [[CrossRef](#)]
- [10] Anjam, Y.N., Yavuz, M., Ur Rahman, M. and Batool, A. Analysis of a fractional pollution model in a system of three interconnecting lakes. *AIMS Biophysics*, 10(2), 220-240, (2023). [[CrossRef](#)]
- [11] Işık, E. and Daşbaşı, B. A compartmental fractional-order mobbing model and the determination of its parameters. *Bulletin of Biomathematics*, 1(2), 153-176, (2023). [[CrossRef](#)]
- [12] Yavuz, M., Sulaiman, T.A., Usta, F. and Bulut, H. Analysis and numerical computations of the fractional regularized long-wave equation with damping term. *Mathematical Methods in the Applied Sciences*, 44(9), 7538-7555, (2021). [[CrossRef](#)]
- [13] Yavuz, M., Özköse, F., Susam, M. and Kalidass, M. A new modeling of fractional-order and sensitivity analysis for Hepatitis-B disease with real data. *Fractal and Fractional*, 7(2), 165, (2023). [[CrossRef](#)]
- [14] Elsonbaty, A., Alharbi, M., El-Mesady, A. and Adel, W. Dynamical analysis of a novel discrete fractional lumpy skin disease model. *Partial Differential Equations in Applied Mathematics*, 9, 100604, (2024). [[CrossRef](#)]
- [15] El-Mesady, A., Adel, W., Elsadany, A.A. and Elsonbaty, A. Stability analysis and optimal control strategies of a fractional-order monkeypox virus infection model. *Physica Scripta*, 98(9), 095256, (2023). [[CrossRef](#)]
- [16] Evirgen, F., Uçar, E., Uçar, S. and Özdemir, N. Modelling Influenza A disease dynamics under Caputo-Fabrizio fractional derivative with distinct contact rates. *Mathematical Modelling and*

*Numerical Simulation with Applications*, 3(1), 58-73, (2023). [[CrossRef](#)]

- [17] Mpungu, K. and Ma'aruf Nass, A. On complete group classification of time fractional systems evolution differential equation with a constant delay. *Fundamental Journal of Mathematics and Applications*, 6(1), 12-23, (2023). [[CrossRef](#)]
- [18] Jajarmi, A. and Baleanu, D. A new iterative method for the numerical solution of high-order non-linear fractional boundary value problems. *Frontiers in Physics*, 8, 220, (2020). [[CrossRef](#)]
- [19] Patnaik, S., Sidhardh, S. and Semperlotti, F. A Ritz-based finite element method for a fractional-order boundary value problem of nonlocal elasticity. *International Journal of Solids and Structures*, 202, 398-417, (2020). [[CrossRef](#)]
- [20] Isah, A. and Phang, C. New operational matrix of derivative for solving non-linear fractional differential equations via Genocchi polynomials, *Journal of King Saud University-Science*, 31(1), 1-7, (2019). [[CrossRef](#)]
- [21] El-Gamel, M. and El-Hady, M.A. Numerical solution of the Bagley-Torvik equation by Legendre-collocation method. *SeMA Journal*, 74, 371-383, (2017). [[CrossRef](#)]
- [22] Koundal, R., Kumar, R., Srivastava, K. and Baleanu, D. Lucas wavelet scheme for fractional Bagley–Torvik equations: Gauss–Jacobi approach. *International Journal of Applied and Computational Mathematics*, 8, 2-16, (2022). [[CrossRef](#)]
- [23] Abd-Elhameed, W.M. and Youssri, Y.H. Sixth-kind Chebyshev spectral approach for solving fractional differential equations. *International Journal of Nonlinear Sciences and Numerical Simulation*, 20(2), 191-203, (2019). [[CrossRef](#)]
- [24] Zaky, M.A. Existence, uniqueness and numerical analysis of solutions of tempered fractional boundary value problems. *Applied Numerical Mathematics*, 145, 429-457, (2019). [[CrossRef](#)]
- [25] Wang, C., Wang, Z. and Wang, L. A spectral collocation method for nonlinear fractional boundary value problems with a Caputo derivative. *Journal of Scientific Computing*, 76, 166-188, (2018). [[CrossRef](#)]
- [26] Ismail, M., Saeed, U., Alzabut, J. and Ur Rehman, M. Approximate solutions for fractional boundary value problems via Green-CAS wavelet method. *Mathematics*, 7(12), 1164, (2019). [[CrossRef](#)]
- [27] Akgül, A. and Karatas Akgül, E. A novel method for solutions of fourth-order fractional boundary value problems, *Fractal and Fractional*, 3(2), 33, (2019). [[CrossRef](#)]
- [28] Li, X. and Wu, B. A new reproducing kernel collocation method for nonlocal fractional boundary value problems with non-smooth solutions. *Applied Mathematics Letters*, 86, 194-199, (2018). [[CrossRef](#)]
- [29] Ur Rehman, M. and Khan, R.A. A numerical method for solving boundary value problems for fractional differential equations. *Applied Mathematical Modelling*, 36(3), 894-907, (2012). [[CrossRef](#)]
- [30] Youssef, I.K. and El Dewaik, M.H. Solving Poisson's equations with fractional order using Haar wavelet. *Applied Mathematics and Nonlinear Sciences*, 2(1), 271-284, (2017). [[CrossRef](#)]
- [31] Saeed, U. and Ur Rehman, M. Assessment of Haar wavelet-quasilinearization technique in heat convection-radiation equations. *Applied Computational Intelligence and Soft Computing*, 2014, 1–5, (2014). [[CrossRef](#)]
- [32] Pedas, A. and Tamme, E. Piecewise polynomial collocation for linear boundary value problems of fractional differential equations. *Journal of Computational and Applied Mathematics*,

- 236(13), 3349-3359, (2012). [[CrossRef](#)]
- [33] Pedas, A. and Tamme, E. Spline collocation for nonlinear fractional boundary value problems. *Applied Mathematics and Computation*, 244, 502-513, (2014). [[CrossRef](#)]
- [34] Ur Rehman, M. and Khan, R.A. The Legendre wavelet method for solving fractional differential equations. *Communications in Nonlinear Science and Numerical Simulation*, 16(11), 4163–4173, (2011). [[CrossRef](#)]
- [35] Araci, S. Novel identities for q-Genocchi numbers and polynomials. *Journal of Function Spaces and Applications*, 2012, 214961, (2012). [[CrossRef](#)]
- [36] Ozden, H., Simsek, Y. and Srivastava, H.M. A unified presentation of the generating functions of the generalized Bernoulli, Euler and Genocchi polynomials. *Computers & Mathematics with Applications*, 60(10), 2779–2787, (2010). [[CrossRef](#)]
- [37] Isah, A. and Phang, C. Operational matrix based on Genocchi polynomials for solution of delay differential equations. *Ain Shams Engineering Journal*, 9(4), 2123–2128, (2018). [[CrossRef](#)]
- [38] El-Gamel, M., Mohamed, N. and Adel, W. Numerical study of a nonlinear high order boundary value problems using Genocchi collocation technique. *International Journal of Applied and Computational Mathematics*, 8, 143, (2022). [[CrossRef](#)]
- [39] Li, Z., Yan, Y. and Ford, N.J. Error estimates of a high order numerical method for solving linear fractional differential equations. *Applied Numerical Mathematics*, 114, 201–220, (2017). [[CrossRef](#)]
- [40] Al-Mdallal, Q.M. and Hajji, M.A. A convergent algorithm for solving higher-order nonlinear fractional boundary value problems. *Fractional Calculus and Applied Analysis*, 18(6), 1423–1440, (2015). [[CrossRef](#)]

Mathematical Modelling and Numerical Simulation with Applications (MMNSA)  
(<https://dergipark.org.tr/en/pub/mmnsa>)



**Copyright:** © 2023 by the authors. This work is licensed under a Creative Commons Attribution 4.0 (CC BY) International License. The authors retain ownership of the copyright for their article, but they allow anyone to download, reuse, reprint, modify, distribute, and/or copy articles in MMNSA, so long as the original authors and source are credited. To see the complete license contents, please visit (<http://creativecommons.org/licenses/by/4.0/>).

**How to cite this article:** El-Gamel, M., Mohamed, N. & Adel, W. (2023). Genocchi collocation method for accurate solution of nonlinear fractional differential equations with error analysis. *Mathematical Modelling and Numerical Simulation with Applications*, 3(4), 351-375. <https://doi.org/10.53391/mmnsa.1373647>



RESEARCH PAPER

## The role of calcium dynamics with amyloid beta on neuron-astrocyte coupling

Hemlata Jethanandani <sup>1,‡</sup>, Brajesh Kumar Jha <sup>2,\*,‡</sup> and Manisha Ubale <sup>1,‡</sup>

<sup>1</sup>Department of Science & Humanities, Indus Institute of Science Humanities & Liberal Studies (IISHLS), Indus University Rancharda, Ahmedabad-382115 Gujarat, India, <sup>2</sup>Department of Mathematics, School of Technology, Pandit Deendayal Energy University, Gandhinagar 382426, Gujarat, India

\*Corresponding Author

‡ hemlatajethanandani.rs@indusuni.ac.in (Hemlata Jethanandani); brajesh.jha@sot.pdpu.ac.in (Brajesh Kumar Jha); manishadalbhide.gen@indusuni.ac.in (Manisha Ubale)

### Abstract

Amyloid beta ( $A\beta$ ) plaques are associated with neurodegenerative diseases such as Alzheimer's disease. Due to the involvement of  $A\beta$  plaques in the functioning of the brain; cognitive decline disrupts calcium homeostasis in nerve cells and causes abnormal calcium ions ( $Ca^{2+}$ ) signaling patterns. In consequence, there is enhanced neuronal excitability, compromised synaptic transmission, and decreased astrocytic function. Neuron-astrocyte coupling through calcium dynamics with different neuronal functions has been studied. Key signaling molecules in this process include  $Ca^{2+}$ , which control several cellular functions, including neurotransmission and astrocytic regulation. The mathematical model for neuron-astrocyte communication has been developed to study the importance of calcium dynamics in signal transduction between the cells. To understand the wide role of mitochondria, NCX, and amyloid beta with various necessary parameters included in the model,  $Ca^{2+}$  signaling patterns have been analyzed through amplitude modulation and frequency modulation. The results of the current model are simulated and analyzed using XPPAUT. The findings of the current study are contrasted with experimental data from an existing mathematical model that illustrates the impact of calcium oscillation frequency and amplitude modulations in nerve cells.

**Keywords:** Neuron; astrocytes; neurodegenerative diseases; calcium dynamics; amyloid beta

**AMS 2020 Classification:** 37M05; 00A71; 34D20

### 1 Introduction

Amyloid beta ( $A\beta$ ) builds up in the brain and causes progressive cognitive impairment, which are hallmarks of Alzheimer's disease (AD), a debilitating neurodegenerative condition [1]. The

complex interplay between  $A\beta$  and calcium dynamics in neurons and astrocytes has been brought to light by recent studies [2]. Maintaining brain homeostasis depends on the neuron-astrocyte connection, and disruptions in calcium signaling are linked to the etiology of AD. Neuronal dysfunction and cell death in AD are believed to be profoundly influenced by the disruption of  $Ca^{2+}$  homeostasis [3]. Maintaining appropriate  $Ca^{2+}$  levels requires neuron-astrocyte interaction, and recent studies have shown the importance of mitochondria and NCX in this process [4].

In order to control  $Ca^{2+}$  signaling, these two cell types engage in intricate interactions known as neuron-astrocyte coupling [5]. Through specialised transporters, astrocytes absorb excess synaptic  $Ca^{2+}$ , thereby buffering  $Ca^{2+}$  levels in neurons and reducing excitotoxicity [6]. By compromising astrocytic  $Ca^{2+}$  regulation,  $A\beta$  has been demonstrated to interfere with this coupling and increase neuronal susceptibility to  $Ca^{2+}$  overload [5].

An essential function of mitochondria is to preserve the  $Ca^{2+}$  homeostasis of neurons and astrocytic membranes [7]. Research has indicated that an accumulation of  $A\beta$  within mitochondria can impair their functionality and result in a higher generation of reactive oxygen species (ROS). Due to decreased mitochondrial  $Ca^{2+}$  buffering, which lowers the effectiveness of  $Ca^{2+}$  clearance within neurons and astrocytes, this mitochondrial dysfunction can cause problems with  $Ca^{2+}$  handling [8].

Apart from their function of buffering  $Ca^{2+}$ , mitochondria also use processes like  $Ca^{2+}$  absorption and release to modify  $Ca^{2+}$  signalling. These mechanisms can be changed by  $A\beta$ -induced mitochondrial dysfunction, which can impact the  $Ca^{2+}$  dynamics in neurons and astrocytes [9, 10]. Uncontrolled release of  $Ca^{2+}$  by malfunctioning mitochondria can lead to astrocytic dysfunction and neuronal excitotoxicity [11, 12]. In neurons and astrocytes, the sodium-calcium exchanger (NCX) plays a critical role in controlling intracellular  $Ca^{2+}$  levels [13]. It has been demonstrated that  $A\beta$  disrupts NCX function by changing its expression and activity [14]. Further altering neuron-astrocyte connection, dysregulated NCX can worsen  $Ca^{2+}$  dysregulation by increasing  $Ca^{2+}$  inflow and impairing  $Ca^{2+}$  extrusion in both cell types [2]. The two main cell types in the central nervous system are neurons and astrocytes, and the proper functioning of these two populations is essential for brain maintenance [15]. Key signaling molecules, such as calcium ions  $Ca^{2+}$ , are involved in several cellular activities, such as neurotransmitter release, plasticity, and synaptic transmission. Calcium signaling is a mechanism used by both neurons and astrocytes to exchange information and react to modifications in the brain's microenvironment [16]. Action potentials are produced when neurons release neurotransmitters into the synaptic cleft, which causes postsynaptic calcium influx [17]. Changes in synaptic activity and calcium levels are actively sensed by astrocytes, which surround synapses with their tiny processes. Astrocytes can control neuronal excitability and synaptic transmission through a process called gliotransmission [15].

Amyloid beta and calcium de-regulation  $A\beta$ , the pathogenic hallmark protein in AD, has been shown to disrupt calcium homeostasis in neurons and astrocytes, with important effects for neuron-astrocyte connection [18].  $A\beta$  peptides have direct interactions with ion channels, including those that control calcium levels, and cell membranes. Increased intracellular calcium levels in neurons as a result of this interaction ultimately cause neuronal death, and synaptic dysfunction [1, 11]. Astrocytic calcium dynamics are similarly impacted by  $A\beta$  exposure. The removal of extracellular  $A\beta$  is mostly dependent on astrocytes, and an elevated  $A\beta$  load may cause abnormal calcium signaling in astrocytes. Dysfunctional astrocytic calcium signaling undermines their ability to support neurons, compromising synaptic function and neuronal survival [1, 12, 19]. Normally, astrocytes remove excess glutamate from synapses to avoid excitotoxicity. This function is compromised by  $A\beta$ -induced disturbances in astrocytic calcium signaling, which prolong glutamate exposure at synapses [4].

Neurotransmission is impacted by changes in calcium dynamics in both astrocytes and neurons.

Reduced synaptic effectiveness and aberrant synaptic plasticity can be caused by  $A\beta$ -mediated dysregulation [13, 16]. In astrocytes, dysregulation of calcium induced by  $A\beta$  can exacerbate neuroinflammation. The neurodegenerative process is accelerated by reactive astrocytes that emit proinflammatory cytokines. The complex interactions among  $A\beta$ , mitochondria, NCX, and neuron-astrocyte coupling have a major effect on the dynamics of  $Ca^{2+}$  in AD. By upsetting the delicate balance of  $Ca^{2+}$  homeostasis,  $A\beta$  causes malfunction in the mitochondria, interferes with NCX activity, and affects astrocytic  $Ca^{2+}$  regulation. The pathogenesis of AD is aided by these consequences, which increase neuronal susceptibility to  $Ca^{2+}$  excess. In order to determine viable therapeutic strategies targeted at reestablishing appropriate  $Ca^{2+}$  homeostasis in Alzheimer's disease, future research should carry out an exploration of these pathways [20].

We offer a theoretical framework in this work to understand the driving forces behind different  $Ca^{2+}$  oscillation patterns in an AD environment. Examining model solutions additionally provides valuable insights into how  $A\beta$  affects  $Ca^{2+}$  basal levels across a range of timescales. Numerous studies have been conducted on calcium dynamics to illustrate the impacts of different parameters, as evidenced by the literature review. Parkinson's disease starts to progress early when there is a loss or change in this cellular activity [21–23]. To analyze the spatiotemporal fluctuations of intracellular  $Ca^{2+}$  concentration in T lymphocyte cells, a two-dimensional mathematical model has been explored [24]. During oocyte development, eggs develop the capacity to create this specific calcium transient. It has been demonstrated that oocyte cells exhibit cytosolic calcium signaling through the use of parameters including buffers, ryanodine receptor (RyR), and Serca pump [25, 26]. Understanding the cellular mechanism underlying the inclusion and extrusion of free calcium is essential [27]. It has been demonstrated analytically and quantitatively how the glycolytic oscillator chemical model behaves through the flip and generalized flip bifurcations [28].

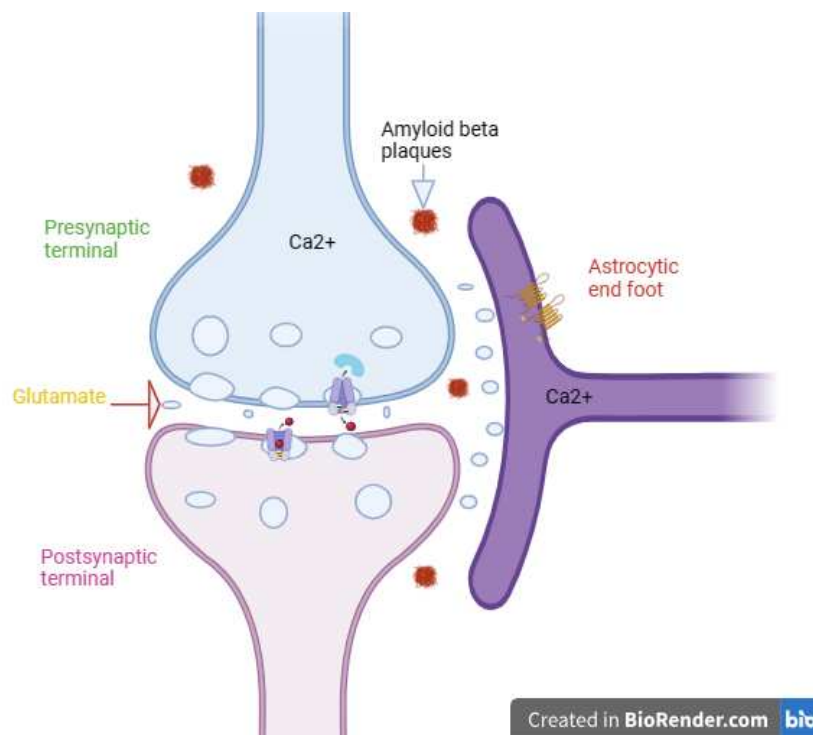


**Figure 1.** Neuron-astrocyte signaling

## 2 Mathematical model of the problem

### Neuron model

The leaky integrate and fire model (LIF) has been used to show the neural communication with required parameters [2]:

$$\tau_m \frac{dV(t)}{dt} = -V(t) + R_m I_{syn}, \quad (1)$$

where  $V$  is the membrane voltage,  $R_m$  is the membrane resistance,  $I_{syn}$  is the input current, and  $\tau_m$  is the membrane time constant.  $V$  is clamped at  $0V(volt)$  when the neuron membrane potential ( $V$ ) approaches a firing threshold value for the neuron, ( $V_{th}$ ).

### Astrocyte-neuron interactions

Gliotransmitters that change neurotransmitter reuptake, boost synaptic strength, or control pruning of synaptic cells may be emitted by astrocytes when exposed to an action potential from a neuron. The neuron-astrocyte coupling process for  $Ca^{2+}$  dynamics is heavily dependent on the inositol trisphosphate ( $IP_3$ ) signaling pathway. Neurotransmitters released by stimulated neurons can activate receptors on astrocytes. The activation of these receptors results in the synthesis of  $IP_3$ , a secondary messenger molecule that causes the astrocyte's internal stores of  $Ca^{2+}$  to be released. Surrounding neurons may be profoundly impacted by this  $Ca^{2+}$  increase in astrocytes, which can alter their activity and synaptic transmission. The model states that the extent of neurotransmitter exposure affects the extension of  $IP_3$ . The neuron-astrocyte coupling describes the two-way exchange of information and interaction that occurs between astrocytes and neurons [29, 30].

$$\frac{dIP_3}{dt} = \frac{IP_3^* - IP_3}{\tau_{ip_3}} + r_{ip_3(AG)}, \quad (2)$$

where  $r_{ip_3}$  is the  $IP_3$  assembly rate,  $IP_3^*$  is the baseline of  $IP_3$  in the steady-state,  $\tau_{ip_3}$  is the  $IP_3$  decay rate.

### Astrocyte dynamics

The  $Ca^{2+}$  flux inside the astrocyte is measured using the Li-Rinzel model. Many computational simulations inside the Li-Rinzel model have demonstrated  $Ca^{2+}$  oscillations for a range of parameter settings [31]. The intracellular expansion triggers reactions in the cytosolic calcium absorption process, including the ER leakage flux, the pump-flux from the cytosol into the ER, and the  $Ca^{2+}$  flux from the ER(Endoplasmic Reticulum) over the  $IP_3$  carriers. By moving  $Ca^{2+}$  across the plasma membrane, the  $Na^+/Ca^{2+}$  exchanger influences the intracellular  $Ca^{2+}$  concentration. The differential equation for the dynamics of  $Ca^{2+}$  in mitochondria is governed by a balance of  $Ca^{2+}$  fluxes [2, 32]:

$$\frac{d[Ca^{2+}]}{dt} = J_{channel} - J_{pump} + J_{leak} + J_{in} - J_{out} - J_{MCU} + J_{mNCX} - J_{NCX}, \quad (3)$$

$$\frac{dh}{dt} = \frac{h_{\infty} - h}{\tau_h}, \quad (4)$$

where

$$h_{\infty} = \frac{Q_2}{Q_2 + Ca^{2+}}, \quad (5)$$

$$\tau_h = \frac{1}{a_2 (Q_2 + Ca^{2+})}, \quad (6)$$

$$Q_2 = d_2 \frac{IP_3 + d_1}{IP_3 + d_3}, \quad (7)$$

where  $h$  is the fraction of activated  $IP_3$ . The following calculates the calcium flux via the channel, pump-flux, and leakage flux from the ER:

$$J_{pump} = v_{ER} \left( \frac{(Ca^{2+})^2}{k_{ER}^2 + (Ca^{2+})^2} \right), \quad (8)$$

$$J_{chan} = r_c m_{\infty}^3 n_{\infty}^3 h^3 (c_0 - (1 + c_1) Ca^{2+}), \quad (9)$$

$$J_{leak} = r_L (c_0 - (1 + c_1) Ca^{2+}), \quad (10)$$

$$J_{out} = k_1 Ca^{2+}, \quad (11)$$

$$J_{NCX} = c_0 \left( \frac{Na_i}{Na_0} \right)^3 \exp \left( \frac{2FV_m}{RT} \right), \quad (12)$$

with

$$m_{\infty} = \frac{IP_3}{IP_3 + d_1}, \quad (13)$$

$$n_{\infty} = \frac{Ca^{2+}}{Ca^{2+} + d_5}, \quad (14)$$

where  $r_c$  represents the maximum CICR (Calcium-induced calcium release) rate,  $c_0$  represents the total of the free  $Ca^{2+}$  cytosolic collection, and  $c_1$  represents the ER/cytoplasm capacity ratio. The  $IP_3$  induced calcium release is shown by  $m_{\infty}$ , the CICR channels are indicated by  $n_{\infty}$ , the maximum absorption amount for the SERCA pump is  $v_{ER}$ , the stimulation constant of the SERCA pump is  $k_{ER}$ , and the calcium leakage amount is  $r_L$ .

### Amyloid beta hypothesis

$IP_3$  concentration is modeled as a linearly increasing function of the membrane leak  $J_{in}$ . To ensure that the steady-state  $Ca^{2+}$  concentration relies on  $p$ , we only include a linearly increasing contribution in this case, even if this rise could be the result of many causes. The effects of  $A\beta$  on the existence of exchangers, channels, and pumps are still largely unknown. Despite this, we have used some of the offered papers to view the  $A\beta$  influence. To add  $k_\beta a^m$  in  $J_{in}$  in order to account for the effect of  $A\beta$  in the model [6, 30]:

$$J_{in} = a_1 + a_2 p + k_\beta a^m, \tag{15}$$

where  $a_1$  and  $a_2$  are parameters and  $m$  denotes a cooperatively coefficients and  $k_\beta$  is a constant of speed.

### Mitochondria model

Studies have demonstrated that the ER and mitochondria cooperate to generate complex functional membranes associated with the ER that is mitochondria-associated membranes (MAMs). The  $Ca^{2+}$  concentration between ER-Mitochondria can reach 10 times higher integrity than in the bulk cytoplasm when cells are activated. When properly activated, the mitochondrial  $Ca^{2+}$  uniporter (MCU) allows for an increase in  $Ca^{2+}$  levels [33]. Owing to their bidirectional nature, the local  $Ca^{2+}$  intake by mitochondria and the inositol triphosphate receptor ( $IP_3R$ ) by  $Ca^{2+}$  can both expand or contract the ER.  $Ca^{2+}$  reveals that by severing the effective feedback from  $Ca^{2+}$  on  $IP_3R$ ,  $Ca^{2+}$  releases, by reducing the ER or the  $Ca^{2+}$ -related  $IP_3R$ s deactivation [7, 8, 34]:

$$\frac{d [Ca^{2+}]_{Mt}}{dt} = J_{MCU} - J_{mNCX}, \tag{16}$$

$$J_{MCU} = v_{mNCX} \left( \frac{Na^3}{k_{Na}^3 + Na^3} \right) \left( \frac{[Ca^{2+}]_{Mt}}{k_{mNCX} + [Ca^{2+}]_{Mt}} \right), \tag{17}$$

$$J_{mNCX} = v_{MCU} \left( \frac{[Ca^{2+}]^2}{k_{MCU}^2 + [Ca^{2+}]^2} \right), \tag{18}$$

where  $[Ca^{2+}]_{Mt}$  mitochondrial calcium concentration and  $J_{MCU}$  and  $J_{mNCX}$  are fluxes of  $Ca^{2+}$  ions through the mitochondrial  $Ca^{2+}$  uniporter and mNCX channels.

### Endocannabinoid dynamics

Several computational models represent the interaction between astrocytes and neurons using tripartite synapse connections. When the signal-receiving neuron is sufficiently depolarized and the synaptic cleft releases a glutamate-like neurotransmitter, 2-AG leaves from the dendrite and attaches itself to CB1Rs on the surface of astrocytes [2]. The model equations are

$$\frac{d (AG)}{dt} = -\frac{AG}{\tau_{AG}} + r_{AG} H(c - c_{th}), \tag{19}$$

$$\frac{d(Glu)}{dt} = -\frac{Glu}{\tau_{Glu}} + r_{Glu}H(c - c_{th}), \quad (20)$$

where  $AG$  denotes the quantity of 2-AG and  $Glu$  denotes the amount of glutamate, and  $\tau_{AG}$  and  $\tau_{glu}$  indicate the relaxation time constants for 2-AG and glutamate, respectively. Glutamate release and 2-AG production are denoted by the variables  $r_{AG}$  and  $r_{Glu}$ , respectively. The release of 2-AG and glutamate is indicated by the Heaviside function  $H(c - c_{threshold})$ , which is accompanied by the  $Ca^{2+}$  threshold and catalyzed by calcium [27].

**Table 1.** Values of biophysical parameters

Astrocyte Constraint	Constraint Description	Value
$\tau_{AG}$	Decay rate of 2-AG	10 s
$\tau_{Glu}$	Decay rate of Glutamate	100 ms
$r_{Glu}$	Maximum rate of Glutamate production	$10 \mu Ms^{-1}$
$r_{AG}$	Maximum rate of AG production	$0.018 \mu Ms^{-1}$
$IP_3^*$	Baseline value of $IP_3$	$0.16 \mu M$
$r_{IP_3}$	Rate of $IP_3$ production	$0.5 \mu Ms^{-1}$
$r_C$	Maximum rate of CICR	$6 s^{-1}$
$r_L$	$Ca^{2+}$ leakage rate from ER	$0.11 s^{-1}$
$v_{ER}$	Maximum rate of SERCA uptake	$0.8 \mu Ms^{-1}$
$k_{ER}$	SERCA pump activation constant	$0.1 \mu M$
$c_1$	Ratio of ER volume to cytosol volume	0.185
$d_1$	$IP_3$ Disconnection constant $Ca^{2+}$	$0.13 \mu M$
$d_2$	$Ca^{2+}$ Dismissal dissociation constant $Ca^{2+}$	$1.049 \mu M$
$d_3$	$IP_3$ Separation constant $Ca^{2+}$	$0.9434 \mu M$
$d_5$	$Ca^{2+}$ Stimulate dissociation constant $Ca^{2+}$	$0.08234 \mu M$
$a_2$	$IP_3R$ $Ca^{2+}$ Dismissal binding rate	$0.2 \mu Ms^{-1}$
$Ca^{2+} threshold$	Astrocyte Glutamate release threshold	$0.3 \mu M$
$c_0$	Total free $Ca^{2+}$ cytosol concentration	$2 \mu M$
$\tau_m$	Membrane time constant	0.1
$I_{sym}$	Injected current	2
$V$	Firing threshold voltage	$9 mv$
$R_m$	Membrane resistance	$1.2 G\Omega$
$k_{Na}$	$Na^+$ activation constants for the mNCX	$7.4 mM$
$k_{mNCX}$	$Ca^{2+}$ activation constants for mNCX	$45 \mu M$
$k_{MCU}$	$Ca^{2+}$ activation constants for MCU	$0.84 \mu M$
$Na^+$	$Na^+$ Concentrations in the Cytosol	$12 mM$
$V_{mNCX}$	Maximal flux through the mNCX	$100 \mu Ms^{-1}$
$V_{MCU}$	Maximal flux through the MCU	$0.07 \mu Ms^{-1}$
$Na_i$	Intracellular $Na^+$ concentration	$12 \mu M$
$Na_o$	Extracellular $Na^+$ concentration	$145 \mu M$
$F$	Faraday's constant	$96485 Cmol^{-1}$
$R$	Gas constant	$8.314 JK^{-1}mol^{-1}$
$T$	Absolute temperature	$310 (^{\circ}C)$
$V_m$	Membrane potential	$-70000 V$
$k_1$	Rate constant of $Ca^{2+}$ extrusion	$0.5 s^{-1}$
$a_1$	Parameter for membrane leak	$0.1 \mu Ms^{-1}$
$a_2$	Parameter for membrane leak	$0.02 s^{-1}$
$k_{\beta}$	Constant of speed	$0.18 s^{-1}$
$m$	Cooperatively coefficients	4
$p$	Linear increase of $IP_3$	0.13
$a$	Measurement of $A\beta$ presence	1.15

**Table 1** provides the starting values for the variables and parameters used in this work [2, 33–35]. The system appears to be inactive based on the principal variable rates. By initializing both variables to zero, experimental measurements have been made for  $Ca^{2+}$  and  $h$ . To duplicate the model,  $IP_3$  levels have been limited at  $0.16\mu M$  (that is equal to  $IP_3^*$ ) until  $Ca^{2+}$  and  $h$  have been balanced [36–38].

### 3 Results

The mechanism of  $Ca^{2+}$ -dependent exosome release is examined, along with the coupling of neuron and astrocytes on the  $Ca^{2+}$ -driven exosomal dynamics, in response to different values of factors linked to mitochondria, NCX, and amyloid beta. The parameter values listed in **Table 1** are used to generate the numerical results provided in this section [2, 33–35]. We aim to demonstrate the influence of  $A\beta$  on the promotion of a chemical involved in several cellular processes. As of right now,  $IP_3$  serves as the main agonist, which can subsequently cause the release of  $Ca^{2+}$  from different fluxes. In all figures,  $c$  represents  $Ca^{2+}$  concentrations.

- i. First, we have used the neglected NCX (Sodium-Calcium exchanger) and Amyloid beta effects on  $Ca^{2+}$  dynamics to characterize the model's solutions with mitochondria.
- ii. Secondly, we have extended to incorporate the impact of NCX (sodium-calcium exchanger) on neuron-astrocyte coupling calcium dynamics, likewise in the absence of amyloid beta.
- iii. Finally, we have incorporated flux  $J_{in}$  to account for the  $A\beta$  impacts of membrane potential on  $Ca^{2+}$  dynamics.

The neuron-astrocyte model has been analyzed using the XPPAUT software, and the Euler integration approach was employed in all of the results shown here. The model dynamics in the following three sections demonstrate that aberrant  $Ca^{2+}$  can arise when  $A\beta$  is present. These aberrant signals can arise in a variety of scenarios, pointing to a complex relationship between  $A\beta$ 's effect and the model's constituent parts. As a result, we deconstruct the model's dynamics by monitoring the outcomes of changing one or two parameters inside a particular signaling component. Finally, we take membrane potential into account and explore model solutions at different  $A\beta$  levels while  $IP_3$  concentration is fixed [39].

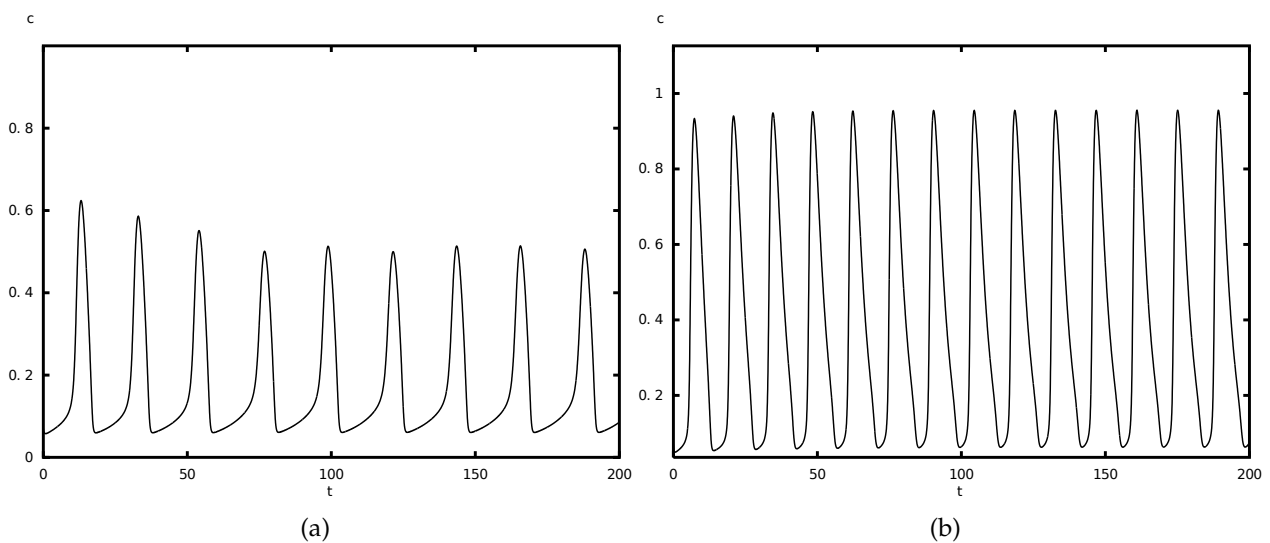


**Figure 2.** The  $Ca^{2+}$  frequency modulation is displayed in **Figure 2(a)**–**Figure 2(b)**. **Figure 2(a)** displays the FM mode results of  $Ca^{2+}$  oscillations for  $r_L = 0.11$ ,  $IP_3 = 0.29$ , and  $k_{ER} = 0.09$  in the proposed model while **Figure 2(b)** displays the FM mode results of  $Ca^{2+}$  oscillations for  $r_L = 0.8$ , with fixed values of  $IP_3 = 0.78$  and  $k_{ER} = 0.07$  in the original model

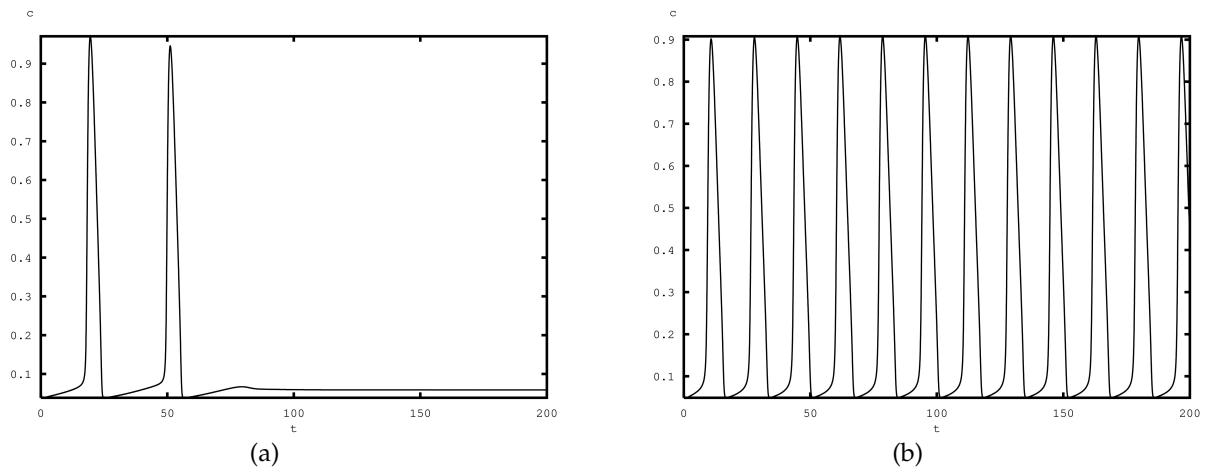


**Figure 3.** These graphs **Figure 3(a)-Figure 3(a)** show the results of frequency modulation  $Ca^{2+}$  oscillations for  $IP_3=0.5$ ,  $r_L$  range 0.08 to 0.15 and  $k_{ER}=0.07$

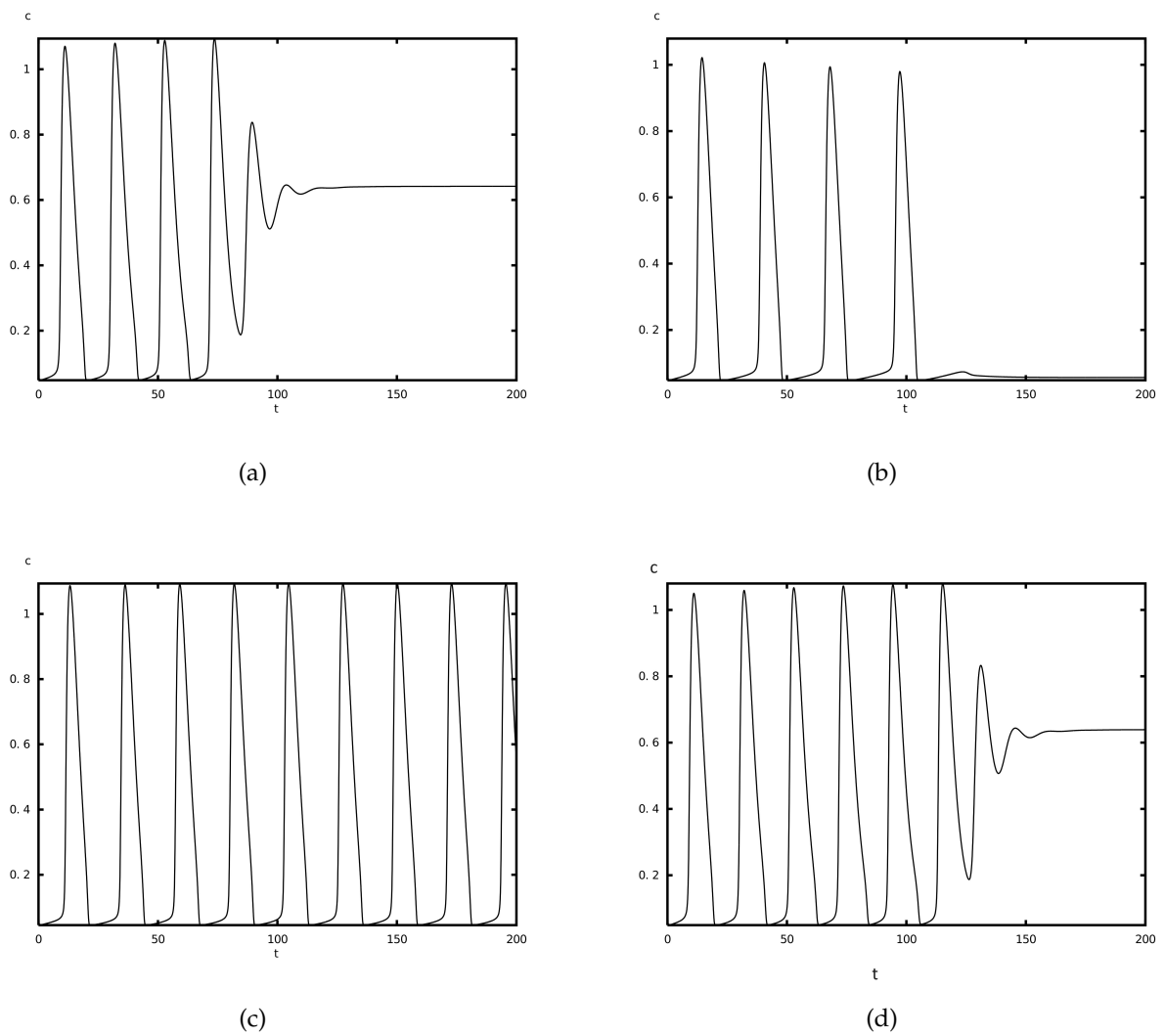


**Figure 4.** These graphs **Figure 4(a)-Figure 4(d)** show the results of frequency modulation  $Ca^{2+}$  oscillations  $IP_3=0.35$ ,  $IP_3=0.32$ ,  $IP_3=0.28$ , and  $IP_3=0.27$ , respectively, for  $p=0.13$  and  $a=1.15$

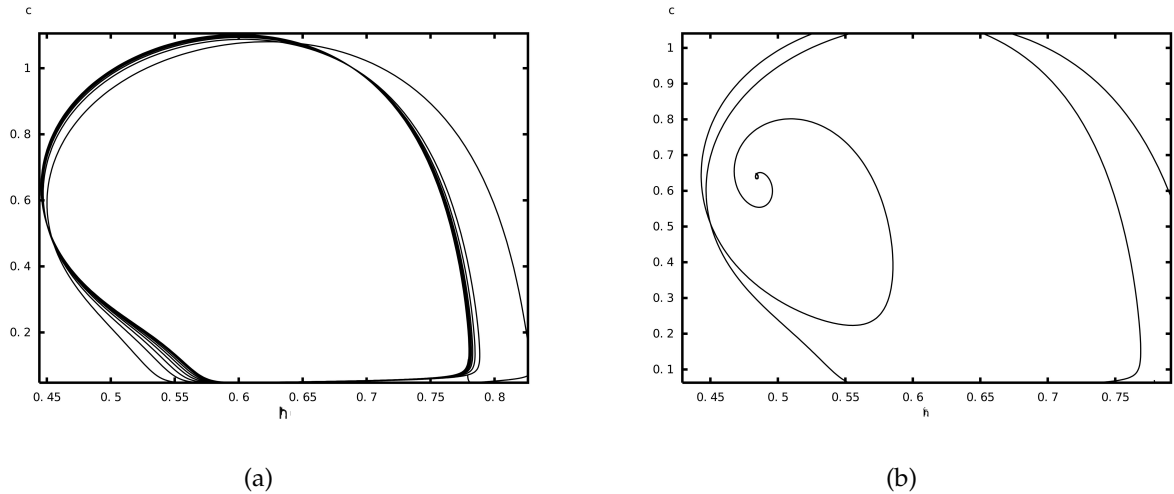


**Figure 5.** The phase plane analysis diagram between  $Ca^{2+}$  and  $IP_3$  fraction with distinct values of the parameters

## 4 Discussion

The cytoplasmic calcium level remains constant while the calcium dynamic is in equilibrium. The  $IP_3$  readings are related to the stability of the calcium level. At low  $IP_3$  values,  $Ca^{2+}$  oscillations are weakly stimulated; at higher  $IP_3$  values, the modulation is altered by  $Ca^{2+}$  oscillations. As  $IP_3$  increases in **Figure 4**,  $Ca^{2+}$  oscillations alter as  $Ca^{2+}$  concentration rises. The system eventually finds a stable state and loses its oscillation behavior at a certain value of  $IP_3$ . The experiment demonstrated that adding  $A\beta$  directly increases  $Ca^{2+}$  dependent fluorescence, which is an indication of intracellular  $Ca^{2+}$  levels [30]. According to the findings,  $A\beta$  does not directly bind with the  $IP_3$  receptor; rather, it stimulates the synthesis of  $IP_3$  through G-protein-mediated activation of PLC, which opens  $IP_3$  receptors and causes intracellular  $Ca^{2+}$  liberation. As a result, even though  $IP_3$  is digested in tens of seconds,  $IP_3$  are actively activated in the presence of  $A\beta$  and last for several minutes or hours. The  $Ca^{2+}$  oscillations appear and attain an equilibrium state for a specific range of  $IP_3$ . **Figure 3** shows how  $Ca^{2+}$  oscillations alter modulation as  $r_L$  ( $Ca^{2+}$  leakage rate from ER) increases and reaches the steady-state at a greater level of  $Ca^{2+}$  concentration. At a specific value of  $r_L$ , the oscillation vanishes, and the concentration of  $Ca^{2+}$  achieves the steady-state. The  $Ca^{2+}$  oscillations appear and achieve an equilibrium state for a specific range 0.08 to 0.15 of  $r_L$ . Calcium dynamics is in equilibrium when the cytoplasmic calcium level is constant ( $dc/dt = 0$ ) and the percentage of inactive  $IP_3R$  remains constant ( $dh/dt = 0$ ). The calcium oscillations in **Figure 4(a)**-**Figure 4(d)** vary differently as  $IP_3^*$  (Baseline value of  $IP_3$ ) decreases and eventually disappear when  $IP_3^*$  gets closer to a stable state. The calcium leakage rate from the ER causes the calcium concentration to stabilize. The calcium oscillation appears and reaches an equilibrium state for the  $0.27 < IP_3^* < 0.36$ . For a specific stimulation intensity, both the range and amplitude of calcium oscillations increase within the specified range. The highest value of the calcium responses in the amplitude modulation encodes the  $IP_3$  level. It is closely related to how strongly the stimulus acts on the cell. Changes in  $IP_3$  cause calcium responses in the frequency modulation and the information contained in those interspike intervals is encoded.  $IP_3^*$  must fluctuate dynamically under the influence of  $A\beta$  in order to duplicate the reaction in  $Ca^{2+}$ . Examine the effect of membrane potential and consider model solutions for various  $IP_3^*$  concentration levels once  $A\beta$  is fixed. In an experimental situation,  $IP_3^*$  can be photoreleased simultaneously throughout a cell.  $IP_3^*$  diffusion is constant and minimized under these conditions. The model can demonstrate

$Ca^{2+}$  oscillations, indicative of various cell types, by varying the amount of  $IP_3^*$  accessible in the cytoplasm. These oscillation patterns are necessary for cells to maintain appropriate concentration gradients and recover homeostasis after a triggering event. In the presence of  $A\beta$ , model  $Ca^{2+}$  oscillations emerge and disappear due to transitions through amplitude modulations as  $IP_3^*$  grows. Dynamic transitions across (Figure 5) can account for both the increases in  $Ca^{2+}$  oscillations and the observed aberrant  $Ca^{2+}$  signals through phase-plane analysis. While there has been some accumulation of  $A\beta$  in an AD environment, it is assumed that this quantity stays constant over the course of our simulation.  $A\beta$  can accumulate to produce large amplitude oscillations and elevated steady-state values. A range of behaviors are displayed by the corresponding model solutions: aberrant  $Ca^{2+}$  signals, steady-state  $Ca^{2+}$  signals, and stable periodic solutions. An essential second messenger in the neurological system is intracellular  $Ca^{2+}$  regulation. The signaling pathways in neurons that govern neurotransmitter release, metabolism, gene expression, plasticity, development, proliferation, and cell death are known to be mediated by  $Ca^{2+}$ . Because of this,  $Ca^{2+}$  might be very important in the pathophysiology of AD. Unfortunately, understanding exactly how  $A\beta$  affects various intracellular regulating mechanisms and components is challenging due to the complexity of  $Ca^{2+}$  signaling. Through the decoupling of specific components by various investigations, we can better comprehend intracellular  $Ca^{2+}$  signaling by combining these theories into a whole-cell computational model.

## 5 Conclusion

In the current study using the neuron-astrocyte model, the synaptic connection initiates diffusions of the gliotransmitters 2-AG and glutamates. The solution graphic shows how variable-parameter  $Ca^{2+}$  frequency and amplitude modulation of leak flow is impacted by mitochondria, NCX, and  $A\beta$ . The proposed model combines cell activation and intracellular signaling. A mathematical model is developed to accurately quantify the  $Ca^{2+}$ -mediated astrocytic exosome exocytosis in AD that is driven by Amyloid-beta. Our model indicates that increasing the amount of  $A\beta$  can lead to aberrant signals and changes in homeostasis levels. A change in intracellular  $Ca^{2+}$  homeostasis can have an impact on the cascade of apoptotic signals. A comparison analysis was performed to quantify the effects of different components related to mitochondria, NCX, and  $A\beta$  the leak fluxes on the calcium signaling process through the amplitude and frequency modulation. They do, however, transform into exosomes produced by astrocytes in AD, which have the potential to harm neurons. This computational model tracks the influence of numerous interrelated biological pathways, which can aid in our understanding of complicated cellular activity in an AD context.

## Declarations

### Ethical approval

The authors state that this research complies with ethical standards. This research does not involve either human participants or animals.

### Consent for publication

Not applicable.

### Conflicts of interest

The authors confirm that there is no competing interest in this study.

## Data availability statement

Data availability is not applicable to this article as no new data were created or analyzed in this study.

## List of abbreviations

**Table 2.** Abbreviations and their explanations

Abbreviations	Explanation
AD	Alzheimer's disease
CICR	Calcium-induced calcium release
ER	Endoplasmic reticulum
$IP_3$	Inositol triphosphate
$IP_3R$	Inositol triphosphate receptor
MAMs	Mitochondria associated membrane
MCU	Mitochondrial $Ca^{2+}$ uniporter
mNCX	Mitochondrial $Na^+ / Ca^{2+}$ exchangers
PLC	Phospholipase C
ROS	Reactive oxygen species
RYR	Ryanodine receptor
NCX	$Na^+ / Ca^{2+}$ exchangers

## Funding

The authors declare that they have never had any known competing financial interests or personal ties that may seem to have influenced the work revealed in this study.

## Author's contributions

H.J.: Investigation, Data Curation, Conceptualization, Methodology, Software, Writing-Original draft preparation. B.K.J.: Supervision, Conceptualization, Methodology, Visualization, Validation, Writing-Reviewing and Editing. M.U.: Supervision, Writing-Reviewing and Editing. All authors have read and agreed to the published version of the manuscript.

## Acknowledgements

The authors are highly thankful to all reviewers and editors for reviewing this article and giving valuable suggestions to improve the article.

## References

- [1] Ye, M. and Zuo, H. Stability analysis of regular and chaotic  $Ca^{2+}$  oscillations in astrocytes. *Discrete Dynamics in Nature and Society*, 2020, 1-9, (2020). [[CrossRef](#)]
- [2] Wade, J.J., McDaid, L.J., Harkin, J., Crunelli, V. and Kelso, J.S. Bidirectional coupling between astrocytes and neurons mediates learning and dynamic coordination in the brain: a multiple modeling approach. *PloS One*, 6(12), e29445, (2011). [[CrossRef](#)]
- [3] Dave, D.D. and Jha, B.K. Mathematical modeling of calcium oscillatory patterns in a neuron. *Interdisciplinary Sciences: Computational Life Sciences*, 13, 12-24, (2021). [[CrossRef](#)]
- [4] Falcke, M., Or-Guil, M. and Bär, M. Dispersion gap and localized spiral waves in a model for intracellular  $Ca^{2+}$  dynamics. *Physical Review Letters*, 84(20), 4753, (2000). [[CrossRef](#)]

- [5] Kalia, M., Meijer, H.G., van Gils, S.A., van Putten, M.J. and Rose, C.R. Ion dynamics at the energy-deprived tripartite synapse. *PLoS Computational Biology*, 17(6), e1009019, (2021). [[CrossRef](#)]
- [6] Keener, J. and Sneyd, J. The Heart. In *Mathematical Physiology* (pp. 523-626). New York, NY: Springer, (2009). [[CrossRef](#)]
- [7] Jha, B.K., Joshi, H. and Dave, D.D. Portraying the effect of calcium-binding proteins on cytosolic calcium concentration distribution fractionally in nerve cells. *Interdisciplinary Sciences: Computational Life Sciences*, 10, 674-685, (2018). [[CrossRef](#)]
- [8] Jha, A. and Jha, B.K. Computational modelling of calcium buffering in a star shaped astrocyte. In *Proceedings of the 2019 9th International Conference on Bioscience, Biochemistry and Bioinformatics (ICBBB)*, pp. 63-66, Singapore, (2019, January). [[CrossRef](#)]
- [9] Dave, D.D. and Jha, B.K. 2D finite element estimation of calcium diffusion in Alzheimer's affected neuron. *Network Modeling Analysis in Health Informatics and Bioinformatics*, 10, 43, (2021). [[CrossRef](#)]
- [10] Vatsal, V.H., Jha, B.K. and Singh, T.P. To study the effect of ER flux with buffer on the neuronal calcium. *The European Physical Journal Plus*, 138, 494, (2023). [[CrossRef](#)]
- [11] Nadkarni, S. and Jung, P. Spontaneous oscillations of dressed neurons: a new mechanism for epilepsy?. *Physical Review Letters*, 91(26), 268101, (2003). [[CrossRef](#)]
- [12] Lenk, K., Satuvuori, E., Lallouette, J., Ladrón-de-Guevara, A., Berry, H. and Hyttinen, J.A. A computational model of interactions between neuronal and astrocytic networks: the role of astrocytes in the stability of the neuronal firing rate. *Frontiers in Computational Neuroscience*, 13, 92, (2020). [[CrossRef](#)]
- [13] Zuo, H. and Ye, M. Bifurcation and numerical simulations of  $Ca^{2+}$  oscillatory behavior in astrocytes. *Frontiers in Physics*, 8, 258, (2020). [[CrossRef](#)]
- [14] Zhou, A., Liu, X. and Yu, P. Bifurcation analysis on the effect of store-operated and receptor-operated calcium channels for calcium oscillations in astrocytes. *Nonlinear Dynamics*, 97, 733-748, (2019). [[CrossRef](#)]
- [15] Pankratova, E.V., Kalyakulina, A.I., Stasenko, S.V., Gordleeva, S.Y., Lazarevich, I.A. and Kazantsev, V.B. Neuronal synchronization enhanced by neuron-astrocyte interaction. *Nonlinear Dynamics*, 97, 647-662, (2019). [[CrossRef](#)]
- [16] Oku, Y., Freseman, J., Miwakeichi, F. and Hülsmann, S. Respiratory calcium fluctuations in low-frequency oscillating astrocytes in the pre-Bötzinger complex. *Respiratory Physiology & Neurobiology*, 226, 11-17, (2016). [[CrossRef](#)]
- [17] Naji, R. and Abdulateef, B. The dynamics of model with nonlinear incidence rate and saturated treatment function. *Science International*, 29(6), 1223-1236, (2017).
- [18] Li, J.J., Du, M.M., Wang, R., Lei, J.Z. and Wu, Y. Astrocytic gliotransmitter: diffusion dynamics and induction of information processing on tripartite synapses. *International Journal of Bifurcation and Chaos*, 26(08), 1650138, (2016). [[CrossRef](#)]
- [19] Matrosov, V.V. and Kazantsev, V.B. Bifurcation mechanisms of regular and chaotic network signaling in brain astrocytes. *Chaos: An Interdisciplinary Journal of Nonlinear Science*, 21(2), 023103, (2011). [[CrossRef](#)]
- [20] Faramarzi, F., Azad, F., Amiri, M. and Linares-Barranco, B. A neuromorphic digital circuit for neuronal information encoding using astrocytic calcium oscillations. *Frontiers in Neuroscience*, 13, 998, (2019). [[CrossRef](#)]

- [21] Singh, T. and Adlakha, N. Numerical investigations and simulation of calcium distribution in the alpha-cell. *Bulletin of Biomathematics*, 1(1), 40-57, (2023). [[CrossRef](#)]
- [22] Joshi, H. and Jha, B.K. Chaos of calcium diffusion in Parkinson's infectious disease model and treatment mechanism via Hilfer fractional derivative. *Mathematical Modelling and Numerical Simulation with Applications*, 1(2), 84-94, (2021). [[CrossRef](#)]
- [23] Nakul, N., Mishra, V. and Adlakha, N. Finite volume simulation of calcium distribution in a cholangiocyte cell. *Mathematical Modelling and Numerical Simulation with Applications*, 3(1), 17-32, (2023). [[CrossRef](#)]
- [24] Naik, P.A. Modeling the mechanics of calcium regulation in T lymphocyte: a finite element method approach. *International Journal of Biomathematics*, 13(05), 2050038, (2020). [[CrossRef](#)]
- [25] Naik, P.A. and Pardasani, K.R. Finite element model to study calcium signalling in oocyte cell. *International Journal of Modern Mathematical Sciences*, 15(01), 58-71, (2017).
- [26] Naik, P.A. and Pardasani, K.R. Three-dimensional finite element model to study calcium distribution in oocytes. *Network Modeling Analysis in Health Informatics and Bioinformatics*, 6, 16, (2017). [[CrossRef](#)]
- [27] Joshi, H., Yavuz, M. and Stamova, I. Analysis of the disturbance effect in intracellular calcium dynamic on fibroblast cells with an exponential kernel law. *Bulletin of Biomathematics*, 1(1), 24-39, (2023). [[CrossRef](#)]
- [28] Naik, P.A., Eskandari, Z. and Shahraki, H.E. Flip and generalized flip bifurcations of a two-dimensional discrete-time chemical model. *Mathematical Modelling and Numerical Simulation with Applications*, 1(2), 95-101, (2021). [[CrossRef](#)]
- [29] Marambaud, P., Dreses-Werringloer, U. and Vingtdoux, V. Calcium signaling in neurodegeneration. *Molecular Neurodegeneration*, 4, 20, (2009). [[CrossRef](#)]
- [30] Latulippe, J., Lotito, D. and Murby, D. A mathematical model for the effects of amyloid beta on intracellular calcium. *PLoS One*, 13(8), e0202503, (2018). [[CrossRef](#)]
- [31] Manninen, T., Havela, R. and Linne, M.L. Reproducibility and comparability of computational models for astrocyte calcium excitability. *Frontiers in Neuroinformatics*, 11, 11, (2017). [[CrossRef](#)]
- [32] Schampel, A. and Kuerten, S. Danger: high voltage-the role of voltage-gated calcium channels in central nervous system pathology. *Cells*, 6(4), 43, (2017). [[CrossRef](#)]
- [33] Grubelnik, V., Larsen, A.Z., Kummer, U., Olsen, L.F. and Marhl, M. Mitochondria regulate the amplitude of simple and complex calcium oscillations. *Biophysical Chemistry*, 94(1-2), 59-74, (2001). [[CrossRef](#)]
- [34] Jha, B.K., Jha, A. and Adlakha, N. Three-dimensional finite element model to study calcium distribution in astrocytes in presence of VGCC and excess buffer. *Differential Equations and Dynamical Systems*, 28, 603-616, (2020). [[CrossRef](#)]
- [35] Cataldi, M. The changing landscape of voltage-gated calcium channels in neurovascular disorders and in neurodegenerative diseases. *Current Neuropharmacology*, 11(3), 276-297, (2013). [[CrossRef](#)]
- [36] Gao, H., Liu, L. and Chen, S. Simulation of  $Ca^{2+}$  oscillations in astrocytes mediated by amyloid beta in Alzheimer's disease. *BioRxiv*, 2020-03, (2020). [[CrossRef](#)]
- [37] Liu, L., Gao, H., Li, J. and Chen, S. Probing microdomain  $Ca^{2+}$  activity and synaptic transmission with a node-based tripartite synapse model. *Frontiers in Network Physiology*, 3, 1111306, (2023). [[CrossRef](#)]

- [38] Zeng, S., Li, B., Zeng, S. and Chen, S. Simulation of spontaneous  $Ca^{2+}$  oscillations in astrocytes mediated by voltage-gated calcium channels. *Biophysical Journal*, 97(9), 2429-2437, (2009).
- [39] Ermentrout, B. and Mahajan, A. Simulating, analyzing, and animating dynamical systems: a guide to XPPAUT for researchers and students. *Applied Mechanics Reviews*, 56(4), B53, (2003). [[CrossRef](#)]

Mathematical Modelling and Numerical Simulation with Applications (MMNSA)  
(<https://dergipark.org.tr/en/pub/mmnsa>)



**Copyright:** © 2023 by the authors. This work is licensed under a Creative Commons Attribution 4.0 (CC BY) International License. The authors retain ownership of the copyright for their article, but they allow anyone to download, reuse, reprint, modify, distribute, and/or copy articles in MMNSA, so long as the original authors and source are credited. To see the complete license contents, please visit (<http://creativecommons.org/licenses/by/4.0/>).

**How to cite this article:** Hemlata Jethanandan, H., Jha, B.K. & Ubale, M. (2023). The role of calcium dynamics with amyloid beta on neuron-astrocyte coupling. *Mathematical Modelling and Numerical Simulation with Applications*, 3(4), 376-390. <https://doi.org/10.53391/mmnsa.1398320>